Nuclear Structure of Light Ca and Heavy Cr Isotopes

Dissertation
zur
Erlangung des Doktorgrades (Dr. rer. nat.)
der
Mathematisch-Naturwissenschaftlichen Fakultät
der
Rheinischen Friedrich-Wilhelms-Universität Bonn

vorgelegt von
Alexander Bürger
aus
Saarbrücken

Bonn 2007

Angefertigt mit Genehmigung der Mathematisch-Naturwissenschaftlichen Fakultät der
Rheinischen Friedrich-Wilhelms-Universität Bonn

1. Referent: Prof. Dr. H. Hübel
2. Referent: Prof. Dr. U. Thoma

Tag der Promotion:

Contents

1. Introduction **1**

2. Concepts and Tools **3**
2.1. The Independent Particle Shell Model 3
2.2. Residual Interactions 6
2.2.1. Interactions for the fp Shell 7
2.2.2. Interactions for the sd Shell 7
2.2.3. Effects in Exotic Nuclei 8
2.3. Reduced Transition Probabilities and Coulomb Excitation 8
2.3.1. Reduced Transition Probabilities 8
2.3.2. Coulomb Excitation 10
2.4. Knockout Reactions 11
2.4.1. Simple Picture of the Knockout Process 11
2.4.2. Outline of the Knockout Process Calculation 12
2.4.3. Spectroscopic Factors 14
2.5. Isospin 15

3. Structure Investigations of ^{36}Ca **17**
3.1. Experimental Considerations 18
3.2. Experimental Setup 19
3.2.1. Primary Target SISSI 19
3.2.2. Alpha Spectrometer 20
3.2.3. Time-of-Flight Before the Secondary Target 21
3.2.4. Secondary Target 23
3.2.5. Gamma-Ray Detectors – "Château de Cristal" 23
3.2.6. Spectrometer SPEG 24
3.3. Experiment and Data Analysis 26
3.3.1. $B\rho$ Calibration of SPEG 27
3.3.2. Energy Calibration of the BaF_2-Detectors 28
3.3.3. Particle Identification After the Target 28
3.3.4. Efficiency of SPEG 30
3.3.5. Particle Identification Before the Target 32
3.3.6. Double-Counting in CATS 32
3.3.7. Time Gate on the BaF_2 Detectors 32
3.3.8. Correction for the Relativistic Doppler Shift 33
3.3.9. Reconstruction of γ-Ray Energies with Add-Back 34

3.4. Geant4-Simulation of the Experiment . . . 34
3.4.1. Detector and Material Geometries . . . 35
3.4.2. Physical Processes in the Simulation . . . 36
3.4.3. Simulation results . . . 38
3.5. Results . . . 40
3.5.1. The Energy of the First 2^+ State . . . 41
3.5.2. Momentum distributions . . . 42
3.5.3. Total Cross Section for the One-Neutron Knockout from ^{37}Ca . . . 45
3.6. Discussion . . . 48
3.6.1. Excitation Energy of the 2^+ State . . . 48
3.6.2. Shell Occupancies . . . 49
3.7. Conclusions . . . 54

4. Confirmation of the $N = 32$ Shell Closure in Cr Isotopes **55**
4.1. Previous Information . . . 55
4.2. Experimental Considerations . . . 56
4.3. Experimental Setup . . . 56
4.3.1. Particle Beam . . . 57
4.3.2. The Fragment Separator FRS . . . 58
4.3.3. Secondary Beam Detectors . . . 58
4.3.4. Target and γ-Ray Detectors . . . 58
4.3.5. The Detector CATE . . . 60
4.4. Experiment and Data Analysis . . . 60
4.4.1. Sub-Event Matching . . . 61
4.4.2. Detectors for γ Radiation . . . 62
4.4.3. Particle Identification and Tracking . . . 63
4.4.4. Gamma-Ray Energy Spectra . . . 66
4.5. Results . . . 66
4.6. Discussion . . . 69

5. Summary **71**

A. Other Results from the GANIL Experiment **73**
A.1. Spectroscopy of ^{37}Ca . . . 73
A.2. Spectroscopy of ^{32}Ar and ^{28}S . . . 76
A.3. Spectroscopy of ^{31}Ar . . . 76
A.4. Spectroscopy of ^{29}S . . . 77

B. Software for the Analysis of Knockout Experiments **79**

C. Scattering Angle Calculation **85**

D. Efficiency Measurement with ^{60}Co **87**

List of Tables

3.1. Deduced target thicknesses in the GANIL experiment 23
3.2. Runs of the GANIL experiment 27
3.3. Calibration of the BaF_2-detectors at GANIL 29
3.4. Experimental and simulated efficiencies of the "Château de Cristal" . . . 39
3.5. Cross sections for the one-neutron knockout from ^{37}Ca. 47
3.6. Parameters for the calculation of momentum distributions 50
3.7. Shell occupancies of ^{36,37}Ca calculated with `antoine` 51
3.8. Cross sections and spectroscopic factors from the GANIL experiment . . . 52

4.1. Excitation energies in Cr isotopes 55
4.2. Runs of the GSI experiment 61
4.3. Cr transition intensities and $B(E2)$ values 67

A.1. Experimental and calculated excitation energies for ^{37}Ca and ^{37}Cl 75

List of Figures

2.1. Radial dependence of mean potentials 4
2.2. Single-particle energies from the shell model 4
2.3. Single-particle energies as function of the nuclear mass 5
2.4. Shell structure signatures in Ca isotopes 6
2.5. Coulomb excitation 10
2.6. Coulomb excitation, GDR, and GQR cross sections 11
2.7. Coulomb excitation cross sections for E2, E1, and M1 transitions 11
2.8. Geometry of the scattering nuclei for knockout 13

3.1. Accelerators and experimental halls at GANIL 20
3.2. Schematic view of a Galotte MCP detector 21
3.3. View of the CATS MWPC detector 22
3.4. Photo of the Château de Cristalin the experimental setup 23
3.5. View on SPEG 25
3.6. Schematic illustration of a drift chamber in SPEG. 25
3.7. $B\rho$ calibration of SPEG 27
3.8. Particle identification with SPEG 31
3.9. Width of CATS charge distributions 33
3.10. Experimental and simulated scattering off the CATS wires 38
3.11. Partial decay scheme for ^{152}Eu 39
3.12. Gamma-ray spectra for ^{36}Ca. 41
3.13. Time-energy matrix measured in coincidence with ^{36}Ca 41
3.14. Inclusive and individual momentum distributions for ^{36}Ca. 42
3.15. Experimental and simulated momentum distributions of ^{36}Ca. 43
3.16. χ^2 values for momentum distributions in ^{36}Ca 44
3.17. Energy-dependence of the knockout cross section 46
3.18. Mirror energy differences for $|T_z| = 1$ and 2. 49
3.19. Empirical quenching factors R_s 53
3.20. Reduction factors R'_s as for individual excited states 53

4.1. Overview of the RISING Setup 57
4.2. Cluster Detectors of the RISING setup 59
4.3. Schematic view of the CATE detector 60
4.4. Tracking of the Beam Particles 63
4.5. RISING γ-ray time-energy matrix 64
4.6. RISING particle identification 65

4.7. Scattering angles for ^{54}Cr 66
4.8. RISING γ-ray spectra of Cr isotopes 67
4.9. B(E2) values of Cr isotopes 68
4.10. B(E2) values of Cr and Ti isotopes 69
4.11. E4/E2 ratios for Cr and Ti isotopes 70

A.1. Gamma-ray spectra for ^{37}Ca 74
A.2. Partial level schemes for ^{37}Ca and ^{37}Cl. 75
A.3. Gamma-ray spectra for the nuclei ^{32}Ar and ^{28}S. 76
A.4. Gamma-ray spectrum for ^{31}Ar. 76
A.5. Gamma-ray spectrum for ^{29}S. 77

B.1. Illustration of the splitting into cubes 81
B.2. Database query times as function of event and cube count 83

D.1. Decay scheme for ^{60}Co 88

1. Introduction

> The other approach is that of the experimentalist and consists in obtaining by direct experimentation as many data as possible for individual nuclei.
> ...
> The shell model, although proposed by theoreticians, really corresponds to the experimentalist's approach.
>
> *(M. Goeppert-Mayer, Nobel Lecture, 12. December 1963)*

Although the nuclear shell model was conceived almost 60 years ago, and despite the continuous efforts in experimental and theoretical nuclear physics research, the prediction of nuclear properties is still a challenging task. While global structures, e.g. *magic numbers* apparent in the nucleon separation energies, and basic properties of some stable nuclei can be explained in terms of the shell model since the 1950's, the precise description of nuclei still is difficult for nuclei away from closed shells, far off stability, or for higher excited states. Progress is made in small steps, by collecting new experimental data and comparing them to theoretical expectations, or by tests on nuclei predicted to exhibit special properties. These advances are based on technical progress, e.g. in accelerator technique, spectrometers and computer power, and on many years of reflection, trial and error.

The study of *exotic nuclei*, i.e. nuclei far away from the beta stability line, is one of the major current research areas in nuclear physics. The investigation of such nuclei becomes possible only gradually with the increasing intensity of the radioactive beams that can be delivered by accelerators. It has become evident that the shell structure of exotic nuclei may be different from that of stable nuclei. For example, new shell closures may appear, or nuclei with magic nucleon numbers may no longer exhibit signs of magicity.

In this thesis, experimental data have been collected for exotic nuclei in the mass regions around $A \approx 40$ and $A \approx 60$ to contribute to the investigation of shell structure at $N = 16$ in Calcium and $N = 32$ in Chromium isotopes, respectively.

The first chapter of this text consists of a very brief introduction into the shell model and residual interactions. It also includes a description of the processes used in the experiments described in the second and third chapter.

Chapter two reports on the (chronologically) second experiment performed for this thesis. The experiment was devoted to the study of the proton-rich nucleus Calcium-36. It was possible to obtain data on the ground state and the first excited state of the lightest known even Ca isotope, none of which were known at the beginning of the thesis. These data are compared to shell model predictions and found to be largely compatible,

although deviations in details become visible.

The third chapter contains a report on an experiment performed to test a shell model prediction. The heavy Chromium isotopes with mass $A = 56$ and $A = 58$ were investigated to learn more about a presumed shell closure at $N = 32$ or 34 for exotic nuclei in this region. This is an example of new shell structure for exotic nuclei: neither of these neutron numbers is a magic number in stable nuclei. With the new experimental data, a shell closure at $N = 32$ is confirmed for these nuclei, while no indication for a closure at $N = 34$ is apparent. This result is consistent with other experimental work on these and neighboring nuclei. Calculations, on the other hand, are not yet able to fully reproduce the newly obtained results.

Finally, a brief summary is presented. Appendices describe some by-products of the present work.

2. Concepts and Tools

This chapter contains an introduction to concepts and tools upon which the present work is based. None of them is new in the sense that they were results from this work, so they will not be elaborated in great detail. Instead, a brief summary of the most important points will be given with references to literature where more details may be found.

2.1. The Independent Particle Shell Model

The structure of the periodic table of chemical elements is determined by the electron shell structure of the atoms. This structure becomes visible, e.g., in the electron separation energies which have maxima for the noble gases.

Already more than half a century ago, a similar structure was observed in atomic nuclei known at that time. Jumps in the nucleon separation energies S_p (for protons) and S_n (for neutrons) are visible at certain *magic numbers*. These are located at proton numbers $Z = 2, 8, 20, 28, 50$ and 82 and at neutron numbers $N = 2, 8, 20, 28, 50, 82$ and 126. In analogy to the electron shells of the atom, closed proton and neutron shells can be expected for these nucleon numbers, i.e. a large energy distance to the next orbital.

In contrast to the atom, no central potential exists a priori in the nucleus. Within the framework of the shell model, it is assumed that such a central potential is created by the nucleons themselves, i.e. the Hamiltonian is split into two parts,

$$\hat{H} = \hat{H}_0 + \hat{V}_r \quad \text{with} \quad \hat{H}_0 = \sum_i (\hat{T}_i + \hat{V}_i) \quad \text{and} \quad \hat{V}_r = \sum_{i<j} \hat{V}_{i,j} - \sum_i \hat{V}_i \tag{2.1}$$

where $\hat{H}_0$ includes only the mean field $\hat{V}_i$, and the residual interaction $\hat{V}_r$ is the difference between the mean field and the two-body interactions $\hat{V}_{i,j}$. Three-body interactions and higher terms are ignored. The residual interactions can be small if a suitable mean field is chosen, and are, therefore, neglected in the independent particle shell model. In this model, the nucleons interact only indirectly via the mean field. In addition they have to obey the Pauli principle. The central potential is usually approximated by a square well, harmonic oscillator, or Woods-Saxon potential (see figure 2.1). The breakthrough for the shell model was the observation by Goeppert-Mayer [Goe49], and Haxel, Jensen and Suess [HJS49] that the interaction between the angular momentum l and the spin s of the nucleons is much more important in the nucleus than for the electrons in an atom. The magnitude of this interaction is of the same order as the shell gaps, so it strongly affects the shell structure and must be included in $\hat{H}_0$ with an additional term $\hat{V}_{ls} = V_{ls}(r)\ \hat{\boldsymbol{l}} \cdot \hat{\boldsymbol{s}}$.

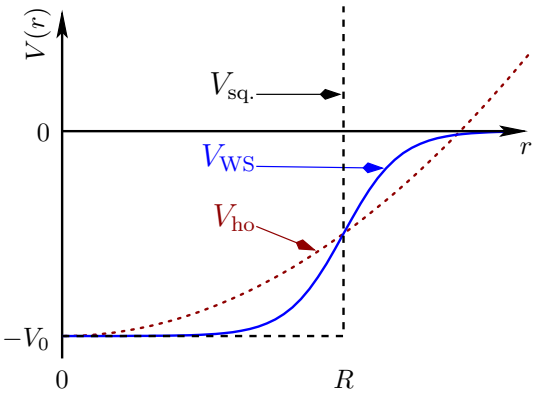

Figure 2.1.: Radial dependence of different mean potentials: square well $V_{\mathrm{sq.}}$, harmonic oscillator V_{ho}, and *Woods-Saxon* potential $V_{\mathrm{WS}}(r) = -V_0/\left(1+\exp\left[{}^{(r-R)}/_{a}\right]\right)$ (drawn here for $R = 10a$). The latter reproduces the measured density distribution in nuclei quite well, but it does not allow the solutions of the Schrödinger equation to be given in closed form [MRRS88].

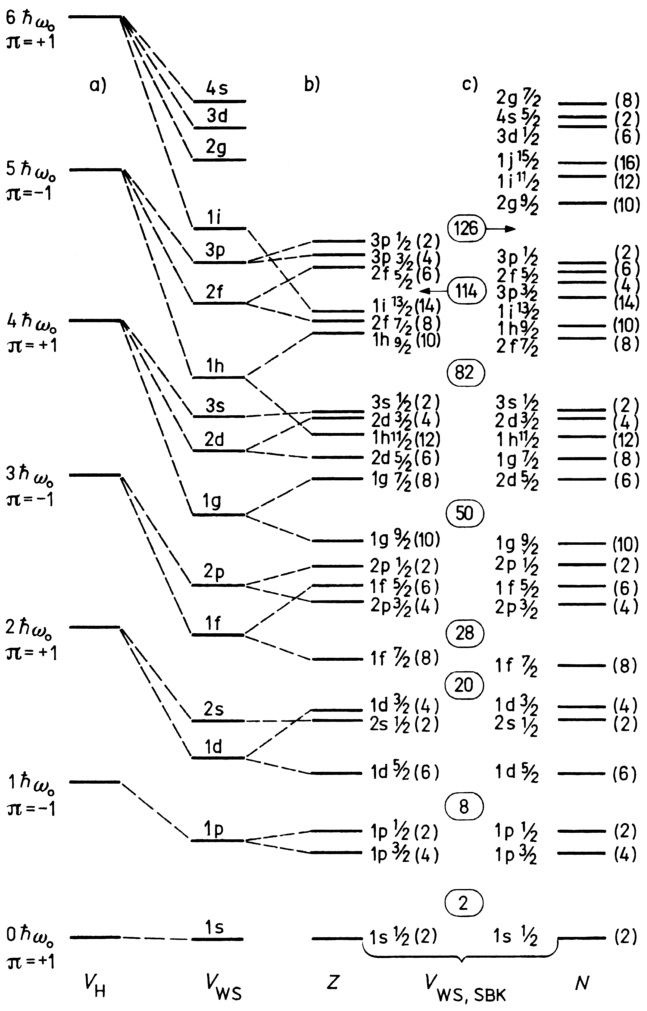

Figure 2.2.: Single-particle energies from the shell model [MRRS88, fig. 8.12, p. 305] **a)** for a harmonic oscillator V_{H}, **b)** for a Woods-Saxon potential V_{WS} and **c)** additional ls coupling and Coulomb correction, $V_{\mathrm{WS,SBK}}$.

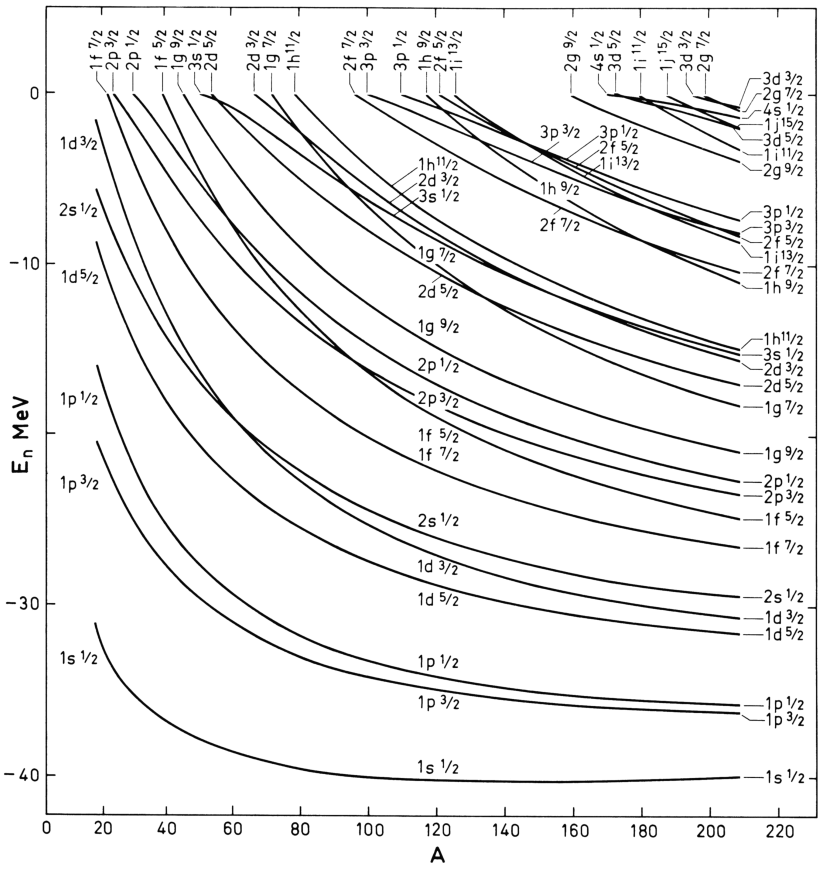

Figure 2.3.: Single-particle energies as a function of the nucleon number A [Cas00, fig. 3.8]. Because of the growth in nuclear size, the energies change approximately as $E \sim 1/r^2 \sim A^{-2/3}$ with a small dependence on the angular momentum due to the change in spatial distribution with l. In addition, there are effects of the residual interactions.

Figure 2.2 shows that the observed magic numbers can be reproduced within this model. The figure is illustrative only, but it helps to get an idea where the individual proton and neutron orbits are roughly located. As the mean field is created by the nucleons themselves, energies and shell gaps vary with the nucleon number. This is shown in figure 2.3. For a more detailed understanding of the nuclear structure, the residual interactions may not be ignored.

Before considering the residual interactions, other signatures of shell structure shall be mentioned briefly. The energy of the first excited state $E(2^+)$, the energy ratio of the first 4^+ to the first 2^+ state, and reduced transition probabilities $B(E2; 0_1^+ \rightarrow 2_1^+)$ are shown for calcium isotopes (magic proton number $Z = 20$) between $A = 40$ (magic neutron number $N = 20$) and $A = 48$ (magic neutron number $N = 28$) in figure 2.4. For the nuclei with magic neutron numbers, the $E(2^+)$ curve shows maxima, and the other two curves show minima. This behavior is typical for magic nuclei and the isotopes in-between. We will come back to the $E(2^+)$ in chapter 3, and to the reduced transition probabilities $B(E2)$ in chapter 4.

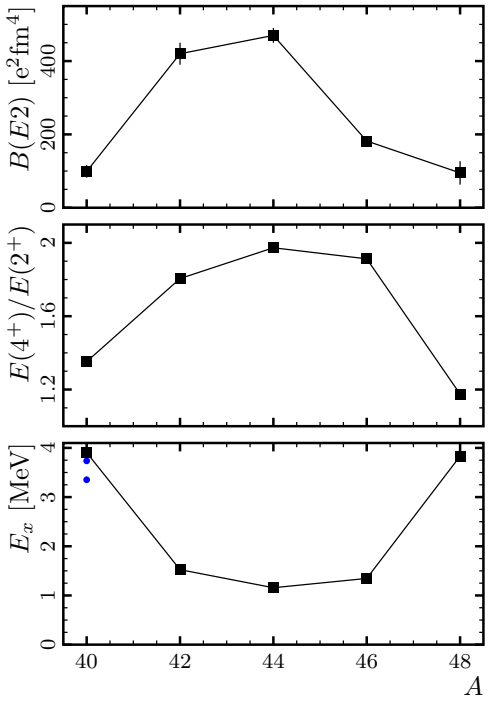

Figure 2.4.: Signs for shell structure in even Ca isotopes for neutron numbers $N = 20$ to 28: while the $E(2^+)$ (lower panel, [ENS07]) show maxima, the ratios $E(4^+)/E(2^+)$ (middle panel, [ENS07]) and the $B(E2)$ values (upper panel, [RNT01]) show minima at the magic numbers (cf. [Cas00, p. 33]). The first excited states of ^{40}Ca (●) are, in this order, a 0^+ and a 3^- state.

2.2. Residual Interactions

The picture drawn so far applies mainly for stable nuclei. While the basic structure remains valid for most of the nuclear chart, the details of the level structure may change. For exotic nuclei, even the magic numbers may disappear in the sense that the typical signatures for magic nuclei are no longer present, or new magic numbers may appear. These effects appear with changes in neutron and proton number, and they are caused by the residual interaction of the nucleons.

For example, Bastin *et al.* [BGS$^+$07] have shown recently that $N = 28$ is no longer a magic number for $^{42}_{14}$Si. The energy of the first excited 2^+ state in this nucleus was determined to be only 770(19) keV which is lower than in the neighboring even Si isotope, ^{40}Si (where $E(2_1^+) = 986(5)$ keV), and much lower than in the Ca isotope with $N = 28$ (where $E(2_1^+) = 3832$ keV).

For the nucleus ^{30}Si with $Z = 14$ and $N = 16$, Otsuka *et al.* [OFU$^+$01] calculate a large energy gap between the neutron orbits $d_{3/2}$ and $f_{7/2}$, which is the well-known $N = 20$ shell closure. But, within the same model, this energy gap almost vanishes for ^{24}O with $Z = 8$ and $N = 16$. In this nucleus, a new gap appears between the neutron orbits $s_{1/2}$ and $d_{3/2}$. This means that removing six protons from the filled $d_{5/2}$ orbit in ^{30}Si made the $N = 20$ shell closure disappear and made a new shell closure appear at $N = 16$.

Both experiments performed within the framework of this thesis are investigating such effects leading to a different shell structure in exotic nuclei. The experimental results are

later compared to theoretical shell model calculations. The residual interactions used in these calculations shall now be presented briefly.

Each of these interactions also contains a description of the mass dependence of single-particle energies, similar to what is shown in fig. 2.3.

2.2.1. Interactions for the fp Shell

In the experiment on Cr isotopes described in chapter 4, a presumed shell closure at $N = 32$ is investigated. Calculations for these Cr nuclei need an interaction suitable for the fp shell, i.e. for nuclei between ^{40}Ca and ^{100}Sn. The two sets of such residual interactions that have been used for comparisons to experimental results in this work are the *GXPF1* and *KB3G* interactions.

The GXPF1 interactions. The GXPF1 interaction [HOBM04] for the fp shell is based on matrix elements derived by Hjorth-Jensen *et al.* [HJKO95] (who extensively describe the derivation of the matrix elements via the G-matrix formalism). The matrix elements and single-particle energies defining the residual interaction of the latter were fitted to reproduce experimental energies in 87 nuclei in the range between $^{47}_{20}$Ca and $^{65}_{32}$Ge. This fit was performed for a limited set of matrix elements. A simplified shell model calculation was used to reduce the amount of computer time needed for the fitting procedure. As a result of the fit, a new set of matrix elements was obtained. With these matrix elements, the mean level deviation between the fit input and the shell model calculations is around 170 keV [HOBM04]. With the new matrix elements, predictions can be attempted also for nuclei and nuclear properties outside the range of the fit. One such prediction was that a large gap should appear between the neutron shells $2p_{1/2}$ and $1f_{5/2}$ (see fig. **2.3** for $A \approx 50$, cf. fig. 2.2) for small Z. In other words: a substantial shell gap was predicted for neutron number $N = 34$ in fp-shell nuclei near $Z = 20$, i.e. for Ca, Ti and Cr (regarding only the even Z). This shell gap is investigated in the experiment described in Chapter 4.

The KB3 interactions. The series of 'KB' interactions is based on work by Kuo and Brown [BK66; BK67; KB68] who have derived a residual interaction starting from the Hamada-Johnston nucleon-nucleon potential [HJ62]. These KB interactions were later modified by manual tuning to experimental data, leading to the interactions KB3 [PZ81] and KB3G [PSCN01].

2.2.2. Interactions for the sd Shell

For the experiment on ^{36}Ca, an interaction for the *sd* shell is needed. This shell includes the nuclei between $^{16}_{8}$O and $^{40}_{20}$Ca.

The USD interaction. A commonly used interaction for the *sd* shell is the *USD* interaction [BW88; Wil84]. In this interaction, differences in excitation energies between mirror nuclei are ignored or averaged out. In a similar way as for GXPF1 (but chronologically

before), two-body matrix elements were fitted to experimental binding and excitation energies, starting from matrix elements derived by Kuo [Kuo67]. This interaction has been used for the calculation of spectroscopic factors in Chapter 3.

Recently, revisions of the USD interaction have been published [BR06] which are based on an enlarged set of experimental data.

The sdpf interaction. The *sdpf* interaction has recently been developed for neutron-rich nuclei around $N = 28$ [CNP02; RCNP97]. It includes both the *sd* and the *fp* shell and thus allows, e.g., to include excitations across the $Z, N = 20$ shell closures in the Ca isotopes. It is based on the USD interaction for the *sd* part, and on a modified KB interaction for the *fp* part. The cross-shell interaction was derived from work of Lee, Kahanna, and Scott [KLS69] by a fitting procedure.

2.2.3. Effects in Exotic Nuclei

As described above, residual interactions used in the present work were derived by starting from a set of matrix elements calculated from nucleon-nucleon scattering data and adapting them to experimental data using a fitting procedure. Most of the experimental data used for these fits are from nuclei near the stability line (cf. [BR06; HOBM04]).

For exotic nuclei, large proton-neutron (isospin $T = 0$, see sec. 2.5) two-body matrix elements (TBME) may lead to shifts in the level energies if one of the two orbits related by a TBME is less filled due to an 'exotic' ratio of proton and neutron numbers compared to nuclei near the stability line. For example, when going from Ni towards Ca in the nuclear chart, large TBME $< jj'|V|jj' >_{T=0}$ with $j = \pi 7/2$ and $j' = \nu 5/2$ may cause a shift of the neutron $f_{5/2}$ orbit up in energy due to the removal of 'proton partners' from the $f_{7/2}$ sub-shell. Such matrix elements are actually found to be among the strongest binding TBME in the *fp* shell (cf. [HOBM04, fig. 1]) leading to the prediction of the $N = 34$ gap.

Measurements in exotic nuclei can therefore help to determine such matrix elements.

2.3. Reduced Transition Probabilities and Coulomb Excitation

The experiment to study heavy Cr isotopes (chapter 4) made use of the intermediate-energy Coulomb excitation technique to study reduced transition probabilities $B(E2)$.

2.3.1. Reduced Transition Probabilities

The lifetime of an excited state decaying by γ-ray emission is determined by the transition energy, its multipolarity and the transition matrix elements. Reduced transition probabilities for transition type σ (magnetic or electric) and multipolarity L are defined as [Hey94, p. 155]

$$B(\sigma L; J_i \rightarrow J_f) = \sum_{M,M_f} |\langle \alpha_f; J_f M_f | \mathcal{O}(\sigma LM) | \alpha_i; J_i M_i \rangle|^2 . \tag{2.2}$$

where the $\alpha_{i,f}$ denote quantum numbers specifying the states. For an equal population of the initial substates M_i, this reduces to

$$B(\sigma L; J_i \to J_f) = \frac{1}{2J_i+1} \left|\langle \alpha_f J_f || \mathcal{O}(\sigma L) || \alpha_i; J_i \rangle\right|^2 . \tag{2.3}$$

For initial and final states expanded as

$$|\alpha_i; J_i M_i\rangle = \sum_k a_k(J_i)|k; J_i M_i\rangle \quad \text{and} \quad |\alpha_f; J_f M_f\rangle = \sum_l b_l(J_f)|l; J_f M_f\rangle, \tag{2.4}$$

the expression can be generalized to

$$B(\sigma L; J_i \to J_f) = \frac{1}{2J_i+1}\Big|\sum_{k,l} a_k(J_i) b_l(J_f) \langle l; J_f || \mathcal{O}(\sigma L) || k; J_i\rangle\Big|^2 \tag{2.5}$$

where enlarged transition rates can result for some cases (collective transitions) when all partial contributions have the same phase [Hey94, p. 156]. Swapping initial and final states in eq. (2.3), the reduced transition probabilities change by a factor

$$\frac{B(\sigma L; J_i \to J_f)}{B(\sigma L; J_f \to J_i)} = \frac{2J_f+1}{2J_i+1} \tag{2.6}$$

The lifetime τ and decay width Γ corresponding to a $B(\sigma\lambda)$ value are [BG77; RN67]

$$\Gamma(\sigma\lambda; I_i \to I_f) = \frac{\hbar}{\tau} = \frac{8\pi(\lambda+1)}{\lambda[(2\lambda+1)!!]^2}\Big(\frac{E_\gamma}{\hbar c}\Big)^{2\lambda+1} B(\sigma\lambda; I_i \to I_f) \tag{2.7}$$

with the transition energy E_γ. For electrical quadrupole radiation, commonly used units are $\mathrm{e^2fm^4} = 10^4\mathrm{e^2b^2}$, and *Weisskopf units* (W.u.) The latter are defined as [Gra04]

$$B(E\lambda; I_i \to I_{\text{g.s.}}) = \frac{1}{4\pi}(1.2)^{2\lambda}\Big(\frac{3}{\lambda+3}\Big)^2 A^{2\lambda/3} \quad \mathrm{e^2fm^{2\lambda}}. \tag{2.8}$$

It is important to note that they depend not only on the multipolarity of the transition, but also on the mass A of the nucleus.

For the $0_1^+ \to 2_1^+$ transition in a $K = 0$ rotational band, the $B(E2)$ value can be related to the intrinsic quadrupole moment Q_0 of the nucleus [Cas00, p. 217]:

$$B(E2; 0_1^+ \to 2_1^+) = \frac{5}{16\pi} e^2 Q_0^2. \tag{2.9}$$

K is the projection of the total angular momentum J on the symmetry axis (i.e. the rotation is perpendicular to the symmetry axis for $K = 0$). Therefore, the $B(E2)$ value contains information on the deformation of the nucleus. This deformation is expected to be small for nuclei with a closed proton or neutron shell.

As shown in figure 2.4, minima in the $B(E2)$ values are visible for the doubly magic Ca isotopes ^{40}Ca and ^{48}Ca. A similar behavior is observed throughout the nuclear chart (cf. [Cas00, fig. 2.16]): at closed shells, the $B(E2)$ values show minima (indicating small deformation), whereas in mid-shell regions, higher $B(E2)$ values (corresponding to larger deformation) are observed.

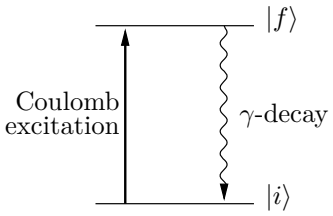

Figure 2.5.: Schematic illustration of first-order Coulomb excitation followed by γ-decay [Gla98, fig. 8].

2.3.2. Coulomb Excitation

Coulomb excitation is the excitation of a target nucleus by the electromagnetic field of the projectile, or vice versa [WA79]. The excitation and de-excitation are illustrated in fig. 2.5. The application of this process in intermediate energy (30 ... 300 MeV/u) experiments is described in the review article by Glasmacher [Gla01] which refers to the calculations presented by Winther and Alder [WA79].

The cross section for the excitation process can be calculated in detail for low energies, i.e. for energies below the Coulomb barrier. At these energies, the charge distributions of the two nuclei cannot overlap due to the Coulomb repulsion, and that allows only electromagnetic interaction.

For the intermediate energies, the cross section for the Coulomb excitation process was calculated in a semicassical approximation. The cross section depends on the minimum impact parameter. In the intermediate energy regime it is calculated as (see [Gla01])

$$b_{min} = \left(\cot\left(\frac{\theta^{cm}_{max}}{2}\right) + \frac{\pi}{2}\right)\frac{Z_p Z_t e^2}{\gamma m_0 v^2} \tag{2.10}$$

with the maximum scattering angle in the center of mass system θ^{cm}_{max}, the target and projectile charges Z_t and Z_p, the reduced mass of the two nuclei m_0, $\gamma^{-2} = 1 - v/c$ and the velocity v of the projectile in the laboratory system. The calculation for the cross section yields [Gla01]

$$\sigma \approx \left(\frac{Ze^2}{\hbar c}\right)^2 \frac{B(E\lambda, 0 \to \lambda)}{e^2 b^{2\lambda-2}_{min}} \frac{1}{\lambda - 1} \tag{2.11}$$

for the multipolarity of the transition $\lambda \geq 2$, the charge of the target nucleus Z in the case of projectile excitation. Due to the Z^2 dependence of the cross section, it is advisable to use a target material with large Z.

Due to the proportionality of σ and $B(E2)$, reduced transition probabilities can be obtained from measurements of Coulomb excitation cross sections. This possibility has been used in chapter 4 to investigate the behavior of $B(E2)$ values for Cr isotopes with $N = 32$ and 34.

Figure 2.6 compares the Coulomb excitation cross section with other processes, namely excitation of giant dipole resonances (GDR) and giant quadrupole resonances (GQR) as a function of the beam energy. At around 100 MeV/u, the Coulomb excitation cross section dominates the other two displayed components by a factor of at least 5. At intermediate energies and above, one-step processes are dominating the population of excited states, i.e. the direct transition from the ground state to the excited state, and

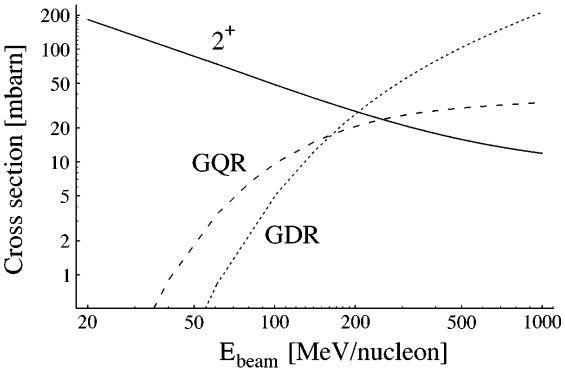

Figure 2.6.: Comparison of the cross sections for Coulomb excitation (labeled 2^+), the giant dipole resonance (GDR), and the giant quadrupole resonance (GQR) for a ^{40}S beam incident on a Au target, for beam energies between 20 and 1000 MeV/u. The calculation assumes a minimum impact parameter of 16 fm [Gla98, fig. 1].

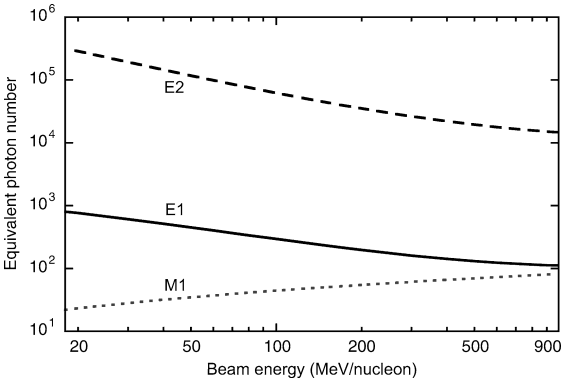

Figure 2.7.: Comparison of equivalent photon numbers for Coulomb excitation for E2, E1, and M1 transitions for the reaction ^{40}S+^{197}Au at different beam energies [Gla01, fig. 2]. The cross section is proportional to the equivalent photon number.

among these, E2 transitions are favored [Gla01] (see fig. 2.7). Therefore, the Coulomb excitation process populates predominantly the first 2^+ states in even-even nuclei.

2.4. Knockout Reactions

In the second experiment performed within the framework of this thesis, nuclei around ^{36}Ca have been studied by coincident γ-ray and particle spectroscopy.

The reaction of interest was the one-neutron knockout from ^{37}Ca, leading to ^{36}Ca in the ground or an excited state. In the experiment, γ rays and particle momenta parallel to the beam direction were measured in coincidence, so that the momenta can be assigned to reactions populating specific excited states (if a specific γ ray was measured in coincidence) or to the ground state. From the distribution of the momenta, conclusions may be drawn on the state of the neutron that was removed in the reaction.

2.4.1. Simple Picture of the Knockout Process

First, a very simple picture of the knockout process shall be drawn to give an idea of the expected results without any formalism.

The starting point is that the reaction channel is fixed by the particle identification before and after the target. This implies, in the present case, that one neutron has to be removed from the incoming nucleus to produce the observed residual nucleus. From

the requirement that one neutron is removed, it is natural to conclude that the reaction is probing mainly the nuclear surface of the incoming nucleus: for a central collision, it is likely that more than one nucleon is removed, or that other reactions occur. This already leads to a prediction on the width of the momentum distributions of the observed residual nuclei: these distributions reflect the momentum of the removed nucleon, and according to $\boldsymbol{l} = \boldsymbol{r} \times \boldsymbol{p}$ this is, as the range of radii is limited by the surface localization, correlated with the angular momentum of the struck nucleon. Therefore, the width of the momentum distribution parallel to the beam axis is expected to be wider for larger l. This behavior is indeed observed experimentally.

2.4.2. Outline of the Knockout Process Calculation

The calculation of momentum distributions and cross sections in chapter 3 have been carried out using the computer code `momdis` [BG06]. An outline of the procedure used in this code shall now be given.

As in many quantum-mechanical problems, the theory is not very pictorial until the end. Therefore some details are skipped here, assuming that they are better described elsewhere. The code itself is described in detail in [BG06], and of course the ultimate description of the procedure is the `FORTRAN` code that is available together with the article. Beyond this, helpful explanations may be found in the references listed in the article, especially [BD04, ch. 8], and [BH04; Tos01; HBE96].

An important approximation made in the calculation is that the process is treated as a three-body problem involving the target (t), the residue or core (c), and the removed valence nucleon (v). The incoming beam particle is regarded as a bound system of $c+v$, and c is the final state of the observed residue (^{36}Ca in the present case) which is thus assumed to be pre-formed in the incoming system.

The quantum numbers nlj of the nucleon v are chosen as an input for the calculation. The nucleon wave function is calculated by solving the Schrödinger equation for a Woods-Saxon potential with a spin-orbit term and, for protons (i.e. not in the present case), the Coulomb potential. The depth and radii of these potentials are input parameters chosen to reproduce the effective separation energy of the nucleon (i.e. the separation energy plus the excitation energy) and the nuclear radius. Residual interactions are assumed to be negligible.

The program can use scattering matrices provided by the user, or calculate such matrices using the $t\rho\rho$-approximation. The latter option has been chosen for the calculations performed for this work and the approximation shall be outlined now.

In the $t\rho\rho$ approximation, the structure of two interacting nuclear systems A and B is approximated with density functions ρ_A and ρ_B, respectively. Then, the reaction is described by an integration of the individual interactions of the nucleons, described by a profile function $t(\boldsymbol{b})$, weighted with the density functions. Figure 2.8 illustrates the geometry of the problem. The probability $T(\boldsymbol{b})$ for a nucleon-nucleon collision in the collision of nuclei A and B is then [BD04, eq. (8.5)]

$$T(\boldsymbol{b}) = \int \rho_B(\boldsymbol{b}_B, z_B) d\boldsymbol{b}_B \rho_A(\boldsymbol{b}_A, z_A) d\boldsymbol{b}_A t(\boldsymbol{b} + \boldsymbol{b}_B - \boldsymbol{b}_A) \tag{2.12}$$

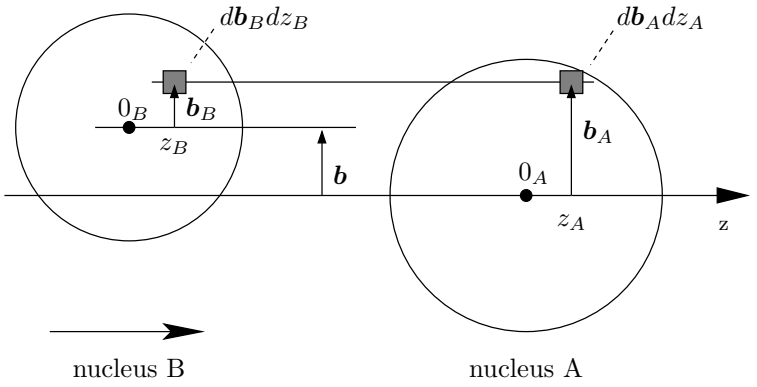

Figure 2.8.: Geometry of the scattering nuclei for the knockout calculations [BD04, fig. 8.1].

with the symbols as in the figure. With a Fourier transformation and an integration of the densities along the z axis,

$$T(\boldsymbol{b}) = \frac{1}{2\pi} \int J_0(qb)\tilde{\rho}_A(q)\tilde{\rho}_B(-q)f_{NN}(q)qdq \tag{2.13}$$

where J_0 is a Bessel function, and the $\tilde{\rho}$ are the Fourier transforms of the nuclear densities. The function f_{NN}, defined by

$$t(\boldsymbol{b}) = \frac{1}{(2\pi)^2} \int e^{-i\boldsymbol{q}\cdot\boldsymbol{b}} f_{NN}(q)d^2q, \tag{2.14}$$

is the Fourier transform of the profile function.

The density functions used in the calculations for this work are Gaussian distributions (cf. [GBB+04a]). Use of this approximation with fixed impact parameters implies that the relative motion of c and v during the reaction is neglected. This *sudden approximation* is valid for high projectile energies [HT03, sec. 3.5].

The reaction cross section contains two parts: the elastic breakup of the incoming nucleus, also called *diffractive* breakup, and the inelastic breakup or *stripping*. The elastic breakup is described by an interference of the elastically scattered waves of c and v. This cross section includes processes where both c and v are at most scattered elastically on the target and form an unbound state after the reaction. The inelastic breakup, on the other hand, comprises processes where at least one of c and v is 'absorbed' in the target, which is excited from its ground state.

The calculation of total cross sections in `momdis` accounts for these two processes separately. Scattering matrices for an 'impact parameter' b are calculated as

$$S(b) = \exp[i\chi(b)] \qquad \text{with} \qquad \chi(b) = \frac{1}{k_{NN}} \int J_0(qb)\tilde{\rho}_A(q)\tilde{\rho}_B(q)f_{NN}(q)qdq. \tag{2.15}$$

Here the phase shift $\chi(b)$ includes $T(b)$ from (2.13), and f_{NN} is parametrized as

$$f_{NN}(q) = \frac{k_{NN}}{(4\pi)^2}\sigma_{NN}(i + \alpha_{NN}) \exp(-\beta_{NN}q^2) \tag{2.16}$$

with tabulated coefficients σ_{NN}, α_{NN} and β_{NN}. The phase shift due to the Coulomb interaction is added as χ_C. According to [BG06; HBE96], the two cross section contributions can then be written as

$$\sigma_{\text{el.bup}} = \sum_m \left[\langle\phi_0|(|\hat{S}_v|^2|\hat{S}_c|^2)|\phi_0\rangle - |\langle\phi_0|(\hat{S}_v\hat{S}_c)|\phi_0\rangle|^2 \right] \tag{2.17}$$

and

$$\sigma_{\text{inel.bup}} = \frac{\pi}{k^2} \sum_m \left[\langle\phi_0|(|\hat{S}_c|^2(1-|\hat{S}_v|^2))|\phi_0\rangle \right] \tag{2.18}$$

where ϕ_0 is the wave function of the projectile, and $\hat{S}_v$ and $\hat{S}_c$ the scattering matrices for interaction of the valence nucleon and the core, respectively, with the target. The latter equation includes the terms $|\hat{S}_c|^2$ and $1-|\hat{S}_v|^2$, the former of which describes the probability that the residue c survives the reaction, and the latter that the nucleon is absorbed [Tos01]. These integrals are evaluated in the code to calculate the two components of the reaction cross section.

For the calculation of momentum distributions, it is assumed that the shape of the distribution is the same for the elastic and inelastic breakup channels [BG06]. The distribution $(p_\parallel, p_\perp)$ is calculated only for the inelastic channel and then scaled to reproduce the total cross section using the expressions for

$$\frac{d\sigma_{\text{inel.bup}}}{d^3k} \tag{2.19}$$

given in [HBE96]. Presently, parallel and transverse momentum distributions cannot be calculated for the diffractive part of the cross section within the model presented here. The cross section for stripping is typically larger by a factor two, so that the scaled distribution mainly contains the 'correctly' calculated part. Nevertheless, a calculation of both parts would be desirable and is being investigated [Gad07].

The simple description given in the previous section appears again in the $t\rho\rho$ approximation. The process is assumed to be independent of the spin of the valence particle [BG06]. Therefore, j appears only in the quantum numbers for the wave-function calculation.

2.4.3. Spectroscopic Factors

In the calculations described above, cross sections are calculated for the reaction of the $c+v$ system with the target, where v is in a specific state nlj. The calculations do not account for the structure of the incoming nucleus: occupation probabilities of the nlj state are ignored in the `momdis` calculation. Therefore, the calculated cross sections are *single-particle* cross sections σ_{sp}: they apply to a situation where exactly one nucleon is in the specified state.

The relation to occupation probabilities has to be calculated within the shell model. For initial and final wave functions Ψ_i and Ψ_f of the initial nucleus with mass A and the final nucleus of mass $A-1$, respectively, the overlap after a knockout reaction can

be expanded in terms of one-particle wave functions as [HT03]

$$\langle \Psi_c(1,\ldots,A-1) \otimes \Psi_v(A) | \Psi_{c+v}(1,\ldots,A) \rangle_{\boldsymbol{r}_v} = \sum_j c_j \psi_j(\boldsymbol{r}_v) \tag{2.20}$$

(with details of the angular momentum coupling not shown, as in [HT03]) with the spectroscopic amplitudes c_j. The spectroscopic factors are $S_j = |c_j|^2$. They relate the single-particle cross sections σ_{sp} and the expected cross section

$$\sigma_{\mathrm{theo}} = \sum_j S_j \sigma_{\mathrm{sp}}(nlj). \tag{2.21}$$

Here, the spectroscopic factors contain the nuclear structure information, while the σ_{sp} are related to the reaction mechanism.

Spectroscopic factors can be calculated using a shell model code like, e.g., `antoine` [Cau04; CN99]. This was done in chapter 3 using the USD interaction for ^{37}Ca and ^{36}Ca.

On the other hand, experimental spectroscopic factors may be determined by comparing experimental and single-particle cross sections. Thereby, a knockout experiment can yield, at the same time, information on the angular momentum l of the removed particle and on the occupancy of the shell where the particle was removed from.

2.5. Isospin

The concept of isospin may be used, e.g., to distinguish between nuclei which have the same nucleon number A but differ in their proton and neutron numbers Z and N, respectively.

Within the isospin formalism, the proton and the neutron are treated as two states of the same particle, the nucleon [Cas00; BL06]. The concept is based on the observation that the strong interaction between nucleons is approximately charge-symmetric and charge-independent. The Coulomb interaction, which applies only to protons, is neglected.

The nucleon is assigned an isospin quantum number $\boldsymbol{T}$, with a projection quantum number

$$T_z = +\frac{1}{2} \quad \text{for the neutron state, and} \quad T_z = -\frac{1}{2} \quad \text{for the proton state.} \tag{2.22}$$

The choice of the sign is a matter of convention (the opposite assignment may also be found in the literature; $-\frac{1}{2}$ for protons is used in [Cas00; BL06]). For a multi-nucleon system, T_z is the algebraic sum of the individual T_z, or

$$T_z = \frac{N-Z}{2}. \tag{2.23}$$

This implies that mirror nuclei, i.e., nuclei a and b with $N_a = Z_b$ and $N_b = Z_a$, have opposite signs of T_z: $T_{z,a} = -T_{z,b}$. The possible values of $\boldsymbol{T}$ depend on the configuration of the system (see [Cas00, p. 84$^+$]).

3. Structure Investigations of ^{36}Ca

With the advent of high-intensity, high-energy radioactive beams, the comparison of properties of mirror nuclei has regained larger interest among nuclear physicists. As for heavier nuclei the neutron number exceeds the proton number, the mirrors of heavier stable nuclei around mass $A \approx 40$ lie far away from the β-stability line. They become accessible for in-beam spectroscopy only gradually. The present investigation looks at the $A = 36$, $T = 2$ mirror pair formed by ^{36}Ca and ^{36}S, and at their $A + 1$ neighbors ^{37}Ca and ^{37}Cl. While these Chlorine and Sulfur isotopes are stable, the two Calcium isotopes have half-lives of 181.1(10) ms ($A = 37$) and 102(2) ms ($A = 36$), respectively. Calcium isotopes are of special interest because of the $Z = 20$ shell closure, but little was known on Ca isotopes lighter than $A = 38$. It is not yet known if ^{34}Ca has a bound ground state. Ground-state spins and nuclear lifetimes for $A = 35 \ldots 37$ were known, but, except for one state in ^{37}Ca, no information on excited states existed.

Starting from the assumption of isospin independence of the nucleon-nucleon interaction, mirror nuclei should be identical in their structure. This symmetry is broken by the Coulomb interaction, which applies only to the charged protons, and turns identity to similarity in most cases. An experimental test of theoretical assumptions might yield confirmation, but also surprises may occur, and thereby input for an improved understanding can be obtained. This experiment was performed to provide such input.

In the nuclei ^{36}S and ^{34}Si, the excitation energies of the first 2^+ states are quite high. These states are located at 3291 and 3328 keV, respectively, and are thus not much below the excitation energy of the doubly-magic nucleus ^{40}Ca which has $E(2_1^+) = 3904$ keV. These high excitation energies might be a sign of large energy gaps between the proton $1d_{5/2}$, $2s_{1/2}$, and $1d_{3/2}$ orbitals. As a large energy gap is nothing else than a (sub-)shell closure, this indicates closed (sub)shells at $Z = 14$ and $Z = 16$. It is interesting to find out if these signatures can also be observed in the mirror nuclei, for $N = 14$ and $N = 16$. It is not known if ^{34}Ca has a bound ground state, but as calculations predict a very small proton separation energy [Col98], the observation of an excited state at high energy seems unlikely. But for ^{36}Ca, a similarly high excitation energy as in ^{36}S may be expected. The primary aim of the experiment was to measure this excitation energy.

Besides the excitation energies, shell occupancies are a very important nuclear property. Information on shell occupancies can be obtained from a measurement of spectroscopic factors, i.e. from a comparison of experimental and calculated single-particle cross sections (see sec. 2.4.3). Such spectroscopic factors can be derived from experiment by measuring momentum distributions of the one-neutron knockout residues ^{36}Ca. Comparing these spectroscopic factors to values calculated in a shell model framework can yield information on the shell occupancies.

This chapter is divided into several sections. In the first, section 3.1, a general de-

scription of a momentum distribution measurement is given, followed by a description of the concrete setup used in this experiment in section 3.2. Subsequently, the steps of the data analysis are detailed in section 3.3 which is followed by a presentation and discussion of the results in sections 3.5 and 3.6. Results for other nuclei than ^{36}Ca are briefly presented in appendix A.

3.1. Experimental Considerations

In the experiment, two aims should be achieved: The energy of the first excited 2^+ state in ^{36}Ca should be determined, and, secondly, momentum distributions and cross sections should be measured to gain information on the shell occupancies. The combination of both goals leads to some requirements for the experimental setup.

The possibility to achieve both aims in one experiment is based on the two-step fragmentation technique. Only beams of stable ions can be extracted from the ion source and then be accelerated. The stable isotope nearest to and heavier than ^{37}Ca is ^{40}Ca. A first fragmentation step—outside the experimental area—is used to produce a secondary beam of ^{37}Ca from the ^{40}Ca primary beam. Because this reaction is outside the experimental area, a very intense beam can be used without running into problems with background radiation and high counting rates of the detectors at the target position, e.g., from the large amount of γ rays emitted in the de-excitation of the large number of nuclei produced. Due to the long flight time to the experimental area compared to typical lifetimes of nuclear excited states, nuclei of the secondary beam may also be expected to be in their ground states when they arrive at the experimental target, except for possible isomeric states. In the experimental area, a second reaction follows where ^{36}Ca is produced by one-neutron removal from the secondary beam. As many of the nuclei produced in the first fragmentation step can be kept away from the experimental area, where the total acceptable rate is limited, a higher production of ^{36}Ca may be achieved. An example including rate considerations for a different experiment is given in [Sta03].

The cross section for the intended knockout reaction is of the order of 10 mb. A commonly used target material for such experiments is ^{9}Be, as it has a high purity (^{9}Be being the only stable isotope), low charge, low mass, and small γ-ray background (no bound excited state exist). Even for a thick Be foil of 200 mg/cm^2, as it was used in this experiment, only in the order of one in ten-thousand of the incoming ^{37}Ca ions undergo the desired reaction. Therefore it is necessary to use such a thick target to have a sufficient reaction rate. Passing through a thick target requires a high beam energy to avoid that the particles are stopped inside. In our case, particles may not be stopped in the target because it is necessary to identify them after the reaction. An important constraint on the possible target thickness is that the approximations and parametrizations used in the calculation of the momentum distributions are valid only for laboratory beam energies of more than 30 MeV/u (see sec. 2.4.2). Thus the beam energy should not be below this value in the target.

To measure momentum distributions for ^{36}Ca residual nuclei both for the first excited

2^+ state and in the ground state, γ rays and particle momenta have to be measured in coincidence. Two momentum distributions are measured: one where a γ ray was detected in coincidence with the ^{36}Ca ion, and the total, or inclusive distribution, where the γ-ray detectors are ignored. From these two, the distribution for the ground state can be calculated. For an accurate determination of both distributions it is therefore desirable to use a γ-ray detector with a high detection efficiency ϵ. A large ϵ decreases the error on the γ-coincident distribution due to the better statistics. Because the ground-state distribution is calculated by subtracting this distribution, scaled by $1/\epsilon$, from the inclusive one, it also reduces the error on the ground-state distribution.

A good energy resolution of the γ-ray detector is less important in the ^{36}Ca case. From the known level scheme of the mirror nucleus, ^{36}S, it is expected that the first two excited states—ignoring the 0^+-isomer which will not decay by γ-ray emission—are separated by around 1 MeV or 30 % of the excitation energy. Discriminating between such energies is possible with scintillation detectors.

Finally, it is necessary to select the reaction channel. As the secondary beam cannot be expected to contain only the desired ^{37}Ca, an identification of the incoming beam particles is necessary. For the products of the reactions in the secondary target, this is also inevitable, as many different types of reactions may occur. Because the different ions are not spatially separated, the identification has to be done event-by-event with specialized detectors.

These requirements were fulfilled by the setup described in the following.

3.2. Experimental Setup

The experiment was carried out at *GANIL* (Grand Accelerateur National d'Ions Lourds) in Caen, France. Figure 3.1 shows an overview of the accelerators and experimental halls of GANIL.

A primary beam of ^{40}Ca was accelerated to an energy of about 94.5 MeV/u in the two cyclotrons CSS1 and CSS2 (see top of figure 3.1). This beam energy corresponds to about 42 % of the speed of light.

3.2.1. Primary Target SISSI

To produce a secondary beam with ^{37}Ca, the ^{40}Ca ions must undergo a first reaction in a primary target, in which part of the beam particles make a fragmentation reaction and *lose* one or more nucleons.

At GANIL, this primary target is located in a device called *SISSI* (*Source d'Ions Secondaires à Superconducteurs Intense*) [BGO95] which receives the accelerated beam after extraction from the second cyclotron, CSS2. Its main components are a rotating target foil, and solenoids surrounding the foil which focus the ion beam. For a continuous adjustment of the matter thickness in beam direction, the target foil can be tilted around an axis perpendicular to the beam direction. For this experiment, a carbon foil with a thickness of $d_0 = 270\,\mathrm{mg/cm^2}$ was used. The foil was tilted to an angle of $\alpha = 25\,^\circ$ to

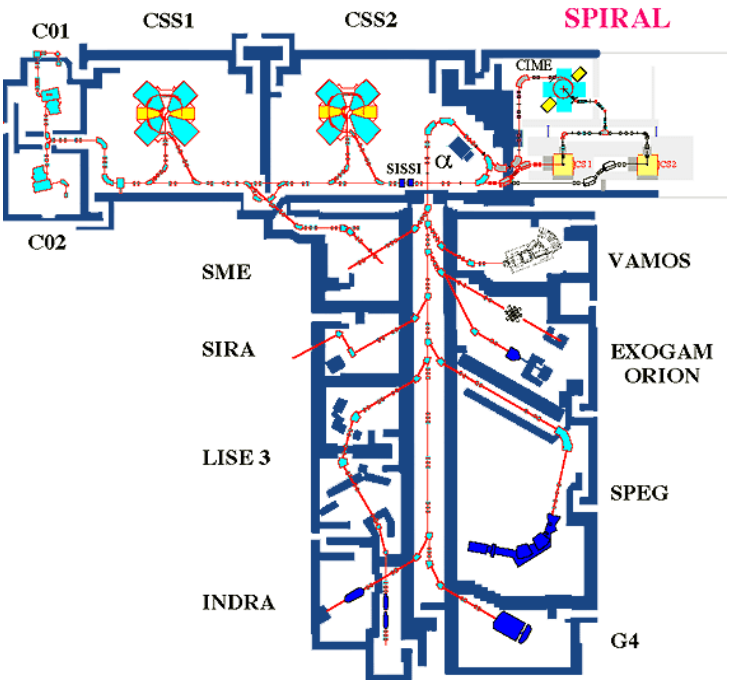

Figure 3.1.: Overview of the accelerators and experimental halls at GANIL [GAN07]. The beam was accelerated in the two cyclotrons CSS1 and CSS2, and then guided through SISSI, the α spectrometer, and the fishbone to the experimental hall of SPEG.

the beam axis, so that the beam had to pass through

$$d = d_0/\cos\alpha \approx 298\,\mathrm{mg/cm^2}$$

of carbon material. This setting was optimized during the experiment by varying the angle to obtain the maximum rate of ^{37}Ca in the experimental hall. After the primary target, the energy of the ^{37}Ca ions was about 71 MeV/u.

After passing through SISSI, the beam was composed of a mixture of ions containing both the primary beam and many different nuclear species, among them the desired ^{37}Ca. While the total beam intensity stays quite constant, the energy and composition of the beam are very different after the primary target. The calculation of expected production rates of the different isotopes shall not be detailed here. More information on this topic may be found in the literature [Tar04; SB02; GS91; GH78].

3.2.2. Alpha Spectrometer

After SISSI, the beam is guided through the α spectrometer. It serves as a filter to select the desired secondary beam of ^{37}Ca. This selection is important to reduce the beam intensity in the experimental hall and to obtain the maximum rate of the desired ions.

The spectrometer is named after its shape (see figure 3.1). It is built mainly from two consecutive dipole magnets and a *degrader* between them, plus quadrupole magnets for beam focusing. For the selection of the nuclear species the deflection of charged particles

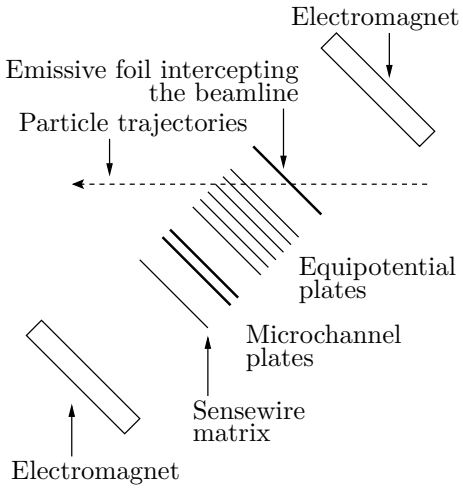

Figure 3.2.: Schematic view of a Galotte MCP detector [OMLS+96, fig. 1]. Beam particles release electrons from the emissive foil. These are guided to the amplifying micro-channel plates by a combined electric and magnetic field, and detected in the sense-wire matrix.

in the magnetic field of the dipoles is used. For the magnetic field B,

$$B\rho = \frac{p}{Q} = \frac{\gamma m v}{Q} \tag{3.1}$$

with $\gamma^{-2} = 1 - \beta^2$ and $\beta = v/\mathrm{c}$, the velocity v of the charged particle, and the speed of light c. With slits in the right position the part of the beam with the desired $B\rho$ can be selected. In our experiment, the dipoles were set to magnetic rigidities $B\rho_1 = 2,291\,\mathrm{Tm}$ before, and $B\rho_2 = 2,093\,\mathrm{Tm}$ after the degrader for the ^{37}Ca secondary beam.

The role of the degrader is to allow a selection of the charge of the particles by making use of the charge dependence of the energy loss dE/dx in material as described by the Bethe-Bloch equation [Leo94, sec. 2.2.3],

$$\frac{dE}{dx} = Z^2 f(v) \tag{3.2}$$

with a function f of the nucleus' velocity v, and the charge Z of the nucleus. A wedge-shaped foil is used to match energy loss, momentum and beam line geometry. For our experiment, the degrader for the ^{37}Ca selection was an aluminum foil of 521 µm thickness in the beam axis.

Despite setting the α spectrometer on ^{37}Ca, other nuclei reached the secondary target, some of them even with higher intensity than ^{37}Ca. Nevertheless, with this setting, the intensity of ^{37}Ca was maximized without exceeding the rate limitation of the detectors in the experimental hall.

3.2.3. Time-of-Flight Before the Secondary Target

At the exit of the α spectrometer, a multichannel-plate-detector (MCP) [OMLS+96] is set up for a measurement of flight times before the secondary target. The model used at GANIL is called *Galotte* (see figure 3.2). It was made use of its time resolution of better than 500 ps, but not of its position measurement capability.

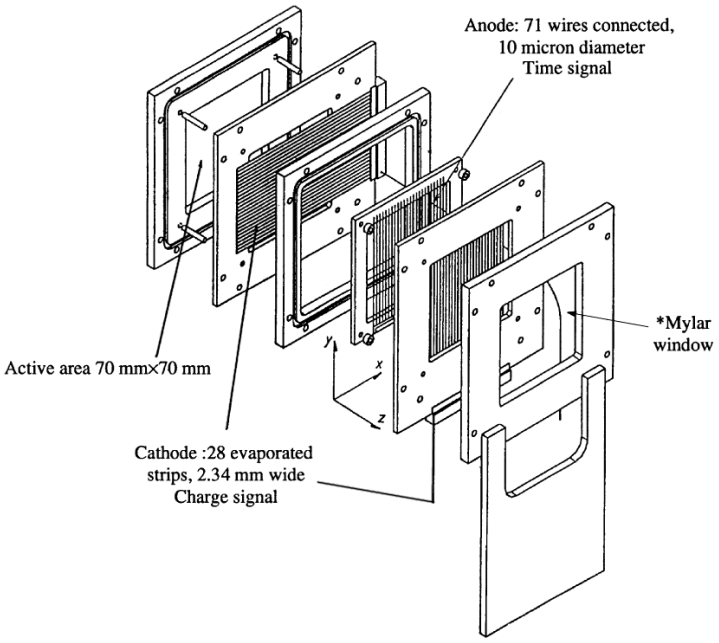

Figure 3.3.: View of the CATS MWPC detector [OMA$^+$99, fig. 2]. Beam particles passing through the detector ionize the gas. The electric field accelerates the charges and leads to a time signal on the anode, and to y and x position signals on the two cathodes.

A second detector for the time measurement was placed just before the secondary target. At the beginning of the experiment, this was a low-pressure multi-wire proportional counter (MWPC). Here, a model named *CATS* (Chambre A Trajectoires de Saclay) [OMA$^+$99] is used at GANIL (see fig. 3.3). It delivers an accurate time signal with a resolution of better than 500 ps, and allows for a determination of the position of the beam particles. (The latter ability was not used much, as there was only one such detector which does not permit trajectory reconstruction—but see figure 3.9 and section 3.5.3 on the reaction cross section.) In the course of the beam time, the MWPC detector was replaced by a second MCP detector of the same type as at the exit of the α spectrometer. To count the incoming beam particles, a scaler was connected to the detector before the target. For every 10000th particle, it triggered the data acquisition to store the time-of-flight values.

The purpose of both detectors is the identification of the secondary beam particles, although the detector at the target position is also used for other purposes to be described later. As the filtering with the α spectrometer leaves more than one component in the beam, it is necessary to identify individual beam particles to be able to select a particular reaction channel. With a measurement of the flight time t of each ion for the fixed distance s between the detectors, and with the known $B\rho$ value, the ratio of mass m to charge Z can be determined from eq. (3.1) inserting the velocity $v = s/t$.

The same method can be applied for a measurement of the time of arrival at one of the detectors relative to the high frequency of the cyclotron.

A determination of the Z of the secondary beam components was not foreseen in the setup. The selection in the α spectrometer is sufficient to let only one isotope pass for each Z.

Table 3.1.: Target thicknesses d deduced from measured $B\rho$ values with and without secondary target for different components of the secondary beam using the program LISE++ [TB03].

Nucleus		^{37}Ca	^{36}K	^{35}Ar	^{32}S	^{31}P	^{30}Si
$B\rho$ with	(Tm)	2.0932	2.0864	2.0783	2.1202	2.1060	2.0862
$B\rho$ without	(Tm)	1.6546	1.6498	1.6430	1.6766	1.6649	1.6492
d	(µm)	1091	1070	1045	1168	1123	1063

Figure 3.4.: The Château de Cristal is built of 74 BaF_2 detector crystals embedded in red aluminum cans. The PMTs extend beyond these cans. The name *crystal castle* is due to the geometry with all detectors aligned perpendicular to the beam plane.

3.2.4. Secondary Target

After the MWPC/MCP timing detector, the beam passes through the secondary target. This was a Be foil of about 198 mg/cm^2, or 1072 µm thickness. The energy of the secondary beam was about 60 MeV/u before and 38 MeV/u after the target.

The target thickness was determined experimentally. The ^{40}Ca primary beam was guided into SPEG, and the $B\rho$ value of the beam was measured with and without the target foil. From these two $B\rho$ values, the energy loss in the target can be calculated. Using the program LISE++ [TB03], the target thickness required to reproduce this energy loss can be determined.

In the program, the energy loss $dE(E)/dx$ is integrated over the target thickness. As these energy loss values are not known with high precision, the target thickness cannot be determined precisely. In table 3.1, thickness values calculated for different components of the secondary beam are listed. They were obtained from runs 164 and 166–169 before the start of the production runs (see table 3.2). Deviations of up to 100 µm have been obtained for the target thickness. In the following, a target thickness of 198(10) mg/cm^2, as measured with the primary beam, is assumed in the calculations.

3.2.5. Gamma-Ray Detectors – "Château de Cristal"

The secondary target was surrounded by the detectors of the *Château de Cristal* [Bec84]. It is built of 74 BaF_2 scintillation-detector crystals with hexagonal shape. The edges of

the crystals are 5 cm long, and the height of the crystals is 14 cm. Figure 3.4 shows that the crystals are aligned parallel to each other and perpendicular to the beam axis. The distance of the crystal front to the beam plane is 12.2 cm for the outer ring, and 32.3 cm for the innermost detectors to have a similar distance to the target for all detectors. A photomultiplier tube (PMT) is attached to each of the crystals. It is read out with a charge-to-digital converter (QDC).

The detector material contains some contaminants which are α emitters. The energy deposit from the α particles can be seen in the energy spectra. As the α decay is not correlated with the secondary beam particles, a narrow time gate for the particle-γ coincidence suppresses this background efficiently.

In addition to the Château de Cristal, three small Ge clover detectors from the EXOGAM array were placed around the target. They have a higher energy resolution than the BaF_2 detectors, but due to their lower detection efficiency they could not contribute to the in-beam γ-ray spectroscopy. Nevertheless their presence was very important for the experimental determination of the efficiency of the Château de Cristal. The high energy resolution allowed to make coincidence measurements of γ rays which could not have been resolved with the BaF_2 detectors.

3.2.6. Spectrometer SPEG

Finally, the beam reaches the spectrometer *SPEG* (Spectromètre à Perte d'Energie au GANIL) [BFG+89]. The main components of the spectrometer part are two large dipole magnets, two pairs of drift chambers, an ionization chamber and a beam-stopping plastic scintillator. Figure 3.5 shows a bird's view on SPEG.

In the dipoles, the charged particles are deflected according to their $B\rho$ value, as described by eq. (3.1). From a position measurement after the deflection, this $B\rho$ value can then be calculated.

The particle position in the $x-y$ plane is measured by the two pairs of drift chambers. As four such positions are determined, the reconstruction of the particle trajectory is possible.

Figure 3.6 shows a schematic view of such a drift chamber. Particles ionize the gas along their track. In the electric field, the released electrons move to the Frisch grid, where they are amplified and finally detected on the pads. Each chamber has 128 such pads of 5.46 mm width with inter-pad gaps of 0.54 mm. The signal measured on each pad is proportional to the number of charge carriers released above it. Therefore, the centroid of the charge distribution determines the x position in the respective chamber with a higher precision than the width of the pads. For the calculation of the centroid, the SECHS method [LP95] is used. In [Lib01], a very similar drift chamber is described, in which the pads are not individually read out. The two rows of pads of a pair of drift chambers are displaced in x direction by half their width. In beam direction, the distance between the two chambers of a pair is 51 mm.

The y position is determined from the drift time of the electrons to the anode wire. This time is measured relative to the time signal from the plastic scintillator at the end of SPEG.

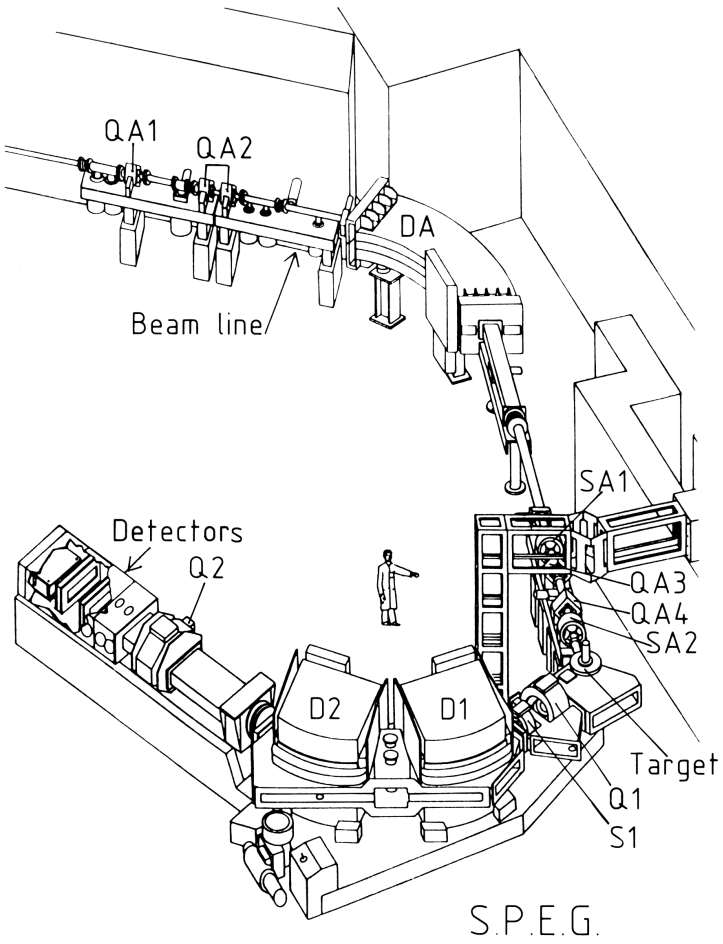

Figure 3.5.: View on SPEG [BFG+89]. The beam enters from the upper left side. Here, only the spectrometer part after the target is discussed, i.e. the drift chambers (labeled *Detectors*), the ionization chamber and the plastic scintillator.

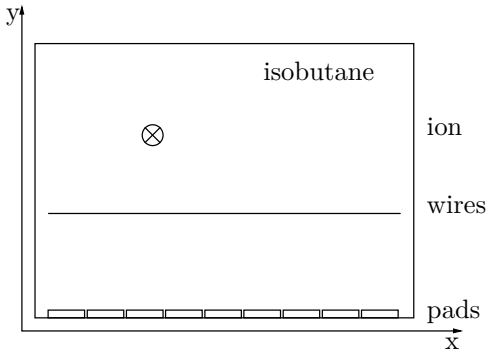

Figure 3.6.: Schematic view of a drift chamber in SPEG. Electrons released by the passing particle are accelerated in the electric field parallel to the y axis towards the wires. They are amplified by the high tension between the wires and the pads where they are finally detected.

To reconstruct the particle trajectory, the four positions are, as already stated, connected by a best fit straight line. Assuming that the scattering of the particle in the chambers is negligible, this line represents the particle trajectory. From the line, the angles θ between the trajectory and the $x-z$ plane (taking into account the tilting angle of 8 ° between focal and $x-z$ plane), and ϕ for the $y-z$ plane can be calculated. A calculation of the intersection point of the best fit line with the tilted focal plane yields the position of the particle in the focal plane. From the x position the $B\rho$ value can be calculated, and, if the charge Z of the particle is known, also the momentum can be determined.

The drift chambers are followed by an ionization chamber, which is used to identify the Z of the particles. The energy loss in the gas, which depends on Z according to the Bethe-Bloch formula, is measured in three consecutive chambers, but only the average is recorded.

Finally, the beam is stopped in a plastic scintillator. Along the beam axis, the distance between target and scintillator was 16.6 m. The scintillator is connected to two PMTs on the right and the left side. Their signal is used both for time measurements and as a trigger for the data acquisition system. One time measurement is, as explained above, against the anode signals from the drift chambers for the determination of y positions. Another time measurement is relative to the MWPC/MCP detector before the target. From this time-of-flight between target and beam stop—the short flight path to the target can be neglected—and the $B\rho$ value obtained from the x position in the focal plane, the ratio of mass to charge can be determined after the target. Together with the Z identification by the drift chambers, this allows to determine the mass A and charge Z of each outgoing particle.

As the very intense secondary beam is also scattered in the target and partially enters SPEG, a slit had to be placed in front of the focal plane for some production runs to keep the trigger rate acceptable. The presence of this slit is listed in table 3.2.

3.3. Experiment and Data Analysis

One week of beam time was available for the experiment. This time includes the setup and optimization of the beams, test runs, calibration runs and different settings for the secondary beam. Table 3.2 lists the most important runs of the experiment. The results for the nucleus ^{36}Ca, that will be presented in section 3.5, have been obtained from the production runs with a ^{37}Ca secondary beam. Between these, data were taken with a ^{36}Ca secondary beam. Some results extracted from these data will be presented in Appendix A.

The secondary beam that was finally obtained contained mainly ^{37}Ca, ^{36}K, ^{35}Ar and ^{34}Cl, and also ^{32}S, and ^{31}P.

To start with the description of the analysis, the calibration of some detectors will be explained in the following sections 3.3.1 and 3.3.2. Then the other important steps of the data analysis follow in sections 3.3.3 to 3.3.9.

Most of the analysis was done using the software described in Appendix B.

Table 3.2.: Overview of the different runs. The mass number A is given for the secondary beam component with $Z = 20$. The value $B\rho_\alpha$ after the α spectrometer remained unchanged throughout the experiment. The beam intensities ν are typical values of a frequency counter on the detector at the target position.

runs	A	$B\rho_\alpha$ (Tm)	$B\rho_{\mathrm{SPEG}}$ (Tm)	ν (kHz)	target det.	target	SPEG slit
164	37	2.093	1.655	0.165	MWPC	yes	no
166–169	37	2.093	2.093	0.150	MWPC	no	no
170–359	37	2.093	1.600	91	MWPC	yes	yes
366–400	37	2.093	1.600	85	MCP	yes	yes
427–452	36	2.093	1.579	67	MCP	yes	no
457–521	37	2.093	1.588	160	MCP	yes	yes

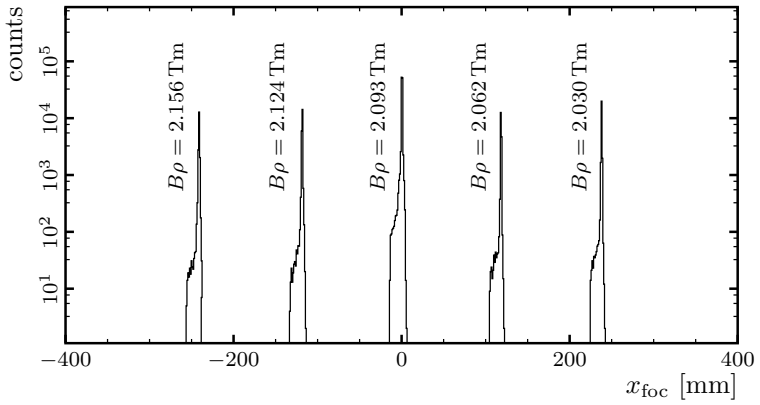

Figure 3.7.: For the $B\rho$ calibration of SPEG, the $B\rho$ setting of SPEG was varied for a fixed beam $B\rho$, and for each setting the x distribution in the focal plane was measured.

3.3.1. $B\rho$ Calibration of SPEG

At the beginning of the beam time, calibration coefficients for the measurement of $B\rho$ values with SPEG were determined in a few dedicated runs. The primary ^{40}Ca beam was guided into SPEG with reduced beam intensity. While the $B\rho$ value of the beam was kept constant, the magnetic field of the dipoles was changed, and thereby the $B\rho$ value of particles that can travel along the central axis. For each $B\rho$ setting of SPEG, the mean x position of the beam in the focal plane was determined. Figure 3.7 shows x distributions for the chosen $B\rho$ settings. From the mean x values, the relation

$$B\rho_{\mathrm{beam}} = \frac{1}{0.9998 - 1.2558 \cdot 10^{-4} \cdot x} B\rho_{\mathrm{SPEG}} \tag{3.3}$$

has been deduced for x in mm. The dimensions and placement of the pads was assumed to be as described in section 3.2.6. The given relation is also true for other $B\rho$ settings of SPEG as these are set by changing the magnetic field, but not the geometry, and the deflection depends linearly on the magnetic field. It has, therefore, been used in all following calculations of $B\rho$ values.

For an ion with charge Q, the relation

$$p = 299.792\ Q\ B\rho \tag{3.4}$$

holds for values of $B\rho$ in Tm, and momentum p in MeV/c.

From figure 3.7 also the good momentum resolution of SPEG can be estimated. The peak for $B\rho = 2.093\,\mathrm{Tm}$ has a width of around 0.85 mm FWHM, which corresponds to a momentum resolution of $dp/p < 10^{-4}$. This is largely sufficient for the purposes of this experiment.

3.3.2. Energy Calibration of the BaF_2-Detectors

To obtain precise γ-ray energies, the detectors of the Château de Cristal have to be calibrated using known transition energies. This calibration is usually done with sources placed at or near the target position. In the experiment, sources of ^{22}Na, ^{60}Co and ^{152}Eu were available. None of these emits γ rays near 3 MeV where the first 2^+ state of ^{36}Ca is expected from a comparison with its mirror nucleus. From the ^{22}Na source, e.g., γ rays of energies 511 and 1275 keV are emitted from the β^+ decay of ^{22}Na.

Therefore, the calibration of the detectors was performed in two steps. In the first step, a calibration for each individual crystal was extracted from the spectra obtained with the Na source. This source calibration was repeated several times throughout the beam time to compensate for possible shifts due to temperature changes or other effects.

In the second step, lines originating from excited nuclei produced in the secondary target during the production runs were used to make small corrections to these calibrations. As these γ rays were emitted in flight, the measured energies had to be corrected for Doppler shifts. This was done in the way described later (in sec. 3.3.8). Even for the most intense lines from the nuclei produced in-beam, it was not possible to correct the calibration of each crystal individually. Therefore, a global correction was applied for each of the four run groups listed in the last rows of table 3.2. While this type of correction does not improve the energy resolution, i.e. the width of the lines, it still reduces the error on the observed centroid. The result of the calibration procedure is shown in table 3.3 for the runs 170–359. The table shows that global corrections are rather small. The remaining deviations from the known transition energies do not exceed 8 keV.

3.3.3. Particle Identification After the Target

According to eq. (3.1), a particle's time-of-flight after the target and its $B\rho$ value determine the ratio of its mass and charge. Although the formula is simple, its practical application is not. This is due to the different flight path lengths depending on the particle's momentum and the angle θ of its trajectory against the $y - z$ plane. For example, the energy loss in the secondary target and in the drift chambers depends on the charge of the ion. Also the flight path length in the ionization chamber depends on the x position of the particle in the focal plane and its angle θ. This complicates a thorough analysis of the energy loss signal. To identify particles, it is not necessary to separately account for these dependencies. It is sufficient to 'correct' the time-of-flight and energy

Table 3.3.: Calibration of the BaF_2 detectors using a ^{22}Na source and known lines from nuclei produced in the secondary target. The known energy values E_{lit} are taken from [ENS07]. E_{source} denotes the value obtained with the ^{22}Na source, $E_{\text{in-beam}}$ the value after the global correction. The difference $\Delta = E_{\text{lit}} - E_{\text{in-beam}}$ is also given. The values given here are for the runs 170–359. For the other sets of runs, a similar quality of the calibration was achieved.

Ion	Transition	$E_{\text{lit.}}$ (keV)	E_{source} (keV)	$E_{\text{in-beam}}$ (keV)	$\lvert\Delta\rvert$ (keV)	$\lvert\Delta\rvert$ (%)
^{33}Cl	$1/2^+ \rightarrow 3/2^+$	810.52(16)	815.6(20)	807.7(22)	3	0.35
^{34}Ar[a]	$2_2^+ \rightarrow 2_1^+$	1196.6(6)	1207.3(15)	1198.2(12)	2	0.14
^{29}Si	$3/2^+ \rightarrow 1/2^+$	1273.367(12)	1278.2(6)	1269.5(6)	4	0.30
^{28}Si	$2^+ \rightarrow 0^+$	1778.969(12)	1789.7(6)	1780.1(6)	1	0.06
^{29}Si	$5/2^+ \rightarrow 1/2^+$	2028.12(6)	2039.3(15)	2028.9(18)	1	0.04
^{34}Ar[a]	$2_1^+ \rightarrow 0^+$	2090.8(3)	2094.6(12)	2085.6(12)	5	0.25
^{32}S	$2_1^+ \rightarrow 0^+$	2230.2(3)	2245.9(10)	2235.8(10)	6	0.25
^{28}Si	$4^+ \rightarrow 2^+$	2838.67(5)	2842.5(26)	2831.1(28)	8	0.27

[a]The error of the *literature* value was calculated from the errors of the level energies as no error of the γ-ray energies is given in [ENS07].

loss signals with quadratic dependences on x position and angle θ. Suitable coefficients can be obtained experimentally from correlation matrices.

Sorting the value pairs of A/Z and Z obtained this way into a matrix, separate peaks become visible which correspond to individual isotopes. An unambiguous identification of the isotopes can be achieved through the γ-ray spectra observed in coincidence with the events in some of the peaks where γ-transition energies are known. Figure 3.8a shows such an identification matrix. Besides the peaks for the different isotopes, long diagonal and vertical stripes are visible which are centered around the scattered components of the secondary beam. This background could be strongly reduced with correlation requirements.

One of these correlations was required between the energy losses measured in the ionization and drift chambers. In the latter, the energy loss of the ions is also measured quantitatively, but as this measurement is not the primary purpose of the detectors, the resolution is worse than in the ionization chamber. The energy loss value for the drift chambers was calculated as the sum of signals of the pad with the maximum charge deposit and its two neighbors, summed over all four drift chambers. Here too, the dependence on x and θ was accounted for with a quadratic 'correction'. The correlation was enforced by defining a range around the diagonal line seen in a matrix plot of the two energy loss values, and by rejecting events with signals outside this range.

A second correlation was required between the time-of-flight and the energy signal of the plastic scintillator which stops the beam. The energy deposited there corresponds to the kinetic energy of the ion, which, according to

$$T = \frac{1}{2}mv^2 \quad \Rightarrow \quad \frac{\sqrt{m}}{q} = \frac{B\rho}{\sqrt{2T}}, \tag{3.5}$$

also allows a determination of the mass-to-charge ratio. Again, a quadratic 'correction' for the x and θ dependence was applied, a range was defined experimentally in a matrix, and events not in this range were rejected.

With these correlation requirements, the particle identification matrix shown in figure 3.8b is obtained, where the vertical and diagonal stripes are strongly reduced.

Figures 3.8c and 3.8d show particle identification matrices for the runs with a MCP detector before the target. These are less clean than the matrices obtained with the MWPC (but see 3.10). All peaks have a satellite at lower A/Q values. As the A/Q value is calculated from the time-of-flight and the satellite peaks appear with the replacement of the detector, it may be assumed that they originate from an undesired signal from the MCP detector, which has, however, a time relation to the particle passage. It is very likely that these signals are produced if the MCP amplification is started by x rays, not electrons, emitted when the ion passes through the emissive foil of the detector (see figure 3.2). The x rays would reach the MCP faster, which agrees with the location of the satellite peaks in the matrix.

3.3.4. Efficiency of SPEG

For one of the calculations of the total knockout cross section (see sec. 3.5.3), the efficiency of the SPEG detector setup needs to be known. This efficiency was determined using data taken immediately before the start of the ^{36}Ca production runs (164–169, see table 3.2). In these runs, the beam intensity was small. Therefore, both the dead-time of the data acquisition system and the number of double-hits in the MWPC detector were small. Furthermore there was no slit in SPEG and the momentum distributions of the beam components were narrow enough to be in the acceptance range of SPEG.

As a first step, the live time of the data acquisition was determined. It is given by the ratio of two scalers fed by a 100 Hz pulser, one of them with and one without an anti-coincidence with the busy signal of the data acquisition system. The ratio of the two counts determines the live time ratio, which was $l = 0.94(1)$. For higher beam intensity, the dead time ratio $(1 - l)$ was larger.

Then, the number N of ions passing through the CATS detector was read from the corresponding scaler. The number n of ions detected in SPEG is the number of events triggered by the plastic scintillator, minus a few events where a trajectory line could not be fitted well. The efficiency of SPEG is then

$$\epsilon_{\mathrm{SPEG}} = \frac{n}{N}\frac{1}{l} = 0.92(1). \tag{3.6}$$

This is actually only the efficiency of SPEG relative to the MWPC detector, but this is not a problem. For the cross section calculation, the time signal of the MWPC detector is used to select the incoming beam both for the counting of ^{37}Ca and for the counting of ^{36}Ca so that its efficiency cancels out in the calculation. Furthermore, the efficiency of the detector is expected to be very close to 100 % for the present beam [OMA+99].

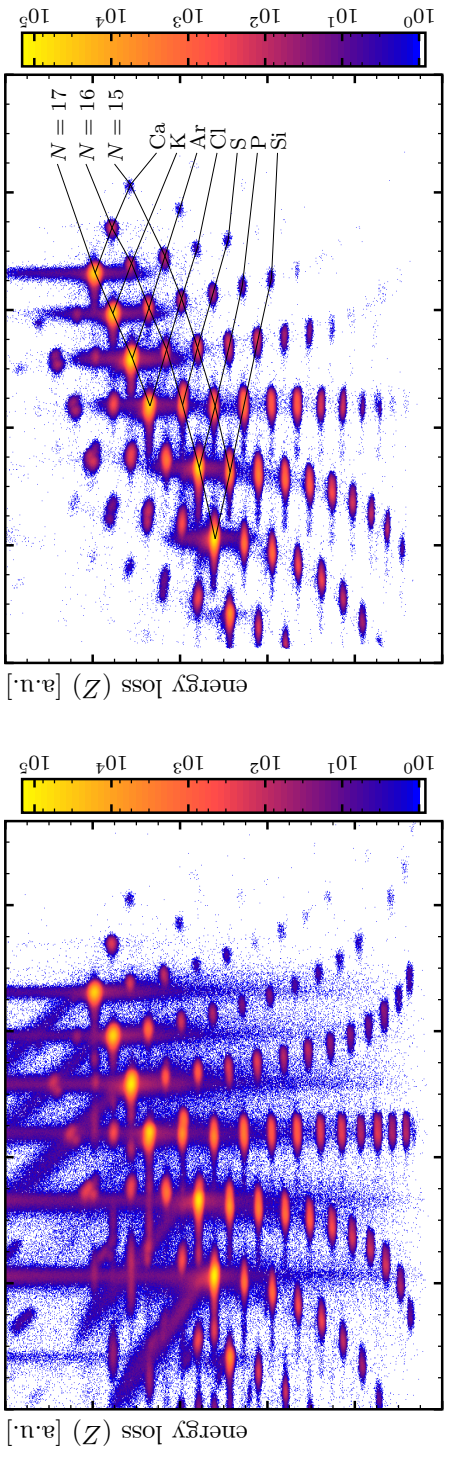

(a) Identification matrix with MWPC without correlations requirements.

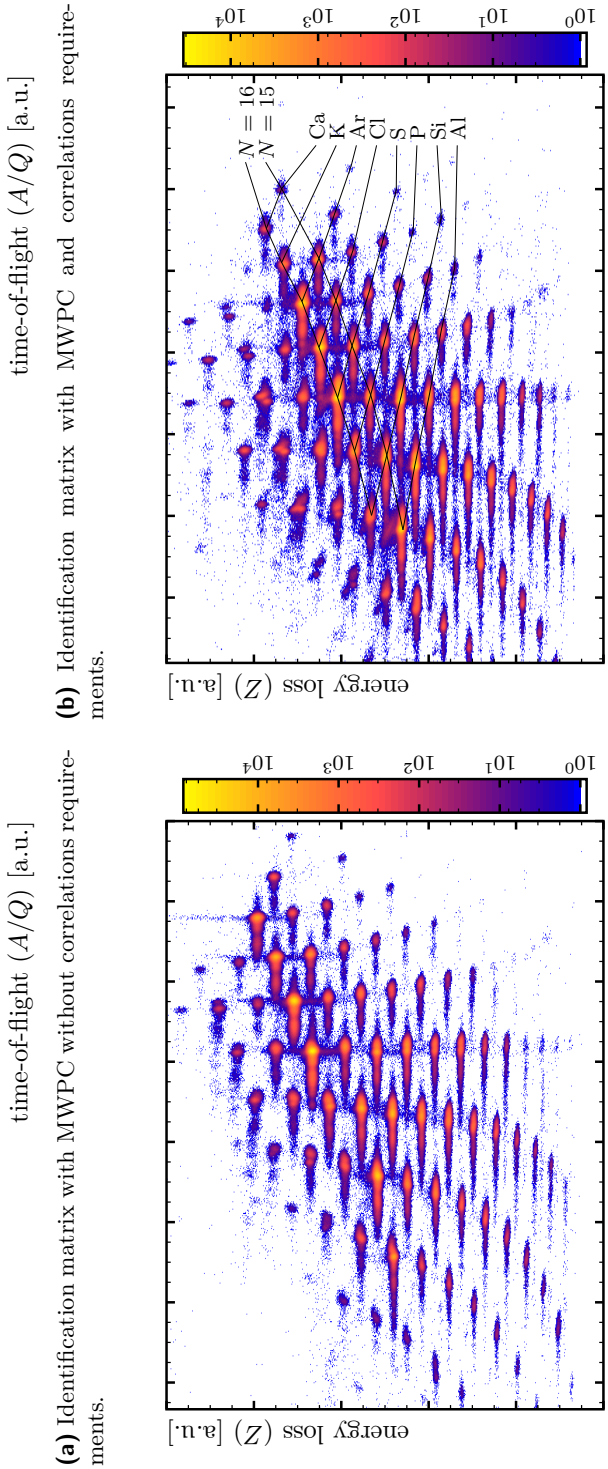

(b) Identification matrix with MWPC and correlations requirements.

(c) Identification matrix with MCP with ^{37}Ca secondary beam.

(d) Identification matrix with MCP with ^{36}Ca secondary beam.

Figure 3.8.: Matrices for particle identification after the Be target. The y axis shows the drift chamber signals, the x axis time-of-flight signals between the timing detector at the target and the beam-stopping plastic scintillator. Both are 'corrected' for momentum. Except for 3.8a, the matrices have been gated as described in the text.

3.3.5. Particle Identification Before the Target

For the identification of particles reaching the secondary target, a time-of-flight measurement was foreseen in the setup. This is sufficient to distinguish the components of the secondary beam. Unfortunately, this measurement was not successful, maybe due to problems in the electronics setup. These problems are related to the beam intensity and were not noticed until after the end of the experiment.

In the runs with the MWPC detector before the target, about 38 % of the events recorded on tape have no value from the time-of-flight measurement, indicating overflow or failure to start the measurement. A test with low beam intensity yields a one-to-one correspondence of peaks in the time-of-flight spectrum to peaks in the SPEG particle identification matrix. But almost all peaks of the matrix are visible at high intensity, even with conditions on the time-of-flight before the target that should select only one isotope of the incoming beam. This cannot fully be caused by nuclear reactions as for the light beam components, heavy nuclei are observed in SPEG, too. In addition, the percentage of, e.g., ^{37}Ca ions of the total counted in SPEG is quite different if a condition is set on the time CATS-HF (HF being the high frequency of the cyclotron) alone, or if an additional condition is set on the time CATS-Galotte. With a correct identification, this value should stay constant.

For the runs with the MCP detector in place of the MWPC, the situation is even worse. Only a few percent of the events have values from the time-of-flight measurement. And the time-of-flight spectra before the target remain almost unaffected by conditions on particular isotopes in SPEG. As this does not allow an identification of the incoming particles, the data from runs with the MCP detector have not not used for the cross section determination.

3.3.6. Double-Counting in CATS

During the production runs, the beam intensity was quite high, in the order of 100 kHz on the secondary target. Therefore, sometimes two ions were detected in the same event by CATS, and some of them can even be recognized.

Such events can be found by counting, for each event, the maxima in the charge deposit on the strips. While this method yields illustrative examples of the problem, it does not find events where two ions hit the detector at similar positions. Most of the two-particle events, with or without two distinct maxima, should have a broader distribution of the charge deposit on the strips. Figure 3.9 shows histograms of the width σ of the charge distribution for two runs, with higher and lower beam intensity. Around 5 % of the events of the high-intensity runs have $\sigma > 1$. For the evaluation of cross sections it is therefore assumed that for production runs, 5 % of the events are double hits in CATS. As this is just an estimate, a 2 % absolute error has been assumed.

3.3.7. Time Gate on the BaF_2 Detectors

In the reactions taking place in the secondary target, neutrons may be emitted with high kinetic energies. Velocities around the speed of the beam may be reached. In

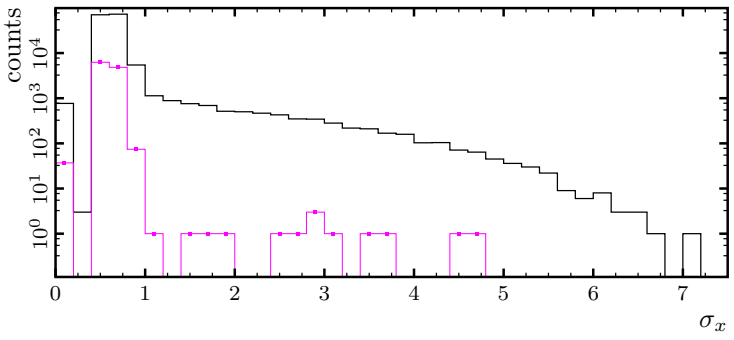

Figure 3.9.: Width (σ_x) of the horizontal charge distributions on CATS for runs with high (——) and low (—▪—) beam intensity.

contrast with charged particles, neutrons may pass through the beam tube, interact with the scintillation crystals and deposit some energy. Furthermore, reactions may be induced by these neutrons, exciting the nuclei of the crystals which then could emit γ rays themselves. To suppress such background, it is desirable to discriminate signals caused by neutrons from γ transitions in the target. This can be achieved using the time signal from the scintillators. The neutrons need more time to reach the crystals due to their lower velocity compared to photons. While γ rays have flight times in the order of 1 ns, neutrons travel for around 4 ns when emitted with a kinetic energy of 50 MeV. In the spectrum of time signals, these two can be separated, at least for some detectors. For detectors in forward direction, the neutrons are faster and consequently the time difference is smaller. Those detectors with an unclear separation of the two contributions have not been used in the further analysis. Some other detectors could not be used because of their bad resolution. In total, only 61 out of the present 74 detectors have been used in the analysis.

3.3.8. Correction for the Relativistic Doppler Shift

Gamma rays emitted from nuclei in flight have different energies in the nuclear rest frame and in the laboratory system due to the relativistic Doppler shift. The energy E_0 in the rest frame is

$$E_0 = E_{\mathrm{lab}}\gamma(1 - \beta\cos\alpha) \tag{3.7}$$

with $\beta = v/\mathrm{c}$, $\gamma^{-2} = 1 - \beta^2$, the velocity v of the nucleus at the time of emission, and the speed of light c. Here, α denotes the angle between the directions of motion of the nucleus and the γ ray. Due to the large opening angle of the BaF_2 crystals of up to 25 ° and the small angles of the beam against the beam axis, the angles of the central point of the detector against the beam axis were used as an approximation for α in the analysis.

The half-life of the first 2^+ state in ^{36}S is 75 fs [ENS07], and as a very first approximation a similar half-life can be assumed for the corresponding state in ^{36}Ca. In this time the nuclei travel approximately 7 µm or 0.7 % of the target thickness. This means that most γ-ray emissions will take place in the target. The energy loss in the target is quite large: the Ca ions are slowed down from around 60 MeV/u to around 38 MeV/u.

Therefore, the exact speed of the ion at which a γ ray was emitted is unknown. The cross section for the knockout reaction does not change very much between the energies at the beginning and the end of the target (cf. fig. 3.17). Therefore, it was assumed in the analysis that the γ-ray emission took place in the middle of the target. The energy at this point can be calculated from the energy loss in the target.

A minor improvement to this procedure was applied using the momentum measured in SPEG: using `LISE++` [TB03], the mid-target energy was calculated for ions with the central $B\rho$ of SPEG. Then, this 'central' mid-target $B\rho$ can be used in eq. (3.3) in place of $B\rho_{\mathrm{SPEG}}$ to calculate the actual $B\rho$ of the ions at mid-target and to obtain an estimate for their speed.

3.3.9. Reconstruction of γ-Ray Energies with Add-Back

At high γ-ray energies, around 3 MeV, as they can be expected in this experiment, the Compton-scattering process has a significant cross section. If a γ ray leaves the crystal after such a scattering process, the measured energy is not the energy of the photon. For a partial reconstruction of the energy of these γ rays, energy values measured in neighboring detectors were added in an *add-back* procedure: Energies measured in up to three crystals in a row, or in a triangle, were added if their time signals were in a narrow, common time window. For the Doppler correction, the emission angle of the γ ray has to be known. As most frequently the largest energy deposit is at the first interaction point of the γ ray, it has been assumed that this point lies in the crystal that measured the largest contribution to the sum.

The same procedure is also suitable to partially reconstruct the energy of γ rays which produced positron–electron–pairs. In the annihilation of the positron with an electron from the crystal, two γ rays of 511 keV are produced, one or both of which might escape from the detector crystal.

3.4. `Geant4`-Simulation of the Experiment

For the analysis of the momentum distributions, a Monte-Carlo simulation was used. It will be described in the following section. Two important parts of this analysis are based on this simulation. The first is the determination of the efficiency of the Château de Cristal. As described in section 3.1, this efficiency is needed to calculate the momentum distribution for the ground state of ^{36}Ca. The second part is the broadening of the momentum distributions in the Be target.

The simulation program was built using the `Geant4` toolkit [AAA$^+$03]. This software package is developed and has been used for many years at CERN. One example of its use for the development of γ-ray detectors is the simulation code by E. Farnea for the AGATA detector [Far07].

3.4.1. Detector and Material Geometries

The first step towards running a Geant4 simulation is to describe the geometries of materials like target, beam tube, vacuum, and detectors.

Secondary target. The secondary target was simulated as a foil held by an Aluminum frame floating in the beam tube (which is easy to realize in a simulation). This frame was quadratic with 4 cm side length, 2 mm thickness and a circular hole for the target foil. The target foil itself was of the material suitable for the simulation being run. For example, for the simulation of ^{36}Ca momentum distributions, it was a Be foil of 4 cm diameter with a thickness of 1080 µm. The thickness was chosen to reproduce the measured $B\rho$ values given in table 3.1. Apparently, the programs LISE++ and Geant4 use slightly different energy-loss tables.

Beam tube. The beam tube was modeled as a simple tube. As in the experiment, it had an outer diameter of 100 mm, and a thickness of 5 mm and was made of steel. In the simulation, 'steel' was assumed to be a mixture of 4 % carbon, 8 % cobalt and 88 % iron. The structures for the target support, the support of the beam tube itself and any other complications were omitted. A perfect vacuum was assumed inside the tube.

The CATS detector. The CATS detector was modeled to see the effects of its anode wires. The dimensions and material specifications were taken from [OMA+99]. The diameter of the tungsten anode wires was set to 18 µm. This deviation from [OMA+99] (who specify 10 µm) was made to make the simulation of the ^{37}Ca secondary beam agree with the experiment. These anode wires cover around 1 % of the surface of CATS. The beam passing through the wires is slowed down, and the slowed-down part of the secondary ^{37}Ca beam is then visible in the SPEG focal plane despite of the slit intended to suppress the secondary beam.

No gap was modeled between the Au cathode strips of the MWPC detector to better reproduce the shape of the momentum distribution of the ^{37}Ca secondary beam without target.

Secondary beam. The secondary beam parameters were adjusted to reproduce the experimental observations. The beam energy of the ^{37}Ca secondary beam before the MWPC detector was sampled from a Gaussian energy distribution centered at 60 MeV/u with $\sigma = 0.11$ MeV/u. The angular distribution was isotropic around the beam axis. The angle between beam axis and ion direction was sampled with the absolute value of a Gaussian distribution centered in z direction with $\sigma = 7.5 \times 10^{-6}$ rad. The possibility to compare simulated and experimental beam was limited by the low statistics collected in the runs without secondary target (cf. 3.2).

The Château de Cristal. The Château de Cristal was modeled as an arrangement of BaF_2 crystals. Unlike the real detector, the energy deposited in the scintillators by γ

rays, neutrons and possibly other particles was read out directly. The photomultipliers were not simulated as they are very complex devices for a Monte-Carlo simulation because many materials and particles (low-energy photons) are involved in producing a signal. The BaF_2 material was shaped hexagonally with 5 cm diameter and 14 cm length. The crystals were enclosed in 90 µm Teflon, a 10 µm air gap, and placed in Aluminum cans of 0.9 mm wall thickness. On top of the crystals, the glass and cathode materials of the photomultipliers were attached without any intermediate layer. The 74 crystals were arranged as in the experimental geometry.

The ^{22}Na source data for the energy calibration of the real Château de Cristal were used to find the energy resolution of the crystals. It was determined to be

$$\sigma = 1.52\text{keV}\sqrt{E_\gamma/\text{keV}}. \tag{3.8}$$

No timing information from the Château de Cristal was used in the simulation. Those crystals that were not used in the real analysis, were simulated to account for scattering, but then ignored in the analysis of simulated data. The same add-back procedure that was used for the experimental data (see section 3.3.9), was also applied to the simulated data.

The spectrometer SPEG. The spectrometer SPEG was not modeled at all to simplify and speed up the simulation. Instead, the $B\rho$ and angles of the beam particles were taken from the tracked particles and smeared out with Gaussian distributions to account for the detector resolution.

3.4.2. Physical Processes in the Simulation

In the `Geant4` toolkit, a simulation of many physical processes is already included. Among those are the photo effect, Compton scattering, pair production, ionization and energy loss by particles passing through matter, and many others. Only a few processes had to be modified or added for the present work.

Gamma-Ray Emission

The emission of γ rays from excited, moving nuclei is one of them. The implementation of the γ-ray emission process included in `Geant4` previously only applied to nuclei produced in radioactive decay and assumed that all transitions from cascades occur at once. Thus it did not allow for transport and energy-loss processes to apply before γ-ray emissions or between two steps of a cascade. Only the application to moving nuclei had to be added.

This emission process implementation takes into account the lifetimes (in rest frame and laboratory system) of the excited states and also the branching ratios if several γ decay paths are known. The recoil of the nucleus is accounted for, too. The angular distribution of emitted γ rays is always isotropic in the rest frame of the excited nucleus.

One-Neutron Knockout

The code for a simulation of the one-neutron knockout process was newly implemented. The present implementation includes a biasing technique (see below) to ensure that all but a few percent of the incoming beam nuclei react in the target. This is unphysical, but it is necessary to obtain simulation results in an acceptable time. For the target thickness used in the experiment, cross sections in the order of 10 mb mean that only roughly one out of ten-thousand ^{37}Ca ions nuclei makes a reaction. The cross sections for other processes are not affected by the biasing. This is most important for the processes describing the energy loss of the ions in the target.

The momentum distributions of the knockout residues have been calculated using the program `momdis` [BG06]. The correlation of parallel and perpendicular distributions have to be calculated in matrix form. The process classes added to `Geant4` use these calculated matrices to sample the momenta of the reaction products. A linear interpolation is used to calculate the momentum distribution at the actual energy of the reacting ion from the distributions calculated for a few beam particle energies. The energy dependences of the calculated cross sections are taken into account, too. (see sec. 3.6)

Biasing technique. For a very small, energy-independent cross section, the probability that a neutron knockout reaction occurs is approximately constant along the track through the target. It is assumed in the simulation that the sum of cross sections of any other isotope-changing reactions is small enough to apply the approximation of constant reaction probability. Therefore the process implementation first calculates the track length l' in the target that can be expected from the particle direction at the entrance point into the target[1]. This length is multiplied with a factor slightly above one to ensure that the length $l = l_0 = el'$ (where $e = 1.02$ was used) is longer than the actual track in the target even in the presence of scattering. Using a uniform distribution, a fraction r with $0 \leq r < 1$ is then chosen so that the particle shall travel the length rl before the process applies. As will be shown in section 3.5.2 (fig. 3.17), the cross section calculated with `momdis` for the knockout reaction varies slightly with the decreasing particle energy in the Be target. For a varying cross section, the value l is modified by scaling it with the ratio of the cross sections $\sigma(E)$ at the present particle energy E and σ_0 at the entrance point into the target at each step through the target as

$$l(E) = \frac{\sigma_0}{\sigma(E)} l_0. \tag{3.9}$$

This technique works as long as the cross section does not increase above the initial value. Otherwise e has to be enlarged to ensure that l is not exhausted before the simulated ion leaves the target[2]. The step size is limited to ensure an 'up-to-date' scaling.

[1] This avoids errors from forgetting to adapt the process implementation if the target thickness is changed and still allows to have, for any target thickness, only a few percent non-reacting particles.

[2] Such an enlargement is not implemented because it is not needed for the present simulation—figure 3.17 shows that the cross section at the beginning is largest.

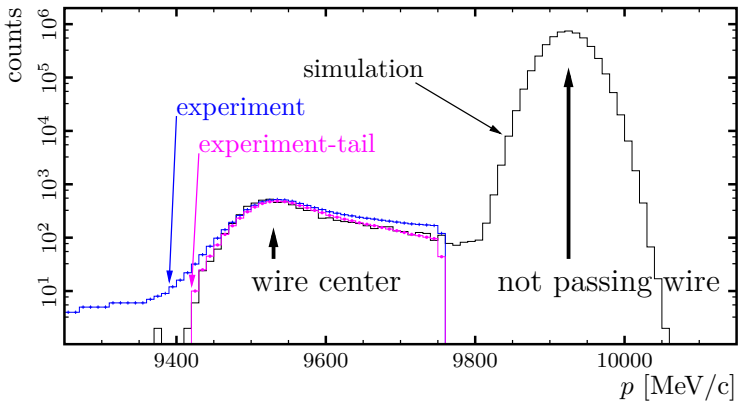

Figure 3.10.: Comparison of simulated (—) and experimental (–•–) beam slowed down in the anode wires of the CATS MWPC detector. After subtraction of the tail of the ^{37}Ca momentum distribution (as measured in the Galotte runs) from the experimental curve from the CATS runs, a good agreement to the simulation is achieved (–•–).

3.4.3. Simulation results

In this section, two results from the `Geant4` simulation shall be presented that are not directly related to a specific nucleus.

Effect of CATS Anode Wires

Good agreement is achieved for the simulated ^{37}Ca beam being slowed down in the CATS anode wires, see figure 3.10. It is apparent that the peak in the experimental $B\rho$ spectrum shown in the figure is caused by these wires. The tail of the momentum distribution of the incoming beam was not simulated because of the low statistics of the runs without secondary target.

Efficiency of the "Château de Cristal"

The efficiency of the Château de Cristal is needed for two measurements: to calculate the portion of the ^{36}Ca ions identified in SPEG that emitted a γ ray, and to calculate the ground-state momentum distribution for ^{36}Ca. In both cases, counts obtained for nuclei detected in coincidence with a γ ray have to be divided by the efficiency ϵ to calculate their actual number.

In the experiment, an efficiency measurement was made with ^{152}Eu and ^{60}Co sources. Both emit two or more γ rays in coincidence in at least one decay path. Decay schemes for these two sources are shown in figures 3.11 and D.1 (page 88). The energies of γ rays emitted by the sources do not exceed 1.4 MeV. This is far from the energy of the 2^+ state in ^{36}Ca. Therefore, some extrapolation had to be done. As in [Sta03] this extrapolation was done using a `Geant` simulation. Table 3.4 shows a comparison of

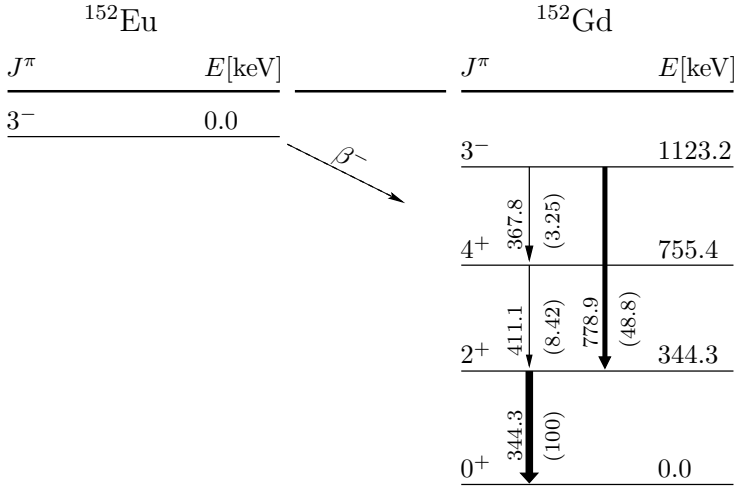

Figure 3.11.: Partial decay scheme for the β^- decay of ^{152}Eu [ENS07]. Only the transitions used for the efficiency measurement are shown. The arrows are labeled with the transition energies (left) and intensities relative to the $2^+ \rightarrow 0^+$ transition (right).

Table 3.4.: Experimental and simulated efficiencies of the Château de Cristal. All error estimates are statistical uncertainties.

	experiment			simulation		
line [keV]	$n_{\text{emit}}/10^2$	$n_{\text{detect}}/10^2$	ϵ [%]	$n_{\text{emit}}/10^2$	$n_{\text{detect}}/10^2$	ϵ [%]
			^{152}Eu			
367, 411[a]	271.2(6)	70.4(14)	25.9(5)	518	137(2)	26.4(2)
779	1134.2(24)	302.7(20)	26.7(2)	2165	563(3)	26.0(1)
			^{60}Co			
1173	22081(16)	4989(8)	22.6(<1)	2500	561(3)	22.5(1)
1332	24137(18)	5080(8)	21.0(<1)	2500	517(3)	20.7(1)

[a]These lines cannot be separated with the BaF_2 detectors.

efficiencies obtained experimentally and by simulation. The procedure to obtain these values shall be described in the following paragraphs.

For the experimental values, a coincidence measurement was used. If two γ rays, say γ_g and γ_e, are emitted in coincidence, then the efficiency of the detector system measuring $E(\gamma_e)$ is the ratio of the number of coincident detections of both rays and the total number of detections of γ_g. The low energy resolution of the Château de Cristal does not permit a clear separation of the lines from the sources. Therefore, γ_g was measured with the EXOGAM Ge detectors and γ_e with the Château de Cristal. For the ^{152}Eu source, one spectrum of BaF_2 energies was produced for events where a transition γ_g with energy 344 keV was detected in the Ge detectors. The peak integrals for the lines given in table 3.4 were calculated from this spectrum. The number of these rays γ_g was determined, too. The BaF_2 spectrum in coincidence with the background around the 344 keV line was practically empty. A very similar procedure was applied for ^{60}Co, but here the angular correlation of the two γ rays and the fact that sometimes only one γ ray with an energy of 1173 keV is emitted were taken into account, too.

In the simulation for ^{152}Eu, known relative intensities were used. These intensities are listed, normalized to the intensity of the 344 keV line, in [ENS07]. For ^{60}Co, one spectrum was made for each of the two γ rays, and the peak integrals were determined in the same way as in the analysis of the experimental spectra.

There are two important points which have to be included in the simulation to reach the agreement shown in table 3.4. One of them was to use foils of Europium and Cobalt at the target position and to emit γ rays from inside these sources. Otherwise the efficiencies were wrong by approximately 10 %. And, secondly, the threshold of the BaF_2 constant-fraction discriminators had to be emulated to obtain a similar gain in add-back for simulation and experiment.

The error estimates given in table 3.4 are statistical uncertainties. The small deviations between simulation and experiment might have many different reasons. One possible origin are simplifications in the geometry, or deviations from the specification in the actual experimental geometry. Others are limitations in the models of physical processes used in the simulation, or differences in the *read-out* of detectors. For example, the energy threshold in the constant-fraction discriminators for the BaF_2 detectors might deviate. This might introduce energy-dependent deviations as the threshold is more important for smaller energies.

As the agreement of simulated and experimental efficiency values is good, it has been assumed that an extrapolation to higher energies is possible.

3.5. Results

The focus of the experiment was on the nucleus ^{36}Ca. The cross section for the production of this nucleus in the one-neutron knockout process, the partial cross sections for the ground state and the first excited 2^+ state, and momentum distributions for these two states could be measured. These results will be presented in this section.

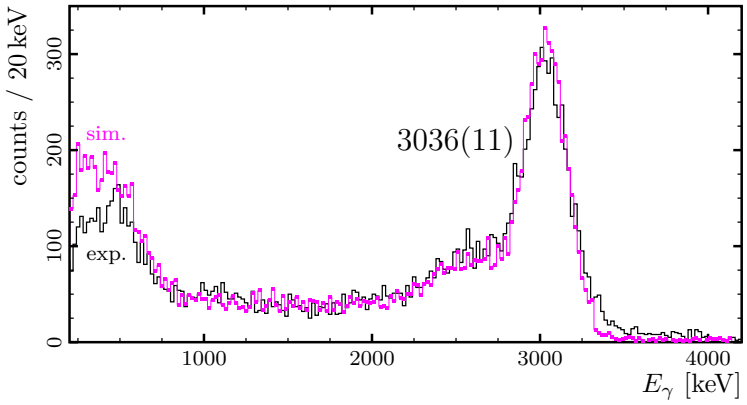

Figure 3.12.: Experimental (—) and simulated (—▪—) γ-ray spectra for ^{36}Ca. The energy of the experimentally observed transition is 3036(11) keV.

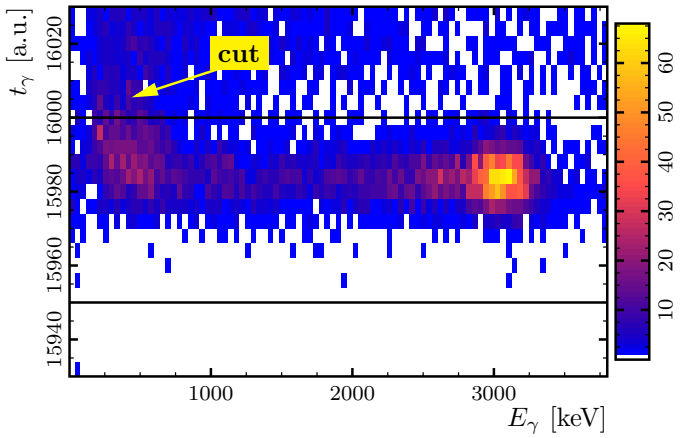

Figure 3.13.: Time-energy matrix measured in coincidence with ^{36}Ca. The only γ rays with times in the range indicated by two dashed lines are analyzed. In the low-energy region indicated by the arrow, this gate cuts the spectrum.

3.5.1. The Energy of the First 2^+ State

Figure 3.12 shows a γ-ray-energy spectrum measured in coincidence with ^{36}Ca nuclei identified in SPEG. The structure at 3 MeV originates from the de-excitation of the first 2^+ state in this nucleus. The J^π assignment is based on a comparison with the mirror nucleus, and on shell model calculations. A fit of the line with a Gaussian shape yields $E(2^+) = 3036(11)$ keV. The error for the energy is calculated from the error obtained from the fitting routine, and from the maximum deviation in the calibration (see table 3.3), added in quadrature.

Figure 3.12 also shows a simulated energy spectrum for ^{36}Ca nuclei emitting γ rays of this energy. The agreement of both is good. Only at lower energies, there is a larger deviation, i.e. the simulated spectrum contains more counts in the region around 500 keV. The origin of this deviation is assumed to be the narrow gate set on the time signals of the BaF_2 detectors (see sec. 3.3.7). Figure 3.13 shows a matrix of time signals vs. Doppler-corrected energies for ^{36}Ca. The time-gate is indicated, and it is visible that it cuts some of the low-energy values. In the simulation, no time signals were simulated, and such a cut is not applied.

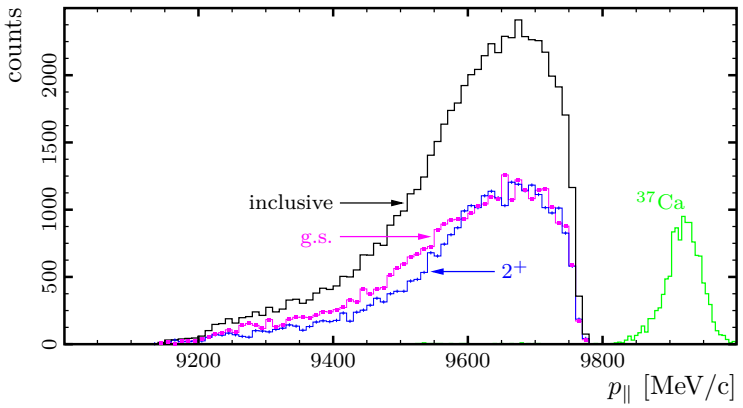

Figure 3.14.: Inclusive (—) and individual momentum distributions for the ground (—•—) and 2^+ state (—▪—) of ^{36}Ca as measured in SPEG, cut by a slit suppressing much of the secondary beam. The ^{37}Ca distribution (—) was obtained from a dedicated run without slit.

The good agreement of both spectra indicates that the experimental spectrum is dominated by γ rays of one energy. This is expected from known experimental data for the mirror nucleus, ^{36}S:

- In ^{36}S, there is a second 0^+ state at 3346 keV [ENS07] which cannot decay to the ground state by a single γ transition.
- The next highest state in ^{36}S has an energy of 4293 keV and a negative parity. This makes it unlikely to be populated by knockout, as negative parity implies that a nucleon is in the pf shell (cf. sec. 2.4.2). Furthermore, no lines which could correspond to a one- or two-step decay are seen in the spectra.
- The state in ^{36}S at 4523 keV decays directly to the ground state in 75 % of the cases. This means that a line would be expected to show up if this state was populated significantly.
- The second 2^+ state at 4575 keV excitation energy only decays via the first 2^+ state by emission of a γ ray of 1284 keV. No such line is visible in the experimental spectrum.

In summary, the assumption that the whole spectrum is originating from a single line seems justified. This is important for the following analysis of momentum distributions.

3.5.2. Momentum distributions

Figure. 3.14 shows momentum distributions for ^{36}Ca nuclei identified in SPEG, both for the ground state and for the first excited state. The procedure to obtain the two spectra is described in the following.

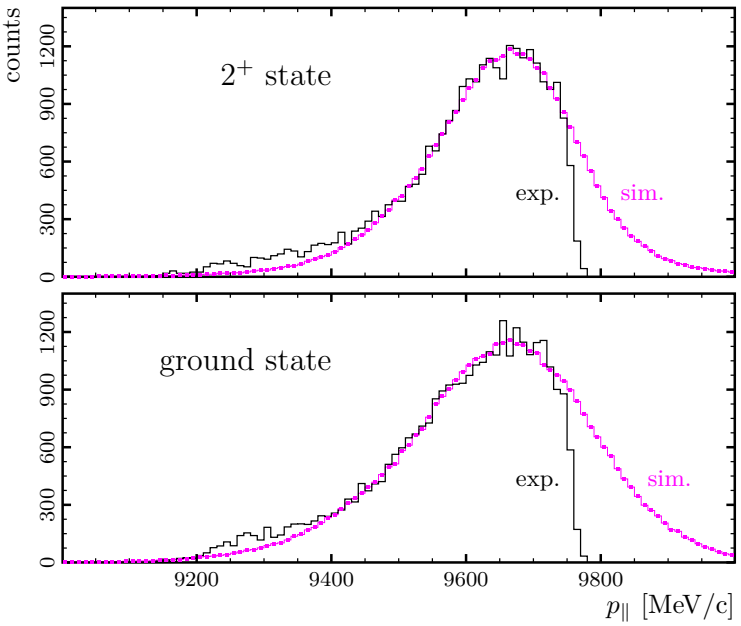

Figure 3.15.: Comparison of experimental (—) and simulated (–■–) momentum distributions after 1-neutron knockout from ^{37}Ca for the 2+ state (upper) and the ground state (lower panel), respectively. The simulated spectra are shifted by 15 MeV/c to align them with the experimental spectra, see text.

The distributions discussed here are those of the component of the momentum parallel to the beam axis. These are calculated from the momentum and the angle of the particle trajectory against the beam axis, both of which are measured in SPEG. The $p_{\|}$ distributions are best suited for the extraction of angular momenta and spectroscopic factors [BG06; HT03; TBB$^+$02].

As stated in the previous section 3.5.1, the γ-ray-energy spectrum is dominated by the decay of the 2^+ state. Furthermore, there is a rather good agreement between simulated and experimental γ-ray spectrum. Therefore, two sets of gates were chosen for the analysis to select those ^{36}Ca nuclei, which emitted a γ ray. One broad gate was set on γ-ray energies between 1200 and 3300 keV, and a narrow gate on energies between 2700 and 3300 keV. The condition for the γ-gated momentum distribution shown in figure 3.14 was that at least one γ ray be in the broader gate. The spectrum obtained with the narrow gate is in good agreement but has only about half the number of counts.

From the simulation, the number of γ rays expected in these two γ-ray energy regions can be calculated, and also ratios ϵ' with the number of emitted rays. These ratios ϵ' are 0.345 for the broad and 0.197 for the narrow gate. The measured distribution for the selected events is multiplied with $1/\epsilon'$ to obtain the momentum distribution for the excited nuclei. As only one state is assumed to be populated, the ground state momentum distribution is the difference between the one for the excited state and the total.

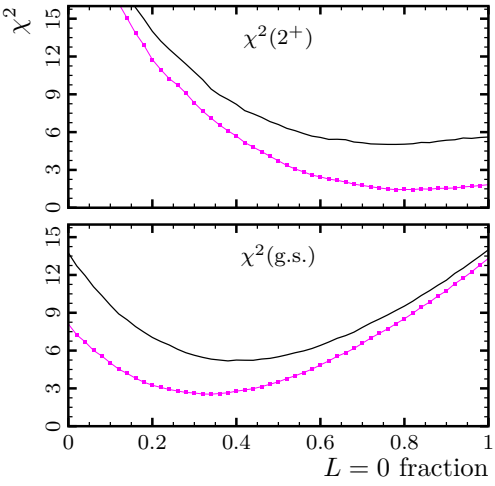

Figure 3.16.: χ^2 values for different comparisons of simulated and experimental momentum distributions, for the excited 2^+ (upper panel) and ground (lower panel) states. The χ^2 values are shown as a function of the fraction of the event number populating the state by neutron knockout from an $L = 0$ (s) state in the simulation. Curves are shown both for a gate on the photo-peak only (γ-ray energies from 2700 to 3300 keV) (—), and for a broader gate on the γ-ray energy range from 1200 to 3300 keV (—▪—).

In figure 3.15, simulated and experimental momentum distributions are compared. Unfortunately, the simulated energy loss does not agree exactly with the experimental one. Therefore, the simulated distributions had to be shifted by 15 MeV/c or $\approx 0.15\,\%$ of the momentum value.

The simulations were made for different fractions of the cross section originating from an $L = 0$ knockout, both for the ground and the excited 2^+ state. Binned spectra were then produced from the simulation data for the ground and the excited state in the same way as the experimental spectra, i.e. the simulated momentum spectra for the two different γ-ray energy ranges were scaled, and the ground state spectra were obtained by subtraction. Figure 3.16 shows the χ^2 values of fits of the simulated to the experimental momentum distribution spectra. Only bins for momenta between 9500 and 9740 MeV/c were used for the fit. Higher momenta are cut by the slit in SPEG. Lower momenta were ignored as in other experiments deviations from the eikonal theory have been observed for low momenta which are not completely understood (cf. [TBB+02; GBB+05]). In order to reduce the statistical errors of the simulated spectrum, around 30 times more particles were simulated than had been detected in the experiment. The only fitting parameter was the scale of the distribution. For each of the points shown in figure 3.16, a χ^2 value was calculated for the difference between simulated and experimental spectra, and the simulated spectra shown in figure 3.14 are those for minimal χ^2. The minimum values χ^2_0 of the χ^2 curves were then searched. It was assumed that the real minimum lies between the two $L = 0$ fraction values with $\chi^2 = 1.2\chi^2_0$, and that the best fit is the mean value of the two limits.

From the spectra gated on the broad γ-ray energy range, the optimal $L = 0$ (s) component for the simulated events was found to be 0.34(20) for the ground state, and 0.84(16) for the excited 2^+ state (see table 3.8).

The spectra gated only on the photo-peak, between the γ-ray energies 2700 and 3300 keV, contain only half the number of counts compared to the broader gate. This is reflected in the higher χ^2 for the fits (fig. 3.16). In the same way as for the broad

gate, the best fits were found to be 0.42(30) for the ground state, and 0.77(26) for the excited 2^+ state. These values are compatible with those noted above for the broader γ-ray energy gate.

The error values for the $L = 0$ components were determined from the width of the χ^2 range between the two $L = 0$ fraction values with $\chi^2 = 1.2\chi^2_0$. The uncertainties due to the choice of the fit range were estimated as 12 and 8 % for the narrow and broad γ-ray gates, respectively, in the case of the 2^+ state. For the ground state, this error plus the uncertainty due to the subtraction of the scaled excited-state spectrum were assumed to be 16 and 24 %. These errors were added in quadrature.

From the ratio of the scaling factors obtained with the χ^2 minimizations for the higher statistics, the branching ratio and consequently (looking ahead into section 3.5.3) the partial cross sections for feeding the 2^+ state and the ground state were calculated. By multiplication with the s fraction values, the four partial cross sections for the knockout from $2s_{1/2}$ and $1d_{3/2}$ can be obtained.

The standard method used in other experiments (e.g., [GBB+04a]) to make experimental and calculated momentum distributions comparable is to fold the calculated distribution with the experimental momentum distribution of the secondary beam. In this work, the interaction of the beam particles with the target is simulated using the `Geant4` toolkit. The most important difference of the two approaches is that the different energy losses of ^{36}Ca and ^{37}Ca in the target are only taken into account in the latter method. Using the method of [GBB+04a], it is not possible to explain the width of the ground state distribution measured in this experiment. The distribution of the secondary beam folded with the calculated distribution for pure $L = 2$ is too narrow. It is not surprising that this effect is not observed or much less prominent in [GBB+04a]. In their experiment, the beam energy is higher, which reduces the difference in energy loss between beam and reaction products.

As the energy-loss difference between the calcium isotopes is found to be important in our case, the energy dependence of the cross sections was taken into account, too. Here, only the dependence calculated with `momdis` is available. To account for this dependence, `momdis` calculations were performed for seven laboratory beam energies between 65 and 35 MeV/u and a linear interpolation technique was used to obtain values for particle energies between these points. Figure 3.17 shows the calculated cross sections as a function of the particle energy. Although the deviation from a constant cross section is small, the energy-dependence was included in the simulation because it might affect the width of the momentum distribution slightly. The importance of the different energy losses of ^{37}Ca and ^{36}Ca depends on the location of the reactions in the target. If the reactions were concentrated in a small region of the target (e.g., at the beginning), the broadening would be smaller as more particles would behave in a similar way.

3.5.3. Total Cross Section for the One-Neutron Knockout from ^{37}Ca

Two methods have been used to calculate the total knockout cross section to eliminate doubts about the calculated value. To determine the cross section for the one-neutron knockout from ^{37}Ca, both the number of incoming ^{37}Ca ions and the number of outgoing

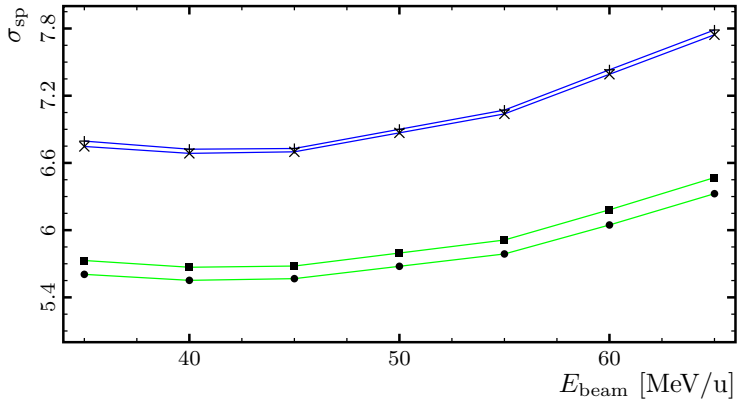

Figure 3.17.: Energy-dependence of the knockout cross section as calculated by momdis for the ground state with $L = 0$ (+) and $L = 2$ ( ), and for the excited 2^+ state with $L = 0$ (×) and $L = 2$ ( ).

^{36}Ca ions have to be determined. The two methods differ in the way the ions are counted.

Standard Method

The two time measurement points foreseen in the setup for the identification of incoming ions (see sections 3.2.3 and 3.3.5) were a Galotte detector after the α spectrometer, and a CATS detector just before the secondary target. Using these, three time measurements were set up: between the two detectors, and between each of them and the high frequency of the cyclotron CSS2. As explained in section 3.3.5, the malfunctioning of these measurements was not noticed until after the experiment.

For two conditions, the ratio of ^{37}Ca ions identified in SPEG to the number of counts in the time-of-flight peaks was determined.

- If a condition is set on the time between the CATS detector and the cyclotron high frequency around the peak that remains strongest when gating on ^{37}Ca in SPEG and looking back, about 54 % of the ions arriving in SPEG are identified as ^{37}Ca.

- If a double-condition is set, one as above, and a second on the time between CATS and the Galotte after the α spectrometer, the percentage of ^{37}Ca ions rises to about 83 % (see sec. 3.3.5 for a possible explanation for this change).

The cross section was calculated for both incoming beam selections. The incoming particles were counted using the scaled-down trigger from the CATS detector (see section 3.2.3).

The determination of the number of ^{36}Ca ions has made some difficulties, too. Here, the reason is the slit that had been introduced in SPEG to keep the scattered ^{37}Ca secondary beam from reaching the plastic scintillator. This slit also kept many of the ^{36}Ca ions away from the SPEG detectors (see fig. 3.14). To extrapolate beyond the slit, the results of the Monte-Carlo simulation were used: For all runs together, including those with Galotte, the loss ratio due to the slit was determined for the ground state and for the 2^+ state by comparing the number of counts in the best-fit simulated spectrum

Table 3.5.: Cross sections for the one-neutron knockout from ^{37}Ca calculated with different conditions and methods. The numbers of ^{37}Ca and ^{36}Ca ions are denoted by N_{37} and N_{36}, respectively.

Method	N_{37}	N_{36}	σ (mb)
CATS-HF, scaler	1.9×10^8	12350	5.4(4)
CATS-HF & CATS-Galotte, scaler	7.7×10^7	5040	5.4(4)
SPEG identification, intensity scaling[a]	4270	0.35	5.8(5)
weighted mean			5.6(4)

[a]The ion numbers are given in units of 10^{-5} incoming ions, i.e. for the Ca ion number n and total ion number N, the value $10^5 n/N$ is listed in the table.

to the corresponding experimental spectrum. Then the ion counts for the CATS runs were multiplied by the loss ratios obtained for the individual states.

As only the ^{36}Ca ions are counted with SPEG, the efficiency of the SPEG detectors has to be considered. It was assumed to be 92(1) % (see section 3.3.4). The resulting cross section values are listed at the top of table 3.5. With both conditions on the incoming beam, a cross section of 5.4(4) mb is obtained. The error values are estimates based on the statistical errors, the errors for the SPEG efficiency, and an assumed uncertainty on the target thickness of 5 %.

Alternative method

To verify the obtained value, a second method was used to determine the reaction cross section.

At the beginning of the experiment, just before the start of the production runs, the ^{37}Ca beam was guided into SPEG without the additional slit and with $B\rho_{\mathrm{SPEG}}$ set to the magnetic rigidity of the beam (see table 3.2, runs 164–169). One such run of 6 min duration was recorded with the secondary Be target (run 164), and another one of 2 min duration without the Be foil (run 166). Assuming that only the intensity, but not the composition of this beam was changed until the first few production runs, the ion rates can be used to calculate the cross section. The beam intensity was determined using a particle counter triggered by the CATS detector at the target position, and the ion counts are simply the numbers of ions of ^{37,36}Ca identified in SPEG. Again, for ^{36}Ca an extrapolation beyond the slit was made using the simulation. But, due to the minuscule number of ions, no γ-coincidence condition was set to obtain ground-state and excited-state spectra to scale them separately. Instead, the ion number was scaled by the average of both scaling factors calculated from the measured branching ratio.

As explained in section 3.3.6, about 5(2) % of the events are assumed to be double hits. While this cancels out in the calculation using the first counting method, it must be considered here as the beam intensity is very different between the runs used for

counting ^{37}Ca—about 150 Hz—and the ^{36}Ca production runs—about 95 000 Hz. This was done by assuming that the ion count read from the particle counter was correct for the ^{37}Ca runs (with lower intensity), but 5(2) % too low for the ^{36}Ca runs (with higher intensity).

The resulting cross section of 5.8(5) mb is listed in table 3.5. The given error estimate is based on the statistical errors, the imprecision estimate for the CATS double-hit rate, an estimated 5 % uncertainty on the beam composition continuity, and an assumed inaccuracy of the target thickness of 5 %.

Conclusion

The values obtained by the two methods are in agreement. The mean cross section value is $\sigma = 5.6(4)$ mb. The errors of the two methods are not independent as both calculations share, e.g., the contribution from the uncertainty of the target thickness. Therefore, the error from the first method has been used as the error estimate for the mean value. The thickness of the Be target was assumed to be 198(10) mg/cm^2 for all calculations.

3.6. Discussion

In this section, the experimental results presented in the previous section shall be compared to theoretical expectations. In the first subsection, the measured excitation energy of the first 2^+ state is discussed. The remaining subsections concentrate on the results obtained from the momentum distributions. First, some calculations will be presented, which will then be compared to the experimental results.

3.6.1. Excitation Energy of the 2^+ State

The energy of the first 2^+ state was found to be 3036(11) keV (sec. 3.5.1). In a simultaneous experiment at GSI, a value of 3015(16) keV was measured [DGR$^+$07]. Both values are in agreement within experimental uncertainties.

Compared to the mirror nucleus, ^{36}S, the energy is lower by 255(11) keV (with the energy value from this work). Besides the pair ^{14}O–^{14}C with $|T_z| = 1$, this is the largest mirror energy difference for first 2^+ states measured so far, and the largest for a pair of nuclei with $|T_z| = 2$. In figure 3.18, mirror nucleus energy differences are shown for all known $|T_z| = 2$ pairs.

Using the standard interaction for *sd* shell nuclei, USD [Wil84], the same excitation energies will be calculated for the mirror nuclei ^{36}Ca and ^{36}S as no distinction is made between protons and neutrons in the specification of this interaction. As described in [DGR$^+$07], the USD interaction can be modified to make this distinction and thus to allow for a calculation of mirror energy differences. Besides some modifications to matrix elements, the main changes to obtain 'USDm' are in the single-particle energies (SPE), i.e. the energy levels of the $d_{5/2}$, $s_{1/2}$ and $d_{3/2}$ sub-shells. In [DGR$^+$07], these energies are taken from excited states of the mirror nuclei ^{17}O and ^{17}F. Both have one

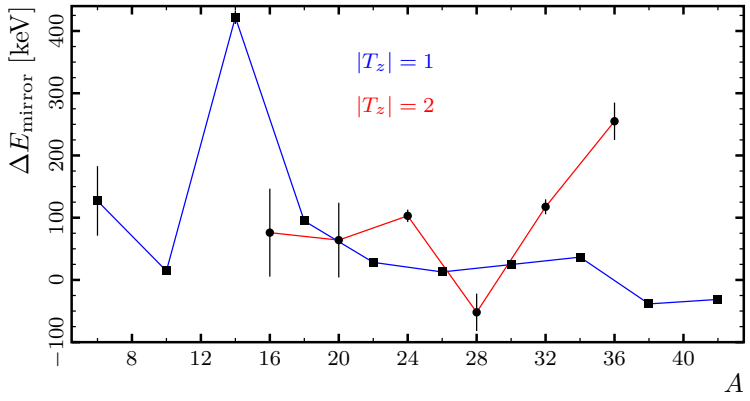

Figure 3.18.: Mirror energy differences for $|T_z| = 1$ (■) and $|T_z| = 2$ (●) mirror pairs [ENS07; YOG+06; KGM+02]. The value for $A = 36$ has been determined in this work, and the values for $A = 28$ and 32 have been confirmed (see Appendix A).

nucleon, one neutron and one proton, respectively, outside the ^{16}O core used for the *sd* shell calculations. Using the energies of the first excited $1/2^+$ and $5/2^+$ states of these $|T_z| = 1/2$ mirror nuclei as SPE, the energies for the 2^+ states in ^{36}Ca and ^{36}S are calculated as 3291 and 3558 keV, respectively. While the absolute energies are too high by about 260 keV, the energy difference of 267 keV agrees well with the experimental result. On the other hand, the mirror energy difference is not reproduced for the mirror pair ^{32}Ar and ^{32}Si. An *ad hoc* modification of these SPE is suggested in [DGR+07] to cure the problem for the $A = 32$ mirror pair. The energies of the 2^+ states in the $A = 36$ pair are not affected by the second modification which will be called 'USDm^2' here. Even with these modifications, the mirror energy difference in the pair ^{37}Ca–^{37}Cl is not well described (see sec. A.1)

A qualitative understanding of the mirror energy can be obtained from the observation that the shell model calculation yields rather pure configurations both for the ground and the excited states in both $A = 36$ mirror nuclei (cf. table 3.7). While the ground state is predicted to have mainly two neutrons in the $s_{1/2}$ shell, the excited state is dominated by a configuration with one neutron in both the $s_{1/2}$ and $d_{3/2}$ shells. Thus the difference of the dominant configurations is that one neutron is promoted from the $s_{1/2}$ to the $d_{3/2}$ shell. In the mirror nucleus, ^{36}S, the same picture holds for protons which are affected by the Coulomb potential. At least part of the mirror energy difference can then be explained as a consequence of the different spatial distributions of protons in the $s_{1/2}$ and $d_{3/2}$ shells. Hartree-Fock calculations yield a difference in Coulomb energy between these two shells of 40 to 150 keV for Sly4 and SkI5 interactions, respectively [Gra07].

3.6.2. Shell Occupancies

In this section, the calculations and results regarding the momentum distributions shall be discussed.

Table 3.6.: Parameters V_0 and r_0 for the calculation of momentum distributions. The resulting energy $-E = S_n + E_x$ and core-neutron separation r_{rms} are given, too.

State	nlj	$-V_0$ [MeV]	r_0 [fm]	$-E$ [MeV]	r_{rms} [fm]
g.s.	$2s_{1/2}$	62.6	3.66	14.8	3.36
	$1d_{3/2}$	59.1	3.88	17.8	3.36
2^+	$2s_{1/2}$	61.5	3.95	14.8	3.36
	$1d_{3/2}$	60.6	4.02	17.8	3.36

Calculations with `momdis`

An important part of this work is based on the calculation of momentum distributions with the computer code `momdis` [BG06]. The parameters for these calculations were chosen according to Refs. [BG06; GJB+06; HT03]. The radius of the ^{36}Ca nucleus was calculated with a Hartree-Fock method as $r_{\mathrm{HF}} = 3.312\,\mathrm{fm}$ [Kha07]. The radius r_0 and the potential depth V_0 for `momdis` were then adjusted for each shell ($2s_{1/2}$ and $1d_{3/2}$) and state (ground state and 2^+ state) such that the energy calculated by `momdis` agreed with $S_n + E_x$ (neutron separation energy plus excitation energy), and the radius with

$$r_{\mathrm{rms}} = \left(\frac{A}{A-1}\right)^{1/2} r_{\mathrm{HF}}. \tag{3.10}$$

The spin-orbit parameters were chosen as $V_{\mathrm{SO}} = -7\,\mathrm{MeV}$ for the strength and $r_{\mathrm{SO}} = A^{1/3}\mathrm{fm} = 3.3\,\mathrm{fm}$ for the radius. The matter distribution of the core (^{36}Ca) was assumed to be Gaussian with a radius r_{HF}. The numeric values of the parameters are summarized in table 3.6.

For the Monte-Carlo simulation, calculations were made for different laboratory energies (see fig. 3.17). For the calculation of experimental spectroscopic factors, the mid-target cross sections calculated for 50 MeV/u laboratory energy were used (cf. [GBB+04a]). These are included in table 3.8.

Theoretical Spectroscopic Factors and Shell Occupancies

Theoretical spectroscopic factors were calculated using the shell-model code `antoine` [Cau04; CN99]. For these calculations, the USD interaction [Wil84] was used. The calculated spectroscopic factors are not changed significantly using the modifications described in the discussion of the excitation energy of the 2^+ state (sec. 3.6.1), or using the recent USDB interaction [BR06]. The USD interaction includes the shells $2d_{5/2}$, $1s_{1/2}$, and $2d_{3/2}$ for neutrons and protons. Therefore, the proton shells are always completely filled for the calcium isotopes in calculations using this interaction. Both shell occupancies and the corresponding spectroscopic factors for the knockout reaction were calculated. The shell occupancies are listed in table 3.7, and the spectroscopic factors are included in table 3.8.

Table 3.7.: Shell occupancies calculated with the shell model code `antoine` [Cau04; CN99] for the nuclei ^{37}Ca and ^{36}Ca with the USD interaction [Wil84]. The column 'fraction' lists the contribution of the configuration that is specified in the remaining columns to the given state. The configurations are specified by the occupation numbers of the individual shells. Very small contributions are neglected.

A	state	fraction	neutrons			protons		
		(%)	$d_{5/2}$	$s_{1/2}$	$d_{3/2}$	$d_{5/2}$	$s_{1/2}$	$d_{3/2}$
37	g.s.	93.3	6	2	1	6	2	4
		1.3	6	1	2	6	2	4
		1.5	6	0	3	6	2	4
		3.2	4	2	3	6	2	4
36	g.s.	88.4	6	2	0	6	2	4
		5.0	6	0	2	6	2	4
		6.0	4	2	2	6	2	4
	2^+	87.6	6	1	1	6	2	4
		3.1	6	0	2	6	2	4
		5.3	5	1	2	6	2	4
		2.3	4	1	3	6	2	4

Comparison with Experiment

In table 3.8, the experimental cross sections and spectroscopic factors are summarized and compared with the theoretical values.

It must be kept in mind that the analysis depends on the calculations with `momdis` via the `Geant4` simulation. Therefore, modifications of the knockout model might also affect the experimental cross section values and the contributions extracted for the individual L values.

The best agreement is seen for the branching ratios: while the theoretical branching ratios for the ground and the excited state are 41 and 59 %, respectively, the experimental values are 57(10) and 43(10) %. Thus, the measured branching ratio, where the population of the ground state is slightly favored, is not in agreement with the calculated one which favors the excited state, although the difference is small (see below).

The theoretical cross sections are calculated [GBB$^+$04a; GBB$^+$04b] as

$$\sigma_{\text{theo}} = \sigma_{\text{sp}} C^2 S_{\text{theo}} \left(\frac{A}{A-1} \right)^2 . \tag{3.11}$$

The A-dependent factor is a center-of-mass correction valid for the *sd* shell [DF74; GBB$^+$04a]. As shown in table 3.8, the experimental cross sections are much smaller than the calculated ones.

The experimental and theoretical spectroscopic factors disagree quite much. The

Table 3.8.: Cross sections σ_{exp} and spectroscopic factors [C^2S (exp)] for the one-neutron knockout from ^{37}Ca. The cross section contributions of the two states is given in column 'BR' in percent. The fraction r is the contribution with angular momentum L to the partial cross section for each state, calculated separately for the ground and the 2^+ state, and for each of the two values, $L = 0$ ($s_{1/2}$)and $L = 2$ ($d_{3/2}$). The columns σ_{sp} and σ_{theo} show calculated single-particle- and expected cross sections, where the latter is the product of the former with the theoretical spectroscopic factors listed in column C^2S (theo). The reduction factors R_s are the ratios of experimental and theoretical spectroscopic factors.

State	BR (%)	σ_{exp} (mb)	nlj	r	σ_{sp} (mb)	C^2S exp	C^2S theo	R_s	σ_{theo} (mb)
g.s.	57(10)	3.2(7)	$2s_{1/2}$	0.34(20)	6.90	0.16(10)			
			$1d_{3/2}$	0.66(20)	5.80	0.36(13)	0.92	0.37(14)	5.64
2^+	43(10)	2.4(6)	$2s_{1/2}$	0.84(16)	6.87	0.29(10)	1.13	0.24(8)	8.20
			$1d_{3/2}$	0.16(16)	5.68	0.07(7)			

experimental spectroscopic factors, calculated as

$$C^2S_{\mathrm{exp}} = \frac{\sigma_{\mathrm{exp}}}{\sigma_{\mathrm{sp}}}, \tag{3.12}$$

are only 37(14) and 24(8) % of the calculated value for the ground and the excited state, respectively (cf. table 3.8). This is, at least in part, a consequence of the mismatch between the cross sections, which are included in the calculation of spectroscopic factors.

It has been observed in other experiments (see, e.g., [GBB$^+$04a; GBB$^+$04b]), that the calculated cross sections are systematically larger than the measured ones. The reduction factor R_s is defined in [BHST02] as the ratio of the experimental to the theoretical cross sections (or, equivalent, the ratio of spectroscopic factors). While in [BHST02] the sum of cross sections is limited to states below proton and neutron thresholds, the definition used in [GBB$^+$04a] sums all final states. Adhering to the latter, a value of $R_s = 0.40(3)$ is obtained for ^{36}Ca. For increasing S_n the quenching factor R_s decreases, as shown in figure 3.19. It is not yet clear how the R_s values can be understood, in particular their dependence on the nucleon separation energies [GBB$^+$04b]. While figure 3.19 indicates a systematic behavior, a compilation of cross section ratios R'_s for individual excited states as shown in figure 3.20 shows that there are quite large fluctuations in the R_s as a function of the effective nucleon separation energy. Together with the often large uncertainties, a systematic behavior cannot readily be recognized.

Despite the difficulties with the cross sections, the observed contributions of $L = 0$ and $L = 2$ are in quite good agreement with the spectroscopic factors calculated within the shell model. Both in theory and experiment, the ground state is mostly populated by knockout of a neutron from $1d_{3/2}$ with $L = 2$, and the excited state by knockout from $2s_{1/2}$ with $L = 0$. This indicates that the structure of the states is dominated by single

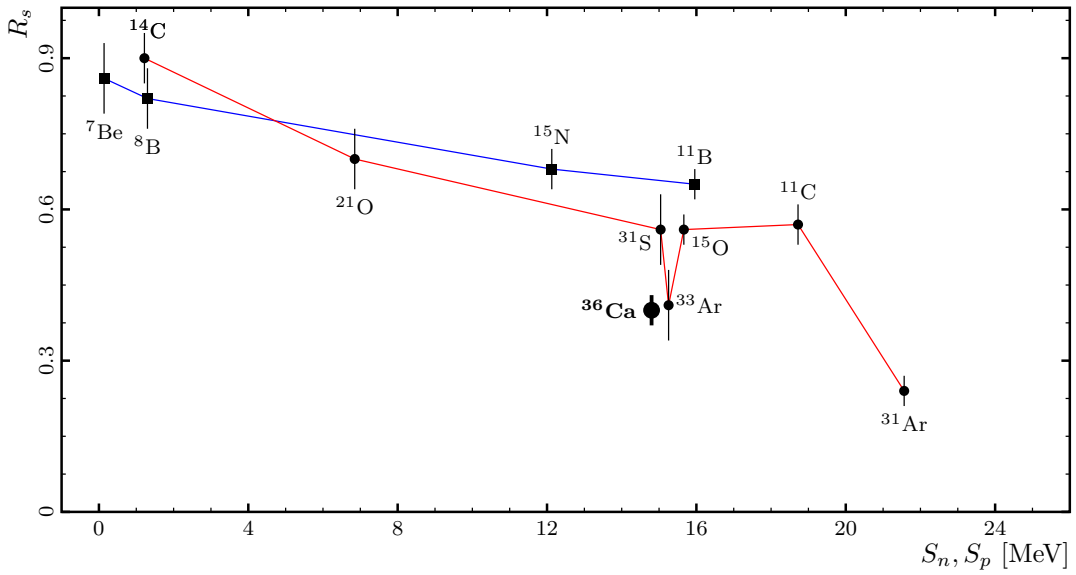

Figure 3.19.: Empirical quenching factors R_s as function of the nucleon binding energy for various nuclei [GBB$^+$04b; BHST02; TBB$^+$04; EBB$^+$03; SCO$^+$00]. Two curves are shown for proton (—■—) and neutron (—●—) knockout (cf. [GBB$^+$04b, fig. 3]). The value obtained in this work is marked with a larger symbol.

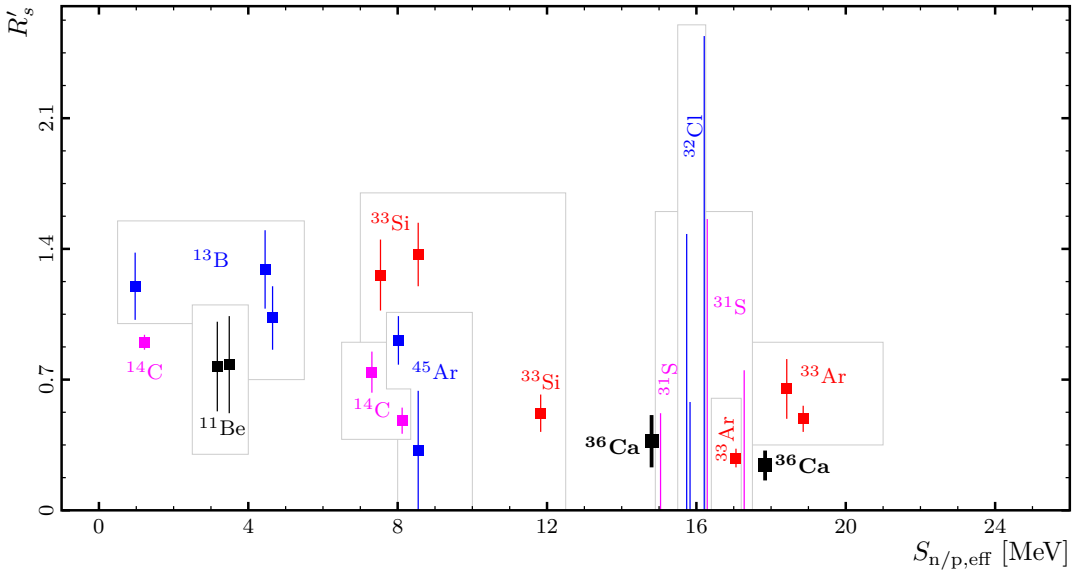

Figure 3.20.: Reduction factors R'_s as function of the effective nucleon binding energies for individual excited states in various nuclei [NAA$^+$00; GBB$^+$04a; TBB$^+$04; GKB$^+$00; EBB$^+$02; GBB$^+$05]. Error bars and fluctuations are large and hamper the interpretation as a systematic behavior. For ^{31}S and ^{32}Cl only upper limits of the cross sections are known.

configurations, as predicted by the shell model calculations for the large $N = 16$ shell gap.

Proton Emission

As the excitation energy of the 2^+ state is above the proton separation energy $S_p = 2560\,\text{keV}$ [AWT03], the state might also decay by proton emission if a configuration involving proton excitations is contributing. Calculations with `antoine` using the *sdpf* interaction and permitting up to two particles in the *pf* shell show that around 7 % of the configurations building the 2^+ state include such proton excitations. The *sdpf* interaction was designed to include neutron excitations into the *pf* shell for heavier *sd* nuclei. Therefore, the calculated value might only be an indication that such contributions are present despite the $Z = 20$ shell gap.

The experimental setup does not allow to recognize decays of ^{36}Ca by proton emission. Any ^{36}Ca nucleus populated in the 2^+ state which decayed by proton emission will therefore not be counted in the cross section calculation as it is no longer identified as ^{36}Ca in SPEG. As a consequence, the cross sections determined here have to be regarded as lower limits. While the cross section to the ground state should not be affected, the cross section from the 2^+ state would be changed, and therefore also the total cross section would be different. The presence of proton emission would furthermore be relevant for the branching ratio to the ground and excited states. As proton emissions are unobserved here, the branching to the 2^+ state could be larger, thus changing towards the theoretical value.

3.7. Conclusions

In the experiment at GANIL, the energy of the first excited 2^+ state of the exotic nucleus ^{36}Ca could be determined as 3036(11) keV. The energy difference to the mirror nucleus, ^{36}S, of 255(11) keV can be explained with *ad hoc* modifications to the USD interaction as described in [DGR+07]. A more sophisticated analysis of these mirror energy differences is left for the future.

From the measured momentum distributions, partial cross sections for the one-neutron knockout reaction from ^{37}Ca were extracted, together with the individual contributions for knockout from $L = 0$ and $L = 2$ using a Monte-Carlo simulation. The observed cross sections are much smaller than the expected ones, a fact which is also observed in other knockout experiments but remains to be explained. The observed contributions from $L = 0$ and $L = 2$ are in qualitative agreement with the expectation from spectroscopic factors calculated within the shell model, whereas the experimental spectroscopic factors deviate from the prediction. The difficulties in the cross section calculation prohibit an interpretation of these deviations as differences between the predicted and experimentally observed shell structure.

4. Confirmation of the $N = 32$ Shell Closure in Cr Isotopes

When going away from the valley of stability in the nuclear chart, the gaps between shells change, and new large gaps may appear or known ones vanish. The experiment described here focuses on the appearance of the new shell gap above neutron number $N = 32$ for nuclei of $_{20}$Ca and above. A gap at $N = 34$ has been predicted theoretically by Otsuka *et al.* [HOBM04; OUF$^+$02]. Experimental indications for the existence of an enlarged shell gap at $N = 32$ in $_{24}$Cr isotopes were known before the experiment from 2_1^+ excitation energies [PMB$^+$01]. The purpose of the experiment is thus to confirm these observations by a measurement of $B(E2; 2^+ \rightarrow 0^+)$ values for ^{56,58}Cr. A relatively low $B(E2)$ value compared to the even-N Cr neighbors would be expected in $^{56}_{24}\mathrm{Cr}_{32}$ if a large shell gap exists.

After a short introduction in sections 4.1 and 4.2, a detailed description of the experimental setup in section 4.3, the data analysis will be explained in section 4.4. After a presentation of the results in section 4.5, the chapter will finish with a discussion and references to more recent experiments in section 4.6.

4.1. Previous Information

Before the present measurement, experimental indications for a sub-shell closure at $N = 32$ were based solely on measurements of excitation energies.

An increase in excitation energy of the first 2^+ state from ^{50}Ca to ^{52}Ca was a first hint for a possibly enlarged $N = 32$ gap [HKK$^+$85]. Due to a lack of data for ^{54}Ca, on the other hand, it was (and, in fact, is) not possible to see if this energy value is a local maximum.

More recent indications for an $N = 32$ sub-shell closure came from measurements of the excitation energies of the first 2^+ states in the isotopes ^{52,54,56}Ti [FZJ$^+$04; JFM$^+$02; ENS07] and ^{54,56,58}Cr [PMB$^+$01; ENS07]. The energies for Cr isotopes are given in

Isotope	N	$E(2^+)$ (keV)
^{54}Cr	30	834.855(3)
^{56}Cr	32	1006.9(1)
^{58}Cr	34	880.7(2)

Table 4.1.: Energies of the first excited states in Cr isotopes [ENS07; PMB$^+$01]. The excitation energy is larger in ^{56}Cr compared to its neighbors, ^{54}Cr and ^{58}Cr.

table 4.1. The maximum for ^{56}Cr may be interpreted as a sign for an enlarged shell gap [PMB$^+$01]. Also for $_{22}$Ti isotopes, a maximum in the $E(2^+)$ has been observed at $N = 32$ [FZJ$^+$04; JFM$^+$02; ENS07].

From the theoretical side a sub-shell closure at $N = 34$ for Ca, Ti and Cr isotopes has been predicted [HOBM04; HOBM02; OUF$^+$02] based on calculations using the GXPF1 interaction. The calculations show that an enlarged gap may be expected between the $p_{1/2}$ and $f_{5/2}$ neutron orbitals. In contrast to expectations, these calculations do not predict a minimum in the $B(E2)$ values at $N = 30 \ldots 34$ [HOBM04, fig. 13].

The purpose of the present experiment was to investigate the development of $B(E2)$ values around the $N = 32$ in Cr isotopes. A similar experiment, run at almost the same time at MSU, aimed at measuring $B(E2)$ values in Ti isotopes with the same motivation.

4.2. Experimental Considerations

Coulomb excitation is a powerful tool for measuring $E2$ transition probabilities, from which nuclear deformation parameters may be derived. While many experiments have been performed using this technique at low, *safe* energies below the Coulomb barrier [CGK$^+$07; HBJ$^+$07], Coulomb excitation experiments are also possible using beams of higher energies [BGF$^+$05; DJG$^+$05]. Low beam intensities can then be compensated by large target thicknesses that could not be penetrated with low-energy beams. A review on this technique is given in [Gla01].

In the present experiment, the exotic Cr nuclei were produced by fragmentation of a high-energy ^{86}Kr beam of around 480 MeV/u. They were then slowed down and impinged on the Coulomb excitation target at an energy of about 140 MeV/u. The beam has relatively large spreads in angle and momentum distributions, which necessitates a tracking of the beam particles. The tracking allows a precise correction of Doppler shifts and the determination of the scattering angle, which is needed to discriminate between Coulomb excitation events and other nuclear reactions. At the high beam energy, other reactions are not unlikely so that a particle identification is required after the target. If, as in the present experiment, the beam cannot be made isotopically pure, an identification of the particles impinging on the target is necessary, too. In addition, the process of slowing down the beam particles involves the production of background radiation, like, e.g., Bremsstrahlung, which then contributes to the rather large background.

4.3. Experimental Setup

The experiment was run at *GSI* (Gesellschaft für Schwerionenforschung) near Darmstadt, Germany. In August 2003, a new experimental setup named *RISING* (Rare ISotopes INvestigation at GSI) had been installed at this site. In September 2003, difficulties with running the new setup left a first attempt to measure $B(E2)$ values in Cr isotopes unsuccessful. A second attempt in May 2004 finally gave the results presented here.

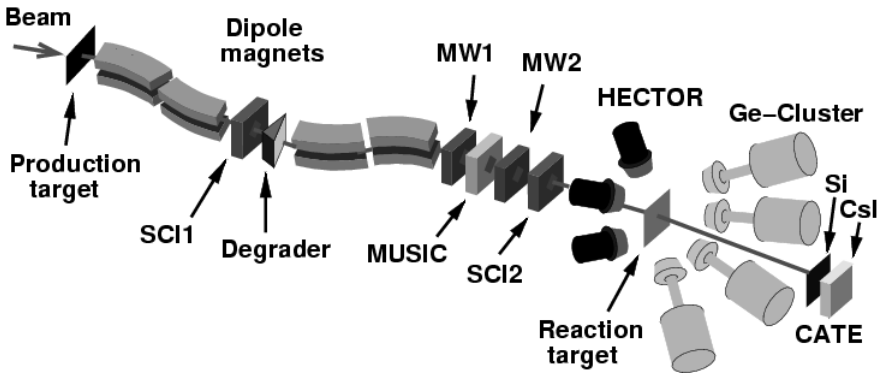

Figure 4.1.: Schematic overview of the RISING setup at GSI. The BaF_2 scintillation detector array *HECTOR* has been ignored in the analysis of the present experiment. An additional degrader between the first two dipole magnets (see text) is not drawn here. Sizes and distances have been scaled arbitrarily for the figure.

The setup includes many detectors and will be described in several steps, starting from the primary ion beam (section 4.3.1) and ending with the beam-stopping detector *CATE* (Calorimeter Telescope) (section 4.3.5). A schematic overview of the setup, excluding the accelerators, is shown in figure 4.1.

4.3.1. Particle Beam

The particle beam was produced, accelerated and selected in several steps. The primary beam of ^{86}Kr was produced in the ion source and guided into the linear accelerator *UniLAc* (Universal Linear Accelerator). This pre-accelerated beam was then injected into the heavy-ion synchrotron *SIS* (Schwer-Ionen-Synchrotron). At the extraction from SIS, the beam particles had an energy of about 480 MeV/u. The beam intensity at this point was around 1 to $5 \times 10^9\,\mathrm{s}^{-1}$.

The accelerated beam was then directed onto a primary Be target of $2.5\,\mathrm{mg/cm}^2$ thickness. Here, a portion of the beam particles reacts with the Be nuclei. At this energy, the dominant reaction channel is fragmentation. Many nuclei with different A and Z values are produced in the target. In order to have a large number of reactions, a thick target is used. This widens the momentum distributions parallel and perpendicular to the beam through *straggling*. Also the fragmentation reactions themselves impose a momentum distribution on the beam [Gol74].

The largest component of the beam after the target is still the primary beam. The distribution of the reaction products can be calculated with, e.g., EPAX [SB02]. The most abundant products in the beam are stable isotopes, while unstable nuclei represent a smaller fraction.

Besides this fragmentation technique, it is also possible to produce secondary beams by fission from, e.g., a uranium beam. For the present experiment, the fragmentation of Kr promised a higher yield of ^{56,58}Cr.

4.3.2. The Fragment Separator FRS

To select the desired isotopes and to reduce the intensity of unwanted contaminants, the fragment separator *FRS* is used at GSI [GAB+92]. It corresponds to the α spectrometer at GANIL (see section 3.2.2). Its main components are four dipole magnets and degrader foils. While normally only one degrader is used between the two pairs of dipoles, in this experiment an additional foil was inserted between the two dipoles of the first pair (see fig. 4.1). As in the α spectrometer, the deflection of the charged beam particles in the FRS dipoles allows a selection of the $B\rho$ value, while the degraders permits a selection of Z, making use of the Z-dependent energy loss in the aluminum foils.

The settings of the dipole magnetic fields and the widths of the primary target and the degrader foils was chosen to optimize the rate of the desired Cr isotope at the secondary target. With these settings, the secondary beam at the exit of the FRS was not a single-isotope beam. Instead, it contained admixtures from neighbors in the nuclear chart, mainly ${}_{23}V$ and ${}_{25}$Mn isotopes. These beam impurities necessitated the identification of the beam particles reaching the secondary target.

4.3.3. Secondary Beam Detectors

The identification of the secondary beam particles before the Coulomb excitation target was made using time-of-flight and energy loss measurements.

The time-of-flight measurement was set up between two plastic scintillators in the focal planes S2 and S4. In figure 4.1, they are labeled SCI1 and SCI2, respectively. These scintillators were used because of their good time resolution of typically 100 ps [WAB+05]. The additional degrader foil in the first dipole pair was introduced to reduce the rate of the beam incident on SCI1, which is located before the slits, to an acceptable value. From the time-of-flight and the $B\rho$ value, the mass-to-charge ratio A/Q of each ion can be measured.

Two multi-wire detectors (MW1 and MW2 in fig. 4.1) [Ste91] were installed in the beam line 1930 and 1065 mm before the target. Each of them measures the position of the incoming beam particles with a resolution better than 1 mm [WAB+05]. The combination of both yields the particle direction and, assuming that no scattering takes place, the reaction point on the target by extrapolation.

Between these tracking detectors, 1481 mm before the target, an ionization chamber *MUSIC* (Multi-Sampling Ionization Chamber) [SS00] was inserted in the beam line. The particles passing through the MUSIC lose energy while ionizing the CF_4 gas along their path, a process that depends on their charge Z. The amplified and collected charge yields the energy loss and thus allows to determine the charge Z of the beam particles.

4.3.4. Target and γ-Ray Detectors

The secondary target for Coulomb excitation was a foil of Au with a thickness of $1\,\mathrm{g/cm^2}$ and a surface of $7 \times 7\,\mathrm{cm^2}$. The gold material was chosen to have a large Coulomb excitation cross section due to the large $Z = 79$. Furthermore, no disturbing lines are

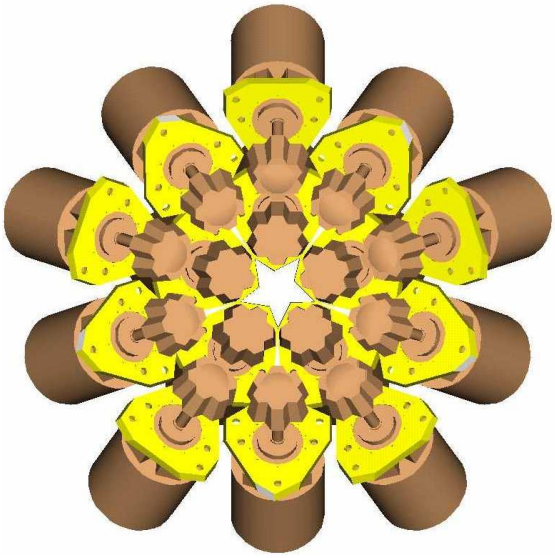

Figure 4.2.: Schematic view of the Cluster Ge detectors in the RISING setup [RIS].

expected from this target, only one line at 547 keV [ENS07], far below the transition energies of the Cr isotopes under investigation.

To detect the γ radiation from the de-excitation of the 2^+ states populated by Coulomb excitation, 15 Ge Cluster detectors from the former EUROBALL [KL03] were placed at the target position. Each of the detectors consists of 7 closely packed Ge crystals [ETB+96], so that altogether 105 crystals are included in the RISING setup. As shown in figure 4.2, the detectors are mounted in forward direction and are arranged in three rings with angles of 15, 30 and 35 °, respectively, against the beam axis. The distance from the detector surface to the target was adjusted to 72 cm, which results in an opening angle of around 3 ° for each crystal. This geometry was chosen to combine a small Doppler broadening and a high detection efficiency for the γ rays emitted in flight (see [WAB+05]). For an isotropic γ-ray emission in the rest frame of the nucleus, the γ rays are forward-focused in the laboratory system due to the relativistic velocity of the nucleus.

Shielding against background radiation. When the beam is passing through the various beam detectors and the target, not only the desired population of the 2^+ state takes place, but also unwanted background radiation appears from various processes. For example, Bremsstrahlung is emitted when charged particles, mostly electrons, are accelerated. Photons emitted in this process have energies mainly below 300 keV for a gold target and 100 MeV/u particle energy [WAB+05; HGK+92; ASM+86; KM59]. To suppress low-energy background radiation from such processes, the detectors were protected with shielding material. On the side facing the target, photons had to traverse a composite material with layers of 1 mm lead, 2 mm tin and 2 mm aluminum to reach the Ge detector. From the rear side, photons had to pass through a shield made of 2 mm aluminum and 4 mm lead to reach the detector. The sides of the detectors and the beam tube at the Ge detector position were wrapped with 2 mm lead.

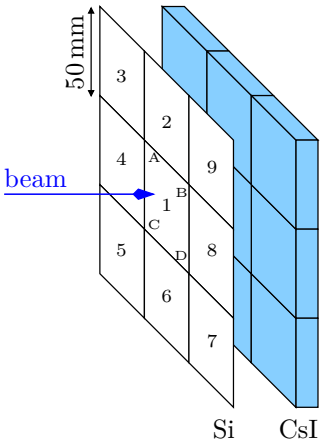

Figure 4.3.: Schematic view of the CATE detector [LMG+05]. Beam particles lose energy in the position-sensitive Si detectors and are then stopped in the CsI scintillators.

4.3.5. The Detector CATE

In addition to the Coulomb excitation process, fragmentation reactions have a significant cross section at the present beam energies. Therefore, the particles after the secondary target have to be identified again in A and Z. To achieve this, the detector CATE (*Calorimeter Telescope*) was installed at the end of the beam line, 1.4 m behind the target [WAB+05, sec. 4]. As shown in figure 4.3, CATE is divided into 9 segments, each of which has a position-sensitive Si detector of 300 μm thickness followed by a CsI scintillator that stops the beam.

The active area of each Si segment has a surface of $50 \times 50\,\mathrm{mm}^2$. Each segment is covered with a resistive layer, and is read out centrally on one side, and at the four corners on the other surface, which allows to determine the position from the relative signal intensities. The CsI detectors have a size of $54 \times 54\,\mathrm{mm}^2$ and are located 4 cm behind their respective Si segment. They are read out via photo diodes. The CATE detector covers an opening angle of 58 mrad. The particle identification uses the energy loss ΔE measured in the Si detector, and the remaining kinetic energy E measured in the CsI scintillator to identify ions in Z and A. From the measured position, the scattering angle of the ion can be calculated from the particle direction measured with the multi-wire detectors before the target.

4.4. Experiment and Data Analysis

Information about the three experiments performed to study ^{54}Cr, ^{56}Cr and ^{58}Cr is summarized in table 4.2. Around 20 h of beam time were devoted to each of ^{54}Cr and ^{56}Cr. Due to the lower beam intensity, the setting on ^{58}Cr was kept for around 55 h. In all three cases, the $^{A}_{24}$Cr beam contained the neighboring isotopes $^{A+1}_{25}$Mn and $^{A-1}_{23}$V with significant abundances.

The new $B(E2)$ values were to be measured relative to the known value of ^{54}Cr. To make the measured intensities comparable, the setup and the beam energy on the secondary target were changed as little as possible during the experiment. Small changes

Table 4.2.: Run durations, beam intensities and abundances of the desired Cr isotopes for the three runs of the experiment. The abundances were determined using the particle identification before the Au target.

Isotope	beam time (h)	intensity (s^{-1})	^{A}Cr abundance (%)	other components
^{54}Cr	22	2000	45	^{55}Mn, ^{53}V
^{56}Cr	20	1400	35	^{57}Mn, ^{55}V
^{58}Cr	55	600	25	^{59}Mn, ^{57}V

were, of course, necessary to change the beam composition.

For all three runs, the same target was used. The beam energy was adjusted to 136 MeV/u before the secondary target in all three settings. This leads to beam energies of 100 MeV/u after the target.

The data acquisition was triggered by one of two conditions: a particle-γ-coincidence condition, or a particle condition. A particle-γ-coincidence was recorded if

1. at least one of the Ge crystals detected a γ ray,
2. the plastic scintillator in front of the target (SCI2 in fig. 4.1) had detected an ion, and
3. an ion was also detected in one of the 9 CsI detectors of CATE.

A particle condition was given if the two last requirements were fulfilled. The data acquisition recorded all events with a particle-γ-coincidence plus every 256$^{\text{th}}$ event with a fulfilled particle condition.

4.4.1. Sub-Event Matching

For a faster read-out of the many detectors, the data acquisition was split. Three computers were responsible for processing the signals of the detectors of the branches *HECTOR* (see fig. 4.1), *FRS* and *Germanium*, respectively, where the *FRS* branch included all the beam particle detectors. All these systems shared a common trigger, and they were synchronized by a common clock signal. For a valid trigger signal, the detectors as well as the 'time' value of the clock were read out and then stored together in sub-events. Another computer system joined the three data streams, ordering the sub-events according to their timestamps.

As a first step of the analysis, these sub-events were to be recombined to complete events. The differences of time-stamp values for pairs of the three branches have fixed, but not necessarily vanishing values which are, e.g., affected by cable lengths. These 'good' difference values show as peaks in spectra of time differences above a very low background which is caused, e.g., by the permanent 50 Hz LED calibration of the hector array uncorrelated with beam particles. To reconstruct complete events, pairs (or triples,

if Hector data are included) of sub-events with such 'good' time difference values have been combined.

This reconstruction needs only to be done for events with the particle-γ-trigger. For particle-only events, no sub-event from the Germanium branch needs to be present. Therefore, the presence of two matching sub-events must not be made a requirement.

4.4.2. Detectors for γ Radiation

Energy and Efficiency Measurement

The energy calibration of the Cluster Ge detectors was done using a ^{152}Eu source. Compared with the calibration of the BaF_2 detectors for the GANIL experiment, the Ge calibration was relatively simple. The lines from the ^{152}Eu source can be resolved with the Ge detectors, yielding at the same time an energy calibration for all relevant γ-ray energies and the energy-dependence of the detector efficiency from a comparison of measured and tabulated intensity values.

Absolute Efficiency. The procedure for the efficiency measurement is described in Appendix D. Using this procedure, an efficiency value of 1.13(1) % at 1.33 MeV was obtained for γ rays emitted at rest. For radiation emitted in flight at $v/c \approx 0.43$, the efficiency increases to about 2.3 % due to the Lorentz boost and the placement of the detectors in forward direction.

Add-Back Procedure

Due to Compton scattering and pair production, the energy signal of the Ge detector does not always correspond to the energy of the interacting γ ray. To obtain higher photo-peak efficiencies, an add-back procedure was applied to the data (cf. sec. 3.3.9). In the case of the cluster detectors, only energies of crystals measured in the same cluster were added, if the difference of detection times did not exceed a threshold, and only if hits were distributed as in the patterns described in [Neu01].

Doppler Correction

As the γ rays are emitted by moving ions, the energies observed in the laboratory system are affected by the Doppler effect (cf. sec. 3.3.8). To reconstruct the γ-ray energy in the rest frame of the ion, the emission angle with respect to the flight direction and the particle speed have to be known.

The angle θ is calculated from the positions measured with the particle tracking detectors (see fig. 4.4). The individual Ge crystals have an opening angle of about 3 °, limiting the granularity of the calculation of θ.

The velocity is calculated from the measured time-of-flight between the scintillators SCI1 and SCI2 (see fig. 4.1). The coefficients have been obtained from a simulation made with the code `MOCADI` [IGM+97] and then fine-tuned to reproduce the known transition energies.

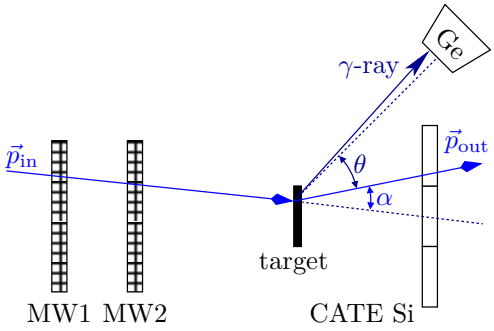

Figure 4.4.: The tracking of the incoming ($\vec{p}_{\text{in}}$) and outgoing ($\vec{p}_{\text{out}}$) beam particles using extrapolation from the two multi-wire detectors (MW1 and MW2) and the position-sensitive Si detectors of CATE allows to determine the scattering angle α and the angle θ between outgoing particle and γ-ray detector.

After this correction for the Doppler shift, an energy resolution of 2 % was reached.

Time Gate

Figure 4.5 shows a time-energy matrix for the ^{54}Cr dataset. It is visible that the $2^+ \rightarrow 0^+$ transition is observed mostly inside a narrow time window. Other radiation arrives at different times, like, e.g., the background radiation produced by the stopping of the ions in the CATE CsI scintillators which arrives later than the γ rays emitted near the target. To suppress the background radiation, only γ rays falling in the indicated time window were accepted in the analysis.

4.4.3. Particle Identification and Tracking

Incoming particles. The identification of the incoming beam particles using the FRS and MUSIC works very well. Figure 4.6a shows a typical particle identification matrix for the run with ^{54}Cr. The three main beam components, ^{54}Cr, ^{55}Mn, and ^{53}V, are clearly separated.

Outgoing particles. The identification of the outgoing particles with CATE is not as accurate as the incoming beam identification. Figure 4.6b shows that it yields a clear separation in Z, while different masses of the nuclear species are not showing up as distinct peaks. As a workaround, the following steps were taken to select the Coulomb excitation channel as accurately as possible:

1. CATE $\Delta E - E$ identification matrices were produced with a condition on the incoming beam. Due to the excellent identification with FRS/MUSIC and the rather small fraction of reacting particles in the Au target, the dominant part of the outgoing beam is also the selected Cr isotope.

2. A set of rather narrow and rather wide polygon gates, both selecting the dominant ^{A}Cr, were defined in the CATE identification matrices.

3. From these, a series of polygon gates was calculated by interpolation, changing the size of the polygon in small steps between the previously defined narrow and wide gates.

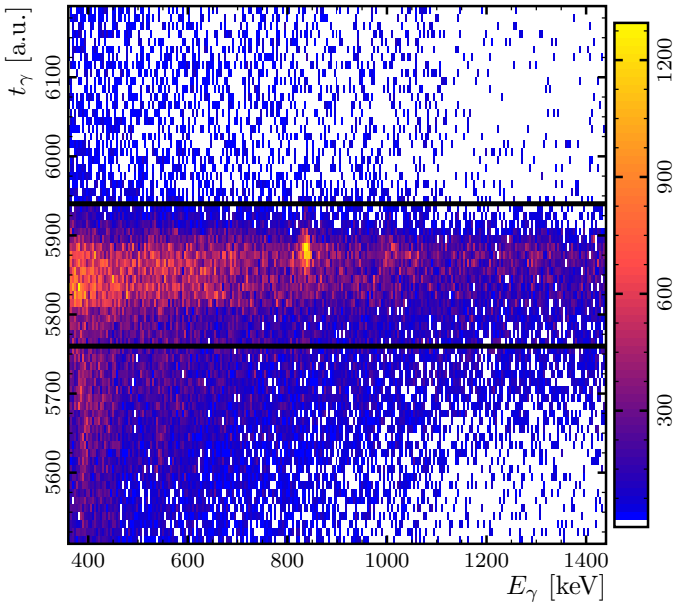

Figure 4.5.: Time-energy matrix for ^{54}Cr showing the Doppler-shift corrected γ-ray energies correlation to the detection times in the Ge detectors. The $2^+ \rightarrow 0^+$ transition is observed inside a narrow time window. The time gate applied in the analysis is indicated by the thick lines.

4. The intensity of the γ line was determined for all these polygon gates.

5. The element in the series of gates where the intensity starts to saturate was searched. Finally the average intensity of four neighboring gates, around and including the selected element, was used for the calculation of $B(E2)$ values.

As the $B(E2)$ values have been determined with a measurement relative to ^{54}Cr, possible mis-identifications can be expected to at least partially cancel out when taking the ratio of measured line intensities.

Scattering angle. The scattering angle resolution is limited in the present setup mainly due to the angular straggling in the Au target. According to `Geant4` or `ATIMA` [Wei07], the angular straggling has a magnitude of about $1.3\,^\circ \approx 24\,\mathrm{mrad}$ FWHM. An additional uncertainty comes from the scattering angle calculation. The position measurement uncertainty is about 1 mm for the two multi-wire detectors [WAB+05] and 7 mm for CATE [WAB+05]. Therefore, the scattering angle α calculated from these measurements (see fig. 4.4) has an uncertainty of $0.35\,^\circ \approx 6\,\mathrm{mrad}$ (see Appendix C). The total uncertainty is thus dominated by the angular straggling. The scattering angle uncertainty is about $1.4\,^\circ \approx 24\,\mathrm{mrad}$ in the laboratory system, and about $3.1\,^\circ$ in the c.m. system.

The scattering angle gate was therefore chosen to exclude the smallest scattering angles (below $0.6\,^\circ$ in the laboratory system) to reduce the atomic background, and to exclude

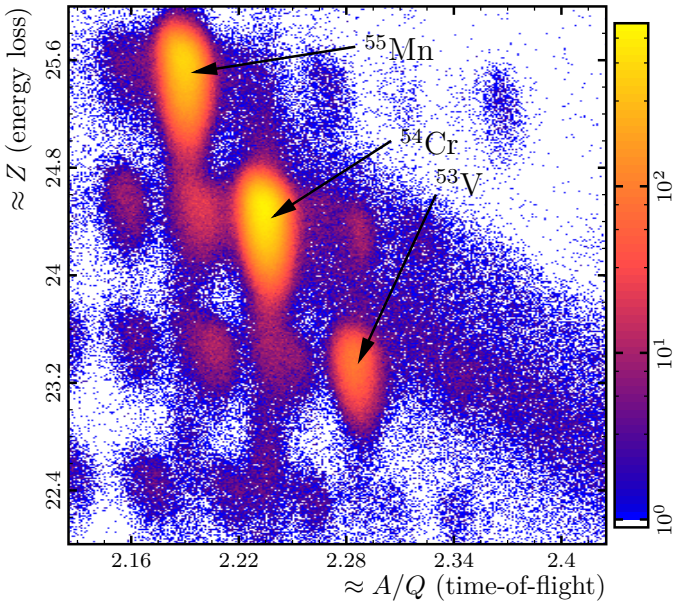

(a) Identification of incoming particles with FRS and MUSIC. The peaks corresponding to ^{54}Cr, ^{55}Mn, and ^{53}V are labeled.

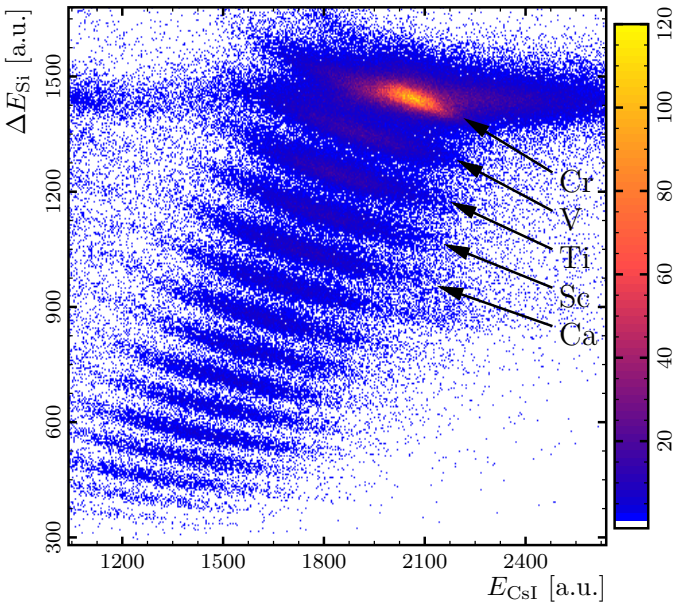

(b) Identification of outgoing particles with CATE, with a condition on incoming Cr. While the Z discrimination works well, masses for the same Z cannot be distinguished.

Figure 4.6.: Identification of incoming on outgoing particles in the RISING experiment. The matrices are for the ^{54}Cr runs.

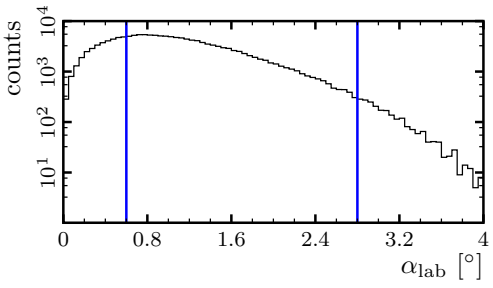

Figure 4.7.: Laboratory scattering angles of ^{54}Cr ions as measured with the RISING setup. The chosen scattering angle gate is indicated by the lines.

the largest scattering angles (above 2.8 °) to reduce contributions from nuclear reactions. The window of accepted scattering angles is indicated in figure 4.7.

4.4.4. Gamma-Ray Energy Spectra

Figure 4.8 shows typical γ-ray energy spectra obtained for the three Cr isotopes with the procedure described above. The energies have been corrected for the Doppler shift, and the intensities for the efficiencies of the Ge detectors.

Lines from other nuclei in the spectra would not affect the final result. Due to the excellent identification before the Au target, they would have to originate from a reaction of the selected Cr isotope in the target. Due to the sufficient Z resolution of CATE, other lines would have to originate from other Cr isotopes which could have been produced by transfer or knockout reactions. They have been ignored in the γ-ray energy spectrum for the intensity calculation as the excitation energies are known and the number of reacting particles is small.

4.5. Results

The intensities I_γ of the $2^+ \rightarrow 0^+$ transitions were determined by integration of the peak area above the background. An angular distribution of the intensities was not taken into account. Such a distribution can be expected to be almost identical for the three nuclei, and since the $B(E2)$ values shall be determined relative to the known value for ^{54}Cr, not accounting for it should be negligible compared to the statistical errors.

In principle the $B(E2)$ values could be calculated from the reaction cross sections for the Coulomb excitation. Models for such calculations exist [Gla01; BCG03], but they require the input of several parameters. Using this approach for the present experiment, the parameters would have been chosen to reproduce the ^{54}Cr $B(E2)$ value. Then they would have been adapted to the heavier isotopes to calculate new $B(E2)$ values. Effectively, the new values would thus be calculated relative to the known ^{54}Cr value using the model as an intermediate step. To avoid (possible systematic errors due to) this intermediate step, the cross section ratios were used directly to calculate the new values. Assuming that systematic problems, like, e.g., feeding from higher excited states, particle identification problems after the Coulomb-excitation target, and the already-mentioned

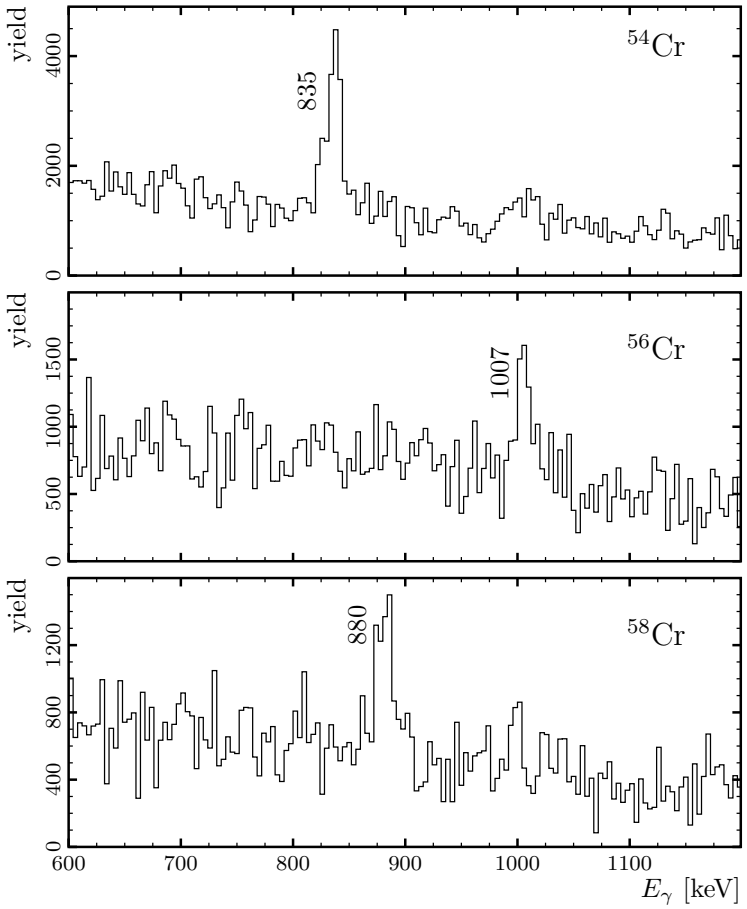

Figure 4.8.: Typical energy spectra for the chromium isotopes ^{54}Cr (upper panel), ^{56}Cr (middle), and ^{58}Cr (lower panel). The energies are corrected for the Doppler effect and the intensities for the energy-dependent efficiency. The known transition energies are visible as distinct lines (see table 4.1).

Table 4.3.: The energies (E_γ) and intensities of the $2^+ \rightarrow 0^+$ transitions with (I_γ) and without (N_γ) correction for the Ge detector efficiency are listed together with the number of projectiles identified before and after the target, (N_{pro}), and the $B(E2; 2_1^+ \rightarrow 0^+)$ values for ^{54,56,58}Cr.

Isotope	N_{pro} /10^6	N_γ	I_γ /10^2	$B(E2)$ (W.u.)	$E(2_1^+)$ (keV)
^{54}Cr	37.4	501(64)	211(27)	14.6(6)[a]	835[a]
^{56}Cr	17.5	126(44)	61(20)	8.7(30)	1007[a]
^{58}Cr	11.6	148(43)	73(19)	14.8(42)	880[b]

[a] from ref. [ENS07]
[b] from ref. [PMB+01]

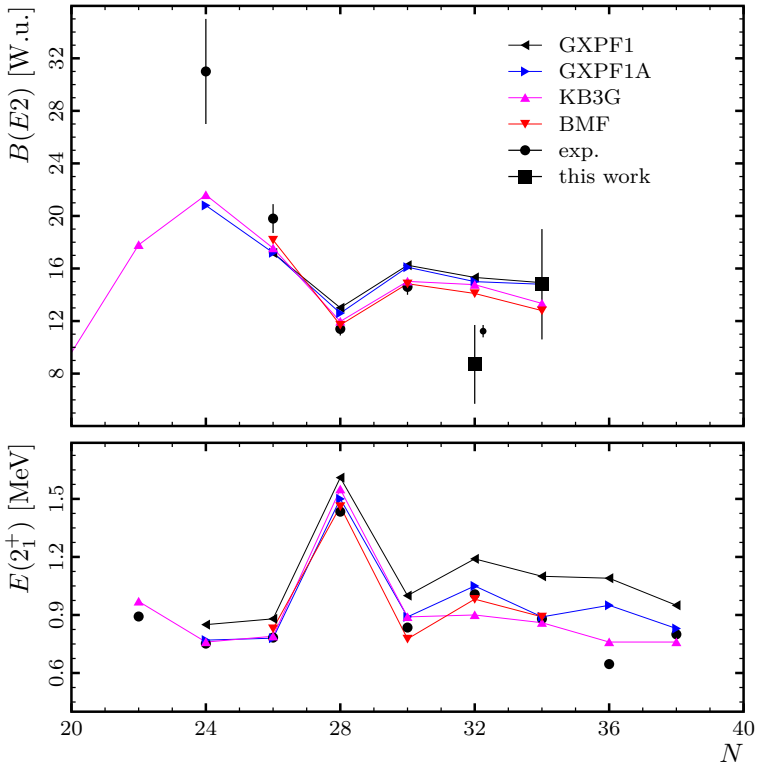

Figure 4.9.: Comparison of calculated and experimental $B(E2;\downarrow)$ values as a function of the neutron number N for Cr isotopes. In the calculations, the GXPF1A (▶), GXPF1 (◀), and KB3G (▲) [OSF+05; HOBM04; CNP02] interactions were used. A calculation using the beyond-mean-field technique (▼) is also included [RE07]. Calculated and experimental energies are shown for comparison. Experimental values are from Refs. [ENS07; PMB+01] (●), from [SRD+06] (●, shifted aside), and from this work (■).

angular distribution are very similar for the three nuclei, such effects cancel when taking the ratio of intensities.

The $B(E2)$ values presented in table 4.3 have been determined using

$$B(E2, {}^{A}\mathrm{Cr}) = \frac{I_\gamma({}^{A}\mathrm{Cr})/N_{\mathrm{pro}}({}^{A}\mathrm{Cr})}{I_\gamma({}^{54}\mathrm{Cr})/N_{\mathrm{pro}}({}^{54}\mathrm{Cr})} B(E2, {}^{54}\mathrm{Cr}) \tag{4.1}$$

where I_γ is the intensity of the line corrected for the energy-dependent efficiency. The errors included in the table for ^{56}Cr and ^{58}Cr comprise the statistical uncertainties and the uncertainty in the reference $B(E2)$ value of ^{54}Cr. The projectiles numbers N_{pro} includes particles in the scattering angle range. Despite the large error bars, it is apparent that the $N = 32$ Cr isotope has a lower $B(E2)$ value than its even-mass neighbors.

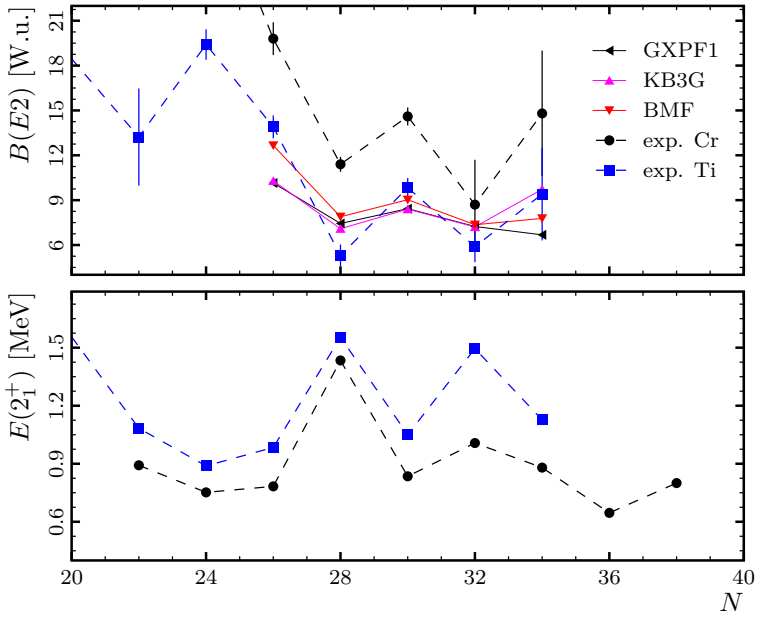

Figure 4.10.: Comparison of calculated and experimental $B(E2)\uparrow$ values as function of the neutron number N for Cr and Ti isotopes. Calculated values for Ti isotopes [PNC05, fig. 2] using the GXPF1 (◀) and KB3G (▲) interactions, as well as calculations using the beyond-mean-field technique (▼) [RE07] are shown together with experimental values for Ti (■)[DJG+05] and Cr (●) [see fig. 4.9].

4.6. Discussion

Experimental and theoretical energies and $B(E2)$ values for Cr isotopes are compared in figure 4.9. The evolution of experimental $B(E2)$ values shows that the collectivity of the excited 2^+ state in ^{56}Cr with $N = 32$ is lower than in the neighboring nuclei, ^{54}Cr and ^{58}Cr with $N = 30$ and $N = 34$, respectively. The $B(E2)$ value has about the same magnitude for $N = 32$ as for the magic neutron number $N = 28$. This result provides further evidence for the existence of an enlarged $N = 32$ sub-shell gap and confirms the previous assumptions based on the $E(2^+)$ systematics.

Since the RISING experiment, new experimental data regarding the $N = 32$ shell gap have become available, both for Cr and Ti isotopes.

In an experiment at the tandem accelerator in Cologne, the lifetime of the 2^+ state in ^{56}Cr has been measured with high accuracy using the Recoil-Distance-Method [SRD+06]. The corresponding $B(E2)$ value of 11.23(47) W.u. has been included in figure 4.9. It is in agreement with the value measured in the RISING experiment. In the Cologne experiment, a ^{11}B beam with an energy of 32 MeV impinging on a ^{48}Ca target was used to produce ^{56}Cr in the reaction ^{48}Ca(^{11}B,p2n)^{56}Cr. The ^{56}Cr ions were then stopped in a plunger foil after the target. The de-excitation of excited states via γ radiation was observed with Ge detectors surrounding the plunger device. From the

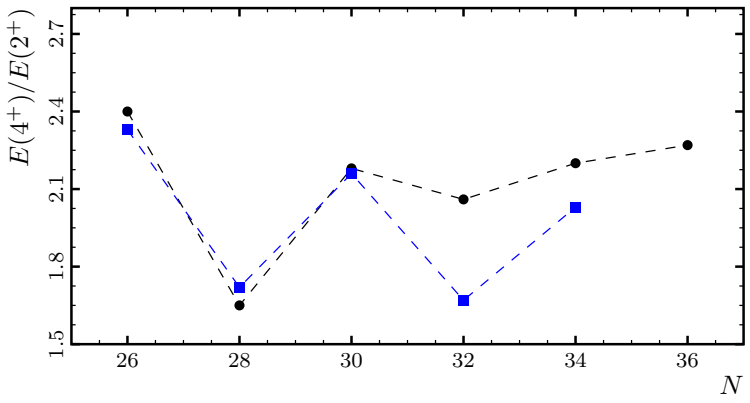

Figure 4.11.: Evolution of the energy ratios $E(4^+)/E(2^+)$ for Cr (-●-) [MLG+06] and Ti (-■-) [FZJ+04; JFM+02] isotopes. In both isotopic chains, a minimum is visible for $N = 32$. This is further evidence for an enlarged shell gap at this neutron number.

intensity ratio between Doppler-shifted and unshifted lines, the lifetime of the 2^+ state and the $B(E2; 2^+ \rightarrow 0^+)$ value were determined using the differential decay curve method [DHB89].

Figure 4.9 includes the results of several theoretical calculations for energies and $B(E2)$ values in Cr isotopes. Two calculations use the effective NN interactions `GXPF1` [HOBM04] and `KB3G` [CNP02], respectively, in the pf model space. The `GXPF1` interaction was recently modified (`GXPF1A`) to better account for the $E(2_1^+)$ energies in Ti and Cr isotopes [OSF+05]. As figure 4.9 shows, this modification has only a very small effect on the $B(E2)$ values. Besides these shell model calculations, also results from 'beyond-mean-field' calculations exist [RE07]. While all of these calculations show good agreement with the excitation energies, none of them describes the staggering of $B(E2)$ values as observed in the RISING and Cologne experiments. Instead, the theoretical $B(E2)$ values show a rather constant trend from $N = 30$ to 34.

Reduced transition probabilities have recently been measured in Ti isotopes at MSU [DJG+05], too. The evolution of $B(E2)$ value in Cr and Ti isotopes is compared in figure 4.10. The comparison shows that the result for Cr is in agreement with the observed decrease in collectivity for ^{54}Ti with $N = 32$. For Ti, the agreement between calculation and experiment is slightly better than for Cr in the sense that at least the shell model results obtained with the KB3G interaction reproduce the observed staggering.

Recently, excitation energies have been measured up to higher spins in ^{56}Cr and ^{58}Cr [ZDF+06; MLG+06]. The development of the energy ratio $E(2^+)/E(4^+)$ for the Cr and Ti isotopic chains is shown in figure 4.11. Both curves show a minimum at $N = 32$, which is further evidence for an enlarged shell gap at this neutron number.

All these experimental results indicate an enlarged sub-shell gap at $N = 32$ in Cr and Ti, i.e. between the orbitals $p_{3/2}$ and $p_{1/2}$. On the other hand, no signs for the predicted gap at $N = 34$ between $p_{1/2}$ and $f_{5/2}$ are visible.

5. Summary

In the present thesis, the shell structure in exotic nuclei has been investigated. The focus of the work was on finding new experimental data in neutron-rich Cr and proton-rich Ca isotopes.

The investigation of light Ca isotopes concentrated on the nucleus ^{36}Ca which was produced in a knockout reaction from a radioactive ^{37}Ca beam. For ^{36}Ca, the excitation energy of the first 2^+ state has been measured for the first time. Furthermore, momentum distributions were analyzed using a Monte-Carlo simulation of the knockout reaction. This analysis yielded the contributions of neutrons from individual orbitals to the total knockout cross section. In principle, these may be used to calculate spectroscopic factors, but such a calculation is hampered by difficulties of present knockout-reaction models in predicting precise single-particle cross sections. The measured branching ratio to the ground and excited states, on the other hand, is close to the predicted value. A remaining difference might be due to emission of protons which cannot be detected with the present experimental setup. Both the branching ratio and the large excitation energy are compatible with a large $N = 16$ gap in ^{36}Ca that leads to relatively pure configurations both in the ground state and the excited 2^+ state.

As a by-product of the experiment, two excitation energies in the $T = 2$ nuclei ^{32}Ar and ^{28}S have been confirmed, and two γ-ray transitions have been observed for the first time in ^{37}Ca. While the mirror energy differences in the $T = 2$ pairs ^{36}Ca–^{36}S, ^{32}Ar–^{32}Si, and ^{28}S–^{28}Mg can be reproduced in shell model calculations using a modified USD interaction, these modifications are not sufficient to explain the mirror energy differences for the pair ^{37}Ca–^{37}Cl.

In the heavy Cr isotopes, new experimental evidence for a sub-shell closure at $N = 32$ was found in a measurement of $B(E2)$ values using high-energy Coulomb excitation of radioactive beams. Prior to this experiment, the assumption of a sub-shell closure was based only on systematics of excitation energies of the first 2^+ states in Cr, Ti, and Ca isotopes. The small $B(E2)$ value for ^{56}Cr is in agreement with these indications. Further evidence for a $N = 32$ shell gap has meanwhile been found in the development of $B(E2)$ values in Ti isotopes and the evolution of $E(4^+)/E(2^+)$ ratios for Cr and Ti. While the experimental evidence has firmly established a sub-shell closure at $N = 32$, calculations are, at present, not able to reproduce the behavior of the $B(E2)$ values, whereas the evolution of excitation energies is well described.

Both results touch the limits of present nuclear structure models: in the Cr isotopes, the $B(E2)$ evolution cannot yet be reproduced, and in the Ca isotopes, a consistent picture of mirror energy differences as well as a successful calculation of cross sections are missing. As a result of this work, new experimental data are available for future improvements of such calculations.

A. Other Results from the GANIL Experiment

It is not uncommon for an experiment using fragmentation that a large number of nuclear species is produced and identified in addition to the nucleus of interest (cf. fig. 3.8). In the GANIL experiment for some of these nuclei γ-ray spectra with intensities sufficient for an analysis have been obtained. In the following sections, those spectra shall be presented that are believed to either confirm recent measurements, or to show transitions observed for the first time. Momentum distributions were not analyzed for these nuclei.

A.1. Spectroscopy of ^{37}Ca

For ^{37}Ca nuclei identified in SPEG, γ rays could be observed in coincidence. The process of population of these states was not investigated here. The number of γ rays is small compared to the number of ^{37}Ca ions in the beam, indicating that either the reaction cross section is small, or that most of the reacting ions do not reach the plastic scintillator of SPEG.

A γ-γ coincidence matrix for ^{37}Ca is shown in figure A.1a. While the presence of several coincidences is apparent, only for one of them quantitative results could be obtained here due to the low statistics and the insufficient energy resolution of the BaF_2 detectors.

Gamma-ray spectra in coincidence with γ-rays in the energy ranges 1.5–1.7MeV and 1.67–1.87MeV are shown in the upper and lower panel of figure A.1b, respectively. Each of them is dominated by one line. The energies of these lines have been determined as 1.78(4) MeV and 1.59(4) MeV, respectively. The latter energy is in good agreement with the energy of a previously known state in ^{37}Ca at an energy of 1613(17) keV [ENS07]. The former is observed for the first time. As the two γ rays are emitted in coincidence, they probably de-excite a state in ^{37}Ca at $\approx$ 3370(60) keV. The most likely corresponding state in the mirror nucleus, ^{37}Cl, is a $3/2^{(+)}$ state with an energy of 3627 keV. This state mainly decays directly ($\approx 57\,\%$) or through an intermediate state at 1726 keV ($\approx 42\,\%$) [ENS07]. Therefore the same spins are tentatively assigned to the states in ^{37}Ca. The direct decay of the state is, in analogy to Cl, also expected for Ca, but a corresponding transition cannot be resolved from the large structure at around 3 MeV in the ^{37}Ca γ-ray spectrum (see fig. A.1c).

A tentative partial level scheme for ^{37}Ca and ^{37}Cl is shown in figure A.2. The order of the included transitions is based on three arguments:

- The only known excited state in ^{37}Ca—which is probably the first excited state—

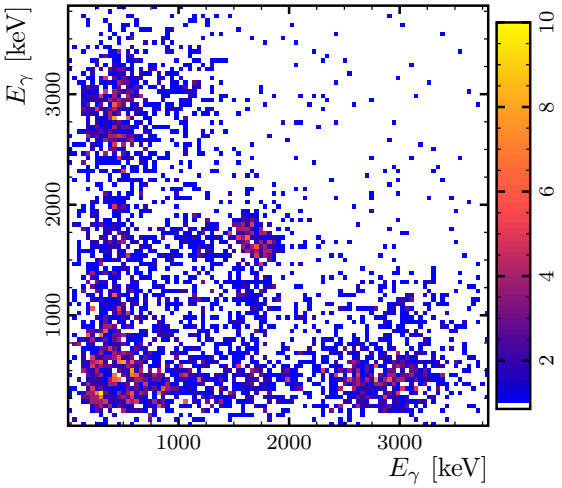

(a) Symmetric γ-γ-coincidence matrix. Only events with two γ rays after add-back were taken into account here.

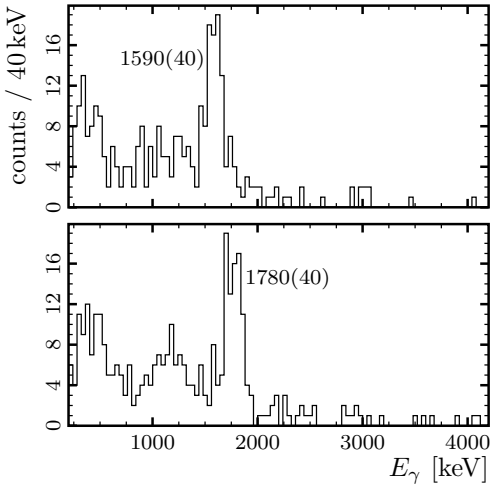

(b) Gamma rays in coincidence with 1500–1700 keV (lower panel) and 1670–1870 keV (upper panel).

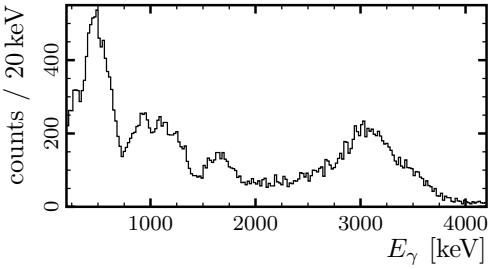

(c) γ-ray spectrum for ^{37}Ca. The broad structure at 3 MeV does not allow to identify a line with the energy sum of the two coincident lines seen in the matrix.

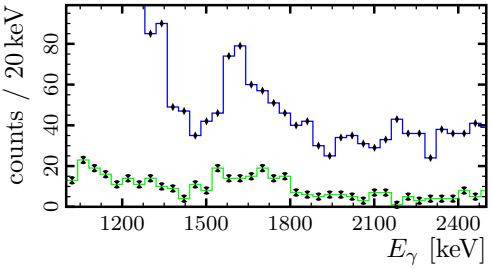

(d) γ-ray spectra for different multiplicities. At 1.6 MeV, more counts are visible than at 1.8 MeV for the multiplicity one (-✦-), while both intensities are similar for multiplicity two (-⧗-).

Figure A.1.: Gamma-ray spectra and matrices for ^{37}Ca.

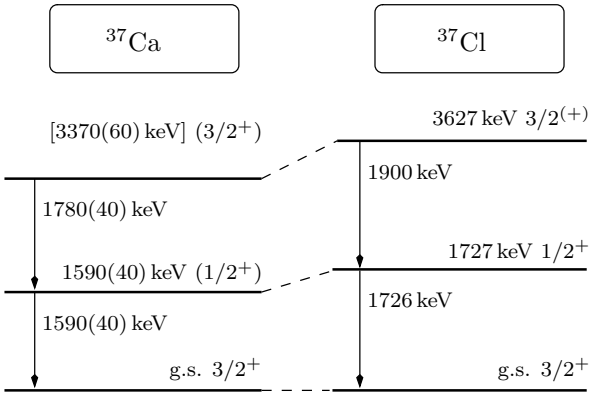

Figure A.2.: Partial level schemes for ^{37}Ca (tentative) and ^{37}Cl. The spin and parity assignments for the excited states are based on comparisons with the mirror nucleus, ^{37}Cl, and with shell-model calculations.

Table A.1.: Comparison of experimental and calculated excitation energies of the first 1_2^+ and the second $3/2^{(+)}$ for the mirror nuclei ^{37}Ca and ^{37}Cl. The energy difference between these is given in the row labeled E_γ. The calculation using the USD interaction yields the same results for Ca and Cl. The columns 'USDm' and 'USDm^2' show results using the modified USD interactions from [DGR$^+$07] described in sec. 3.6.1. The rows labeled Δ show the mirror energy differences for the respective rows above.

Energy		exp.		USD	USDm		USDm^2	
		Ca	Cl		Ca	Cl	Ca	Cl
$E(1/2^+)$	(MeV)	1.59(4)	1.73	1.84	1.72	1.99	1.70	1.99
Δ	(MeV)	0.14(4)			0.27		0.27	
$E(3/2_2^+)$	(MeV)	3.37(6)	3.63	4.11	3.97	4.31	3.96	4.31
Δ	(MeV)	0.26(6)			0.34		0.35	
E_γ	(MeV)	1.78(4)	1.90	2.27	2.25	2.32	2.26	2.32

has an energy of 1613(17) keV which agrees well with the lower of the two transitions observed here.

- The transitions de-exciting the mentioned $3/2^{(+)}$ state in ^{37}Cl have the same order: the transition to the intermediate state has a higher energy than the transition from there to the ground state.
- Finally, an intensity argument can be given: In a γ-ray spectrum for γ-ray multiplicity one, the 1.6 MeV transition has a higher intensity than the 1.8 MeV transition, while for multiplicity two, the intensities are similar. This is illustrated in figure A.1d. The argument is weakened by the fact that, for unknown reasons, this difference in intensity change is only observed for some of the runs, namely the last runs (457–521, cf. table 3.2).

The experimental energies are compared to shell model results in table A.1. Shell model calculations were made using both the standard USD interaction and the modified USD interactions described in sec. 3.6.1 (cf. [DGR$^+$07]). While the modifications account for the mirror energy differences in the $T = 2$ mirror pairs with $A = 28$, 32

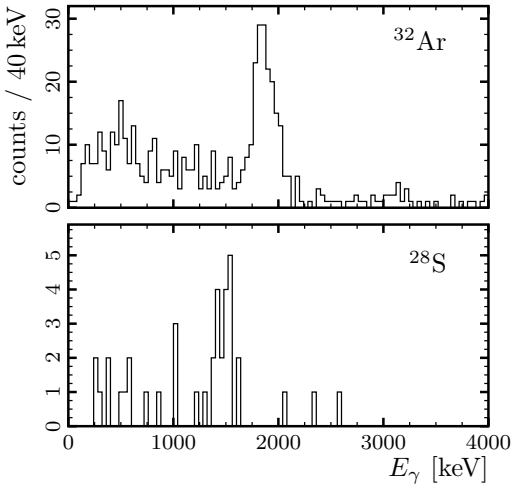

Figure A.3.: Gamma-ray spectra for the nuclei ^{32}Ar and ^{28}S. These were obtained with a ^{36}Ca secondary beam. The energies of the lines are 1873(20) keV and 1525(30) keV, respectively. Both values agree with [YOG$^+$06].

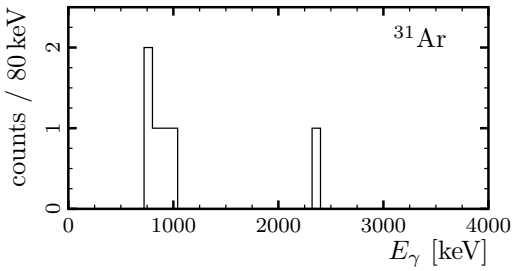

Figure A.4.: Gamma-ray spectrum for the nucleus ^{31}Ar. The centroid of distribution below 2 MeV is at 857 keV.

and 37, apparently neither the level energies nor the mirror differences observed for the $T = 3/2$ pair with $A = 37$ are reproduced in any of the calculations.

A.2. Spectroscopy of ^{32}Ar and ^{28}S

For the two nuclei ^{32}Ar and ^{28}S, γ-ray energy spectra are shown in figure A.3. The energies of the lines are 1873(20) keV and 1525(30) keV, respectively. The energy of the first 2^+ state in ^{28}S had been measured previously [YOG$^+$06], and has been confirmed here. For ^{32}Ar, two different energy values had been measured previously: 1824(12) keV [CHP$^+$02], and 1857(8) keV [YOG$^+$06]. The value measured here confirms the latter result.

Both ^{32}Ar and ^{28}S are, like ^{36}Ca, $|T_z| = 2$ nuclei. The mirror energy differences are included in figure 3.18.

A.3. Spectroscopy of ^{31}Ar

In total, only 50 ^{31}Ar nuclei have been detected in the focal plane of SPEG. A spectrum of γ rays in coincidence with these nuclei is shown in figure A.4. Despite the small

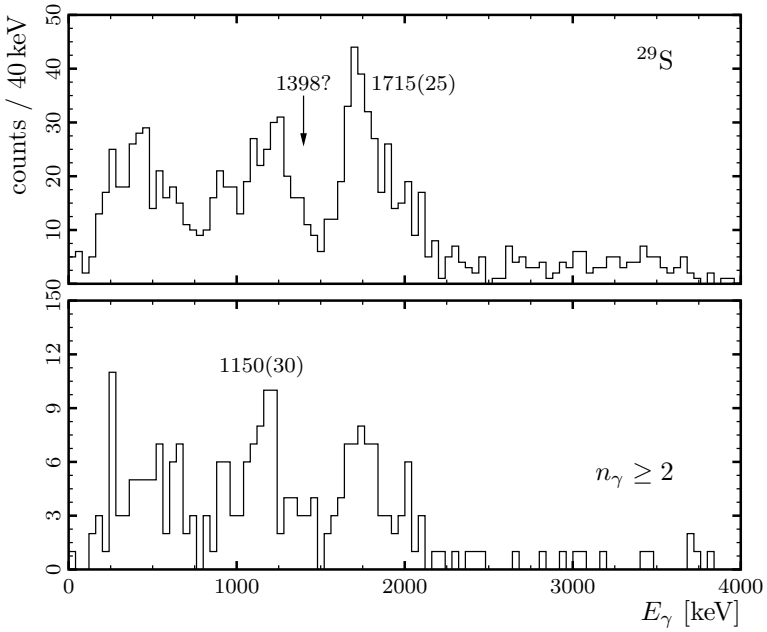

Figure A.5.: Gamma-ray spectra for the nucleus ^{29}S. The energy of the line indicated in the upper panel is 1715(25) keV. In the lower panel, a γ multiplicity of two or more is required. Here, a second line at 1150(30) keV can be identified.

number of counts, an accumulation of counts is visible below 2 MeV. The centroid of this distribution is at 857 keV. If this is the energy of the first excited state in ^{31}Ar, it is around 90 keV lower than in the mirror nucleus, ^{31}Al [MBB$^+$05].

A.4. Spectroscopy of ^{29}S

A γ-ray spectrum for ^{29}S is shown in figure A.5. The most prominent γ ray appears at an energy of 1715(25) keV. The second spectrum, in the lower panel of figure A.5, shows the distribution of γ-ray energies for multiplicities of two or more. Here, also a line at 1150(30) keV can be identified. In the mirror nucleus, ^{29}Al, no line of a similar energy and high intensity is known.

In ^{29}Al, the first and second excited states have energies of 1398 and 1754.2(2) keV, respectively. If the line at 1.7 MeV observed in ^{29}S corresponds to the second excited state in ^{29}Al, also the first excited state should be visible. In figure A.5, an arrow indicates the energy of this state in ^{29}Al. In ^{29}S, there is no sign of such a transition, so the corresponding state must have quite a different energy.

The interpretation of these spectra is hampered by the low resolution of the BaF_2 detectors which does not allow a sufficient separation of the lines.

B. Software for the Analysis of Knockout Experiments

To facilitate the analysis of the Ca experiment, a 'database' software has been developed. Due to the relatively fast reading of the data and the interface to ROOT [BR97], it permits an interactive analysis of data. On the other hand, methods are also provided to access the data with a compiled program. A description of the software has been published in [Bür07].

B.1. Motivation

In a typical fragmentation/knockout experiment, many different particles are produced and identified. For the analysis of these data, a variety of spectra are needed for many nuclei. Especially at the beginning of the analysis, or even during the experiment, many attempts are made trying to understand if the experiment works as planned, or if the results are roughly as expected.

To obtain spectra for a specific nucleus, this nucleus has to be identified with the help of detectors. Such particle identification detectors are described both in chapter 3 and 4. A specific nucleus, or a specific reaction channel, is then identified by correlations between the signals for these detectors. For example, a reaction channel might be selected by requesting two time-of-flight values and two energy loss values to be in certain ranges.

The data acquisition system of a typical experiment records data for all nuclei, thus postponing the selection of the interesting nuclei out of all the produced ones. To obtain a histogram for one specific nucleus, it is only necessary to read the part of the data taken in events that belong to this isotope. All other data may be skipped, and skipping them also has the benefit of reducing the amount of time needed until the histogram is visible. In the GANIL experiment from chapter 3, about 60 000 ^{36}Ca nuclei were identified in a total of about 20 million events. From these numbers it is clear that the gain in speed may be enormous if only the ^{36}Ca event data are read to produce a histogram for this nucleus.

One technique to reduce the amount of data to be read is to *pre-sort* the data into smaller sets, each containing data on one specific nucleus. This approach has some disadvantages:

- The selection criteria for the nuclei are fixed—broadening them requires re-reading the whole dataset, even if the broadening is small.
- The association of datasets and nuclei is done manually, which is laborious if a large number of nuclei is produced, and it is an error-prone task.

- The data are typically stored in separate files, thus producing a large number of files that want to be handled, and may not be confused.

Storing all data in a single file and using the computer to select the desired data can eliminate these disadvantages. It can also offer a more convenient user interface: doing 'the same' to a different nucleus could be done with two mouse-clicks. The prospect of these advantages was enough motivation to develop the software presented here.

The concept of the software is similar to the *Blue* database by Cromaz *et al.* [CSL+01]. Their software is designed specifically for the analysis of high-spin data from present and future γ-ray detector arrays like Gammasphere [Lee90], Greta/Gretina [Lee03], EUROBALL [KL03], and AGATA [N+]. Therefore it is adapted to storing high-multiplicity γ-ray data with a high compression, and also to read back the data in a way suitable for the analysis of such experiments. The treatment of these data, as implemented in *Blue*, is more complex than the selection of events based on particle-identification data implemented here. The reason is that no order is inherent to a multiplet of detected γ rays, while the particle-identification signals always come from the same detectors.

B.2. Sorting Algorithm

The program sorts the data in a *kd* tree to allow fast access to a subset for specific nuclei. To do so, the variables used to index the tree have to be specified by the user. For the GANIL experiment, these variables were the signals from the particle identification detectors after the target. These span a multi-dimensional space which is divided alternatingly along the axes into smaller and smaller hypercubes. Let the variables be denoted by $q_k \in \mathbb{Q}_k$ with $1 \leq k \leq m$, and the hypercubes of dimension m numbered by b.

In the beginning, there is only one cube $V_{b=0}$ (dropping the *hyper* from now on), into which the data are stored until a given limit n_s of datasets in the cube is reached. Then, all the data in V_b are analyzed with respect to q_k where $k = (d \bmod m) + 1$ with the depth d of the cube in the tree. From the values of the q_k, n_l limits $l_{b,i}$ $(i = 1, 2, \ldots, n_l)$ are calculated for 'child' cubes. For example, for $n_l = 1$ the mean value of the q_k could be calculated and taken as $l_{b,1}$, or the range of q_k could be divided into equally large intervals for any m. The children of cube V_b are the cubes V_{b_i} with

$$V_{b_i} = V_b \cap \tilde{V}_{b_i}$$

where

$$\tilde{V}_{b_i} = \mathbb{Q}_1 \times \cdots \times ([l_{b,i-1}, l_{b,i}] \cap \mathbb{Q}_k) \cdots \times \mathbb{Q}_m.$$

Here, $i = 1, 2, \ldots, n_l + 1$, $l_{b,0} = -\infty$ and $l_{b,n_l+1} = +\infty$. After calculating the limits, the event data are distributed into the $n_l + 1$ child cubes V_{b_i}.

After the splitting, further data are sorted into the child cubes. As soon as a child cube contains n_s datasets, it is also split with the same technique as described, but as it has a different depth d, a different variable q_k will be used to calculate the limits for the splitting step.

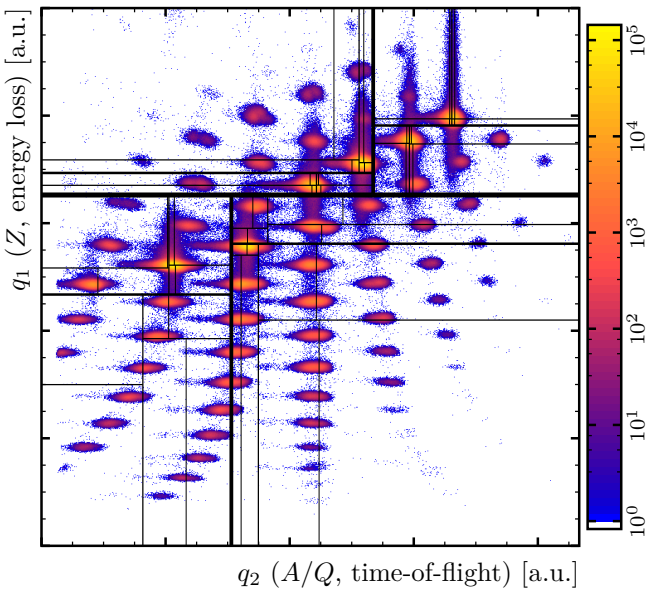

Figure B.1.: Particle identification matrix and its division in rectangles for $m = 2$, $n_l = 1$ and division at the mean q_k value. The x axis shows the time-of-flight after the target (q_2), and the y axis the signal from the ionization chamber (q_1), both in arbitrary units. To keep the figure simple, only the divisions for depths $d = 0, 1, \ldots, 5$ are shown. Thicker lines correspond to divisions at lower d. The experimental data that were sorted are shown in the background.

This procedure creates a tree structure of cubes, where the child cubes divide one of the axes of their parent cube in finer intervals. As all data in a cube are analyzed when the cube is split, they are better kept in the computer's RAM for a fast splitting. As this storage capacity is limited, the splitting is stopped when a given number of cubes has been created. Then, all data from the cubes are written to disk storage and only the limits $l_{b,i}$ are kept in memory. The remaining data are sorted into the cubes and immediately stored on disk. After all data have been read, the tree structure of limit values $l_{b,i}$ is also stored to disk with an index to the data.

This procedure is only useful for data that are not sorted with respect to any of the q_k. In most experiments, data are written on tape or disk in the so-called *list-mode*, i.e. the data are stored in the order the events are coming. Such data can easily be sorted with the algorithm described. It is also presently a requirement that the data are complete in the sense that all data relevant for one event are in the same dataset. This is not the case, for example, for data from a so-called *total data readout* (TDR) system as it is used in Jyväskylä. In the TDR system, data from different detectors are associated with a time-stamp and stored on disk independently. In the analysis, the data 'belonging together' are identified by the relation of their time-stamps, but this relation is not necessarily constant.

If the resulting structure of cubes is not fine enough, it can be refined using a second

Listing B.1: Code snippet for reading from a database, with a polygon selection on the variables q1 and q2

```
#include "dbgetter.h"
// open database file; assumed to include variables q1,q2 and x3,x4
DBGetter db( "example.db" );
// add polygon selection, defined as a string
db.AddCut( PolyCut::Create( &db, "q1 q2 5 0 0 0 1 1 1 1 0 0 0" ) );
// obtain accessors for the variables
Field* f_x3 = db.FindField("x3");
Field* f_x4 = db.FindField("x4");
// start looping
Limits limits;
for( db.GoToStart( limits ); db.GetNextEvent( limits ); ) {
   // analysis -- do something with x3 and x4
   /* ... */
}
```

program. This program works with the same algorithm, but it reads the contents of the hypercubes, again making use of the *not sorted* requirement.

An example for the division of a plane ($m = 2$) is shown graphically in figure B.1 for data from the GANIL experiment. It can be seen that the division is fine for high intensity components of the beam.

B.3. Reading from the Database

Retrieving data from the database starts by reading the limits of the cubes. Also the selection criteria for a nucleus max be regarded as the specification of a cube. In case this is not true immediately, a cube enclosing the volume corresponding to the identification criteria can be found. The tree structure of cubes is then visited. Data from cubes with an empty intersection between cube limits and selection criteria need not be read. Especially for exotic nuclei that are produced only in small amounts, the number of datasets to be read may be much smaller than the total count of datasets. This results in significantly decreased reading times for the data of such nuclei.

B.4. Implementation in C++

The software has been implemented in the C++ programming language [Str97]. The data of each event are organized in variables and arrays of fixed or variable size, each of which is given an almost arbitrary name. The data of each such variable may be of integer type with 8, 16 or 32 bit, or of floating point type. The choice of types may easily be extended. The database may be accessed using the interactive command input facility of the data analysis software ROOT [BR97], or using a compiled program as illustrated

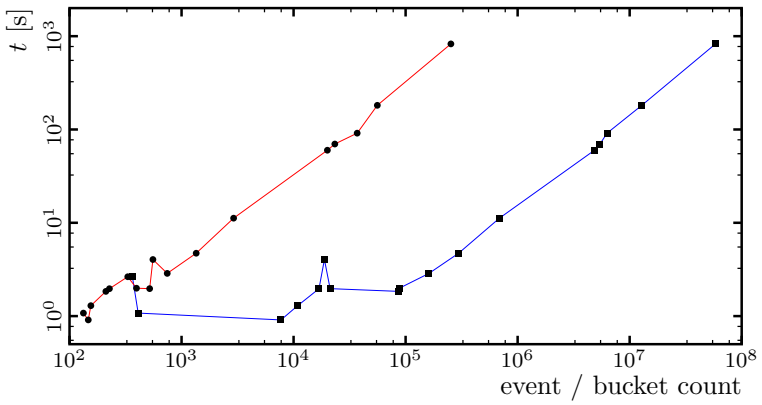

Figure B.2.: The time t needed to read all data for a specific nucleus is approximately proportional to the number of selected events (■) and cubes (●) with a lower limit set by the time needed to read the index.

in listing B.1. To save disk space, the data are compressed using the standard `zlib` library [GA].

B.5. Results

As mentioned, the software was used for most of the analysis of the data from the GANIL experiment on ^{36}Ca. Databases have been created with $m = 4$ using the ionization chamber signal as q_1, the time-of-flight signal after the target as q_2, the charge deposited in the drift chambers as q_3 and the energy deposited in the scintillator as q_4, thus alternating between mass and charge identification. In the run with ^{37}Ca secondary beam and the CATS detector as timing detector at the target position, about $6 \cdot 10^7$ events have been recorded. The database for these runs has been created in two steps in about 2.5 h. It has a size of about 5.5 GB and contains about 250000 hypercubes. Figure B.2 shows query times for this database as a function of the number of selected events and cubes. Two regions may be distinguished:

- for nuclei with small event numbers, the reading time is dominated by the time needed to read the limit tree structure and therefore approximately constant;
- the reading time for larger event numbers is approximately proportional to the number of selected events.

For the nucleus ^{36}Ca, the reading time is approximately 2 s for this database. Together with the databases for the runs with the MCP timing detector at the target position, both of similar size, the reading time for all ^{36}Ca events is only a few seconds. This has to be compared to reading the full database which takes about 20 min.

The reading times depend on the choice of q_k (e.g. the time of flight before the target could be included), and the amount of data stored for each event. The approximate proportionality of reading time and event count is not broken by such changes.

B.6. Summary

The software developed for the analysis of the GANIL experiment has proven to be a reliable tool for data analysis. It is also in use for another knockout experiment analyzed at the TU München. The time for producing spectra was drastically reduced for nuclei produced in small amounts compared to reading the full database and ignoring most of the data read in.

C. Scattering Angle Calculation

The calculation of the scattering angle in the RISING experiment will be explained in this Appendix, including the calculation of the error in this measurement.

In the setup used for this RISING experiment, the tracking of the beam particles is done using two multi-wire detectors and CATE as illustrated in fig. 4.4. Let the measured positions be denoted $\vec{m}$ for MW1, $\vec{n}$ for MW2 and $\vec{c}$ for CATE. The z components contain the detector positions along the beam line. The vector

$$\vec{a} = \vec{n} - \vec{m} \tag{C.1}$$

is the direction of the particle as measured by the multi-wire detectors, i.e. the direction of the incoming particle. The direction of the outgoing particle is

$$\vec{b} = \vec{c} - \vec{m} - f\vec{a} \quad \text{with} \quad f = (t_z - m_z)/a_z \tag{C.2a}$$

$$\Rightarrow b_z = c_z - t_z \tag{C.2b}$$

where t_z is the position of the target along the beam line. The vector $\vec{b}$ describes the direction from the target to CATE, calculated from the position measured with CATE ($\vec{c}$) and the extrapolation to the target from the multi-wire detectors. The scattering angle α (see fig. 4.4) can be calculated as

$$\cos\alpha = s = \frac{\vec{a}\cdot\vec{b}}{|a||b|}. \tag{C.3}$$

To calculate the error in α, the partial derivatives have to be calculated. For f, only the derivatives with respect to n_z and m_z are non-zero:

$$\frac{\partial f}{\partial n_z} = -\frac{f}{a_z} \quad \text{and} \quad \frac{\partial f}{\partial m_z} = \frac{f-1}{a_z}. \tag{C.4}$$

For the inverse length of a vector $\vec{v}$,

$$\frac{\partial}{\partial v_x}\frac{1}{|v|} = \frac{\partial}{\partial v_x}\frac{1}{\sqrt{v_x^2+v_y^2+v_z^2}} = -\frac{v_x}{|v|^3}. \tag{C.5}$$

Because n_z and m_z appear in f, they also appear in b_x and b_y, while b_z does not depend on n_z. The vector $\vec{c}$ appears only in $\vec{b}$, so the derivatives are

$$\frac{\partial s}{\partial c_x} = \frac{a_x}{|a||b|} - \frac{s b_x}{|b|^2}, \tag{C.6}$$

and accordingly for c_y and c_z. The derivatives with respect to n_i ($i = x, y$) are

$$\frac{\partial s}{\partial n_i} = \frac{b_i - f a_i}{|a||b|} + s\left(\frac{f b_i}{|b|^2} - \frac{a_i}{|a|^2}\right). \tag{C.7}$$

For n_z, additional terms appear from f, but (C.2b) may be used for simplification:

$$\frac{\partial s}{\partial n_z} = \frac{1}{|a||b|}\left(b_z + \frac{f}{a_z}\left(a_x^2 + a_y^2\right)\right) + s\left(\frac{f}{a_z|b|^2}\left(a_x b_x + a_y b_y\right) - \frac{a_z}{|a|^2}\right). \tag{C.8}$$

The derivatives with respect to m_i ($i = x, y$) are

$$\frac{\partial s}{\partial m_i} = \frac{(f-1)a_i - b_i}{|a||b|} + s\left(\frac{a_i}{|a|^2} - \frac{(f-1)b_i}{|b|^2}\right). \tag{C.9}$$

For m_z the expression is

$$\frac{\partial s}{\partial m_z} = \frac{-1}{|a||b|}\left(b_z + \frac{f-1}{a_z}\left(a_x^2 + a_y^2\right)\right) - s\left(\frac{f-1}{a_z|b|^2}\left(a_x b_x + a_y b_y\right) - \frac{a_z}{|a|^2}\right). \tag{C.10}$$

Then, assuming independence of the errors of all nine measurements, the error in x can be calculated:

$$(\Delta s)^2 = \sum_{i=x,y,z}\left[\left(\frac{\partial s}{\partial c_i}\Delta m_i\right)^2 + \left(\frac{\partial s}{\partial m_i}\Delta m_i\right)^2 + \left(\frac{\partial s}{\partial n_i}\Delta m_i\right)^2\right]. \tag{C.11}$$

Finally, the error in the scattering angle is

$$(\Delta\alpha)^2 = \left(\frac{\Delta s}{1 - s^2}\right)^2. \tag{C.12}$$

The x and y measurements have precisions of 1 mm for the multi-wire detectors and 7 mm for CATE [WAB+05]. The multi-wire detectors being placed at 1930(5) and 1065(5) mm before the target, respectively, and CATE 1481(5) mm behind the target, an uncertainty of $\approx 0.35^\circ$ is obtained using the given formulas (for non-zero scattering angles), as quoted in section 4.4.3.

D. Efficiency Measurement with ^{60}Co

For the determination of the absolute efficiency of the RISING γ-ray detectors, a measurement with a ^{60}Co source was performed. In the following, the analysis of these data will be explained.

D.1. General Considerations

The analysis is based on the assumption that the radioactive source emits two γ rays in coincidence, with energies E_l and E_h. In the case of ^{60}Co, the energies are $E_l = 1173\,\mathrm{keV}$ and $E_h = 1332\,\mathrm{keV}$. For each crystal i the efficiency ϵ_i at E_h is to be determined. For this efficiency

$$\epsilon_i = \frac{M_i}{D} = \frac{N_i}{r_i D} \tag{D.1}$$

holds where M_i and N_i are the number of E_h and E_l singles in crystal i, where $r_i = N_i/M_i$ the ratio of the efficiency at E_l to the efficiency at E_h and D the number of decays outside the dead-time of the acquisition system. The number of coincidences c of both γ rays can then be written as

$$c = D \sum_i (\epsilon_i \sum_{j \neq i} r_j \epsilon_j). \tag{D.2}$$

Using eq. (D.1) this means

$$c = D \sum_i \frac{M_i}{D} \sum_{j \neq i} \frac{N_j}{D} = \frac{1}{D} \sum_i M_i (N_* - N_i) \quad \text{with} \quad N_* = \sum_j N_j. \tag{D.3}$$

So the number of decays outside the dead-time is

$$D = \frac{1}{c} \sum_i M_i (N_* - N_i). \tag{D.4}$$

From eq. (D.4) the efficiencies of each crystal can easily be determined by using eq. (D.1) again.

The statistical errors can be calculated from

$$\Delta D^2 = \frac{1}{c^2} \Big(D^2 \Delta c^2 + \sum_i [(N_* - N_i)^2 \Delta M_i^2 + M_i^2 (\Delta N_*^2 + (\Delta N_i^2)] \Big) \tag{D.5}$$

$$\Delta \epsilon_i^2 = \frac{1}{D^2} (\Delta M_i^2 + \epsilon_i^2 \Delta D^2) \tag{D.6}$$

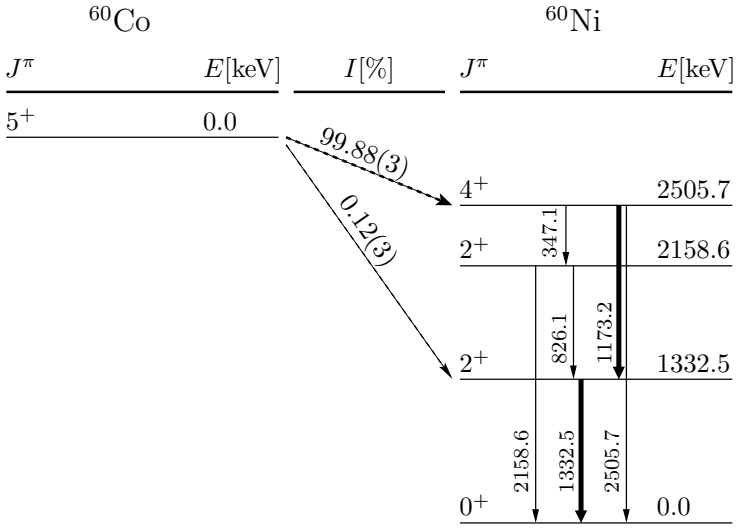

Figure D.1.: Decay of ^{60}Co [ENS07]. The dominant ($\geq$ 99.8 %) transitions are drawn with thicker lines. After most, but not all of the β^- decays of ^{60}Co, two γ rays of 1173 and 1332 keV are emitted in coincidence.

D.2. Advantages

There are two main reasons to use the present approach. One is that the calculated efficiency is independent of the dead-time of the data acquisition system, and also independent from information on the activity on the source. The other reason is the statistical error which is reduced as all quantities in eqs. (D.4) and (D.1) are large: c is for the full array of Ge detectors and also the number of singles events per crystal is large. Compared to a calculation like $\epsilon_i = \frac{c_i}{N_i}$ (with the number of coincidences of both γ-rays in one crystal c_i), the statistical error reduces by a factor in the order of $\sqrt{n}$ for n detectors.

D.3. Disadvantages

One difficulty comes from the branching ratio of the decay of ^{60}Co. Figure D.1 shows that 0.12 % of the decays go into the 1332 keV excited state so that there is only this gamma ray but no 1173 keV γ ray. A γ ray of 1173 keV is emitted in 99.85(3) % of the decays of the 4^+ state. These effects can be accounted for by scaling the measured coincidence rates.

A different problem is that the two γ rays from the ^{60}Co decay are correlated in their emission angle. The relation between the two angles is given by

$$W(\theta) = 1 + \frac{1}{8}\cos^2(\theta) + \frac{1}{24}\cos^4(\theta). \tag{D.7}$$

This relation is deduced in [SW92, p. 82-84]. Using the relative angle of the detectors

that observed both γ rays in coincidence, this angular distribution can be taken into account in the efficiency calculation.

The γ-ray spectra used for counting the M and N include some background. When counting the singles n_l and n_h, the background in the peak gate is also counted which is too much. This can be corrected by background subtractions.

Finally, for high activity sources, one or more additional decays may occur in the acquisition time window started by a first decay. Events where two γ rays of the same energy were detected are ignored in the analysis. The other cases cannot be distinguished from a single decay and therefore introduce a systematic error of the calculated efficiency.

The precise efficiency of the RISING γ-ray detectors is not needed for the calculation of $B(E2)$ values. As the $E(2^+)$ are different, the efficiency as a function of the γ-ray energy has to be known.

Bibliography

The references are sorted in alphabetical order of the reference keys.

[AAA+03] S. Agostinelli, J. Allison, K. Amako, J. Apostolakis, H. Araujo, P. Arce, M. Asai, D. Axen, S. Banerjee, G. Barrand, F. Behner, L. Bellagamba, J. Boudreau, L. Broglia, A. Brunengo, H. Burkhardt, S. Chauvie, J. Chuma, R. Chytracek, G. Cooperman, G. Cosmo, P. Degtyarenko, A. dell'Acqua, G. Depaola, D. Dietrich, R. Enami, A. Feliciello, C. Ferguson, H. Fesefeldt, G. Folger, F. Foppiano, A. Forti, S. Garelli, S. Giani, R. Giannitrapani, D. Gibin, J. J. Gómez Cadenas, I. González, G. Gracia Abril, G. Greeniaus, W. Greiner, V. Grichine, A. Grossheim, S. Guatelli, P. Gumplinger, R. Hamatsu, K. Hashimoto, H. Hasui, A. Heikkinen, A. Howard, V. Ivanchenko, A. Johnson, F. W. Jones, J. Kallenbach, N. Kanaya, M. Kawabata, Y. Kawabata, M. Kawaguti, S. Kelner, P. Kent, A. Kimura, T. Kodama, R. Kokoulin, M. Kossov, H. Kurashige, E. Lamanna, T. Lampén, V. Lara, V. Lefebure, F. Lei, M. Liendl, W. Lockman, F. Longo, S. Magni, M. Maire, E. Medernach, K. Minamimoto, P. Mora de Freitas, Y. Morita, K. Murakami, M. Nagamatu, R. Nartallo, P. Nieminen, T. Nishimura, K. Ohtsubo, M. Okamura, S. O'Neale, Y. Oohata, K. Paech, J. Perl, A. Pfeiffer, M. G. Pia, F. Ranjard, A. Rybin, S. Sadilov, E. di Salvo, G. Santin, T. Sasaki, N. Savvas, Y. Sawada, S. Scherer, S. Sei, V. Sirotenko, D. Smith, N. Starkov, H. Stoecker, J. Sulkimo, M. Takahata, S. Tanaka, E. Tcherniaev, E. Safai Tehrani, M. Tropeano, P. Truscott, H. Uno, L. Urban, P. Urban, M. Verderi, A. Walkden, W. Wander, H. Weber, J. P. Wellisch, T. Wenaus, D. C. Williams, D. Wright, T. Yamada, H. Yoshida, and D. Zschiesche (Geant4 Collaboration): «Geant4 – a simulation toolkit». Nucl. Instr. Meth. A **506**, 250–303 (2003). DOI: 10.1016/S0168-9002(03)01368-8. URL `http://geant4.web.cern.ch/geant4/`

[ASM+86] R. Anholt, C. Stoller, J. D. Molitoris, D. W. Spooner, E. Morenzoni, S. A. Andriamonje, W. E. Meyerhof, H. Bowman, J.-S. Xu, Z.-Z. Xu, J. O. Rasmussen, and D. H. H. Hoffmann: «Atomic collisions with relativistic heavy ions. VI. Radiative processes». Phys. Rev. A **33**, 2270–2280 (1986). DOI: 10.1103/PhysRevA.33.2270

[AWT03] G. Audi, A. Wapstra, and C. Thibault: «The AME2003 atomic mass evaluation». Nucl. Phys. A **729**, 337–676 (2003). DOI: 10.1016/j.nuclphysa.2003.11.003. URL `http://csnwww.in2p3.fr/AMDC/`

[BCG03] C. A. Bertulani, C. M. Campbell, and T. Glasmacher: «A computer program for nuclear scattering at intermediate and high energies». Comp. Phys. Comm. **152**, 317–340 (2003). DOI: 10.1016/S0010-4655(02)00824-X. arXiv: nucl-th/0207035

[BD04] C. A. Bertulani and P. Danielewicz: *Introduction to nuclear reactions*. Graduate Student Series in Physics (Institute of Physics Publishing, Bristol, 2004)

[Bec84] F. A. Beck: «Properties of Large BaF_2 Crystals. Application as Fast and Efficient Gamma-Ray Detectors In the $4\pi - \gamma$ Crystal Castle Array.» In *Nuclear Science Research Conference Series*, vol. 7, page 129 (Harwood, New York, 1984)

[BFG+89] L. Bianchi, B. Fernandez, J. Gastebois, A. Gillibert, W. Mittig, and J. Barrette: «SPEG: An energy loss spectrometer for GANIL». Nucl. Instr. Meth. A **276**, 509–520 (1989). DOI: 10.1016/0168-9002(89)90577-9

[BG77] P. Brussaard and P. Glaudemans: *shell-model applications in nuclear spectroscopy* (North-Holland, Amsterdam, 1977)

[BG06] C. A. Bertulani and A. Gade: «MOMDIS: a Glauber model computer code for knockout reactions». Comp. Phys. Comm. **175**, 372–380 (2006). DOI: 10.1016/j.cpc.2006.04.006. arXiv: nucl-th/0602048

[BGF+05] A. Banu, J. Gerl, C. Fahlander, M. Górska, H. Grawe, T. R. Saito, H.-J. Wollersheim, E. Caurier, T. Engeland, A. Gniady, M. Hjorth-Jensen, F. Nowacki, T. Beck, F. Becker, P. Bednarczyk, M. A. Bentley, A. Bürger, F. Cristancho, G. D. Angelis, Z. Dombrádi, P. Doornenbal, H. Geissel, J. Grebosz, G. Hammond, M. Hellström, J. Jolie, I. Kojouharov, N. Kurz, R. Lozeva, S. Mandal, N. Mărginean, S. Muralithar, J. Nyberg, J. Pochodzalla, W. Prokopowicz, P. Reiter, D. Rudolph, C. Rusu, N. Saito, H. Schaffner, D. Sohler, H. Weick, C. Wheldon, and M. Winkler: «^{108}Sn studied with intermediate-energy Coulomb excitation». Phys. Rev. C **72**, 061 305 (2005). DOI: 10.1103/PhysRevC.72.061305

[BGO95] E. Baron, J. Gillet, and M. Ozille: «The high power target system for SISSI, an intense source of secondary ions». Nucl. Instr. Meth. A **362**, 90–93 (1995). DOI: 10.1016/0168-9002(95)00308-8

[BGS+07] B. Bastin, S. Grévy, D. Sohler, O. Sorlin, Z. Dombrádi, N. L. Achouri, J. C. Angélique, F. Azaiez, D. Baiborodin, R. Borcea, C. Bourgeois, A. Buta, A. Bürger, R. Chapman, J. C. Dalouzy, Z. Dlouhy, A. Drouard, Z. Elekes, S. Franchoo, S. Iacob, B. Laurent, M. Lazar, X. Liang, E. Liénard, J. Mrazek, L. Nalpas, F. Negoita, N. A. Orr, Y. Penionzhkevich, Z. Podolyák, F. Pougheon, P. Roussel-Chomaz, M. G. Saint-Laurent, M. Stanoiu, I. Stefan, F. Nowacki, and A. Poves: «Collapse of the $N =$

28 shell closure in ^{42}Si». Phys. Rev. Lett. **99**, 022 503 (2007). DOI: 10.1103/PhysRevLett.99.022503

[BH04] C. A. Bertulani and P. G. Hansen: «Momentum distributions in stripping reactions of radioactive projectiles at intermediate energies». Phys. Rev. C **70**, 034 609 (2004). DOI: 10.1103/PhysRevC.70.034609. arXiv: nucl-th/0407026

[BHST02] B. Brown, P. Hansen, B. Sherrill, and J. Tostevin: «Absolute spectroscopic factors from nuclear knockout reactions». Phys. Rev. C **65**, 061 601(R) (2002). DOI: 10.1103/PhysRevC.65.061601

[BK66] G. E. Brown and T. T. S. Kuo: «Structure of finite nuclei and the free nucleon-nucleon interaction—An Application to ^{18}O and ^{18}F». Nucl. Phys. **85**, 40–86 (1966). DOI: 10.1016/0029-5582(66)90131-3

[BK67] G. E. Brown and T. T. S. Kuo: «Structure of finite nuclei and the free nucleon-nucleon interaction—General discussion of the effective force». Nucl. Phys. A **92**, 481–494 (1967). DOI: 10.1016/0375-9474(67)90627-6

[BL06] M. A. Bentley and S. M. Lenzi: «Coulomb energy differences between high-spin states in isobaric multiplets». Progr. Nucl. Part. Phys. (2006). DOI: 10.1016/j.ppnp.2006.10.001. In press

[BR97] R. Brun and F. Rademakers: «ROOT – An object oriented data analysis framework». Nucl. Instr. Meth. A **389**, 81 (1997). DOI: 10.1016/S0168-9002(97)00048-X

[BR06] B. A. Brown and W. A. Richter: «New "USD" Hamiltonians for the *sd* shell». Phys. Rev. C **74**, 034 315 (2006). DOI: 10.1103/PhysRevC.74.034315

[Bür07] A. Bürger: «A database for fast access to Particle-Gated Event data». Nucl. Instr. Meth. A **571**, 739–742 (2007). DOI: 10.1016/j.nima.2006.10.303

[BW88] B. Brown and B. H. Wildenthal: «Status of the Nuclear Shell Model». Ann. Rev. Nucl. Part. Sci. **38**, 29–66 (1988). DOI: 10.1146/annurev.ns.38.120188.000333

[Cas00] R. F. Casten: *Nuclear Structure from a Simple Perspective* (Oxford University Press, 2000), 2nd edn.

[Cau04] E. Caurier: «Shell Model Code `antoine`» (1989-2004). IReS, Strasbourg, France

[CGK+07] E. Clément, A. Görgen, W. Korten, E. Bouchez, A. Chatillon, J.-P. Delaroche, M. Girod, H. Goutte, A. Hürstel, Y. L. Coz, A. Obertelli, S. Péru,

C. Theisen, J. N. Wilson, M. Zielińska, C. Andreoiu, F. Becker, P. A. Butler, J. M. Casandjian, W. N. Catford, T. Czosnyka, G. D. France, J. Gerl, R.-D. Herzberg, J. Iwanicki, D. G. Jenkins, G. D. Jones, P. J. Napiorkowski, G. Sletten, and C. N. Timis: «Shape coexistence in neutron-deficient krypton isotopes». Phys. Rev. C **75**, 054 313 (2007). DOI: 10.1103/PhysRevC.75.054313

[CHP+02] P. D. Cottle, Z. Hu, B. V. Pritychenko, J. A. Church, M. Fauerbach, T. Glasmacher, R. W. Ibbotson, K. W. Kemper, L. A. Riley, H. Scheit, and M. Steiner: «$0^+_{\mathrm{gs}} \rightarrow 2^+_1$ Excitations in the Mirror Nuclei ^{32}Ar and ^{32}Si». Phys. Rev. Lett. **88**, 172 502 (2002). DOI: 10.1103/PhysRevLett.88.172502

[CN99] E. Caurier and F. Nowacki: «Present status of shell model techniques». Acta Phys. Pol. B **30**, 705 (1999)

[CNP02] E. Caurier, F. Nowacki, and A. Poves: «Large-scale shell model calculations for exotic nuclei». Eur. Phys. J. A **15**, 145–150 (2002). DOI: 10.1140/epja/i2001-10243-7

[Col98] B. J. Cole: «Proton and two-proton drip lines in the *sd* shell». Phys. Rev. C **58**, 2831–2839 (1998). DOI: 10.1103/PhysRevC.58.2831

[CSL+01] M. Cromaz, T. J. M. Symons, G. J. Lane, I. Y. Lee, and R. W. MacLeod: «Blue: a database for high-fold γ-ray coincidence data». Nucl. Instr. Meth. A **462**, 519–529 (2001). DOI: 10.1016/S0168-9002(00)01126-8

[DF74] A. E. L. Dieperink and j. T. de Forest: «Center-of-mass effects in single-nucleon knock-out reactions». Phys. Rev. C **10**, 543–549 (1974). DOI: 10.1103/PhysRevC.10.543

[DGR+07] P. Doornenbal, H. Grawe, P. Reiter, A. Al-Khatib, A. Banu, T. Beck, F. Becker, P. Bednarczyk, G. Benzoni, A. Bracco, A. Bürger, L. Caceres, F. Camera, H. Geissel, J. Gerl, M. Górska, J. Grębosz, H. Hübel, M. Kavatsyuk, O. Kavatsyuk, M. Kmiecik, I. Kojouharov, N. Kurz, R. Lozeva, A. Maj, S. Mandal, W. Meczynski, B. Million, Z. Podolyák, A. Richard, N. Saito, T. Saito, H. Schaffner, M. Seidlitz, T. Striepling, J. Walker, N. Warr, H. Weick, O. Wieland, M. Winkler, and H. Wollersheim: «The $T = 2$ mirrors ^{36}Ca and ^{36}S: A test for isospin symmetry of shell gaps at the driplines». Phys. Lett. B **647**, 237 (2007). DOI: 10.1016/j.physletb.2007.02.001

[DHB89] A. Dewald, S. Harissopulos, and P. von Brentano: «The Differential Plunger and the Differential Decay Curve Method for the Analysis of Recoil Distance Doppler-Shift Data». Z. Phys. A **334**, 163–175 (1989). DOI: 10.1007/BF01294217

[DJG+05] D.-C. Dinca, R. V. Janssens, A. Gade, D. Bazin, R. Broda, B. A. Brown, C. M. Campbell, M. P. Carpenter, P. Chowdhury, J. M. Cook, A. N. Deacon, B. Fornal, S. J. Freeman, T. Glasmacher, M. Honma, F. G. Kondev, J.-L. Lecouey, S. N. Liddick, P. F. Mantica, W. F. Mueller, H. Olliver, T. Otsuka, J. R. Terry, B. A. Tomlin, and K. Yoneda: «Reduced transition probabilities to the first 2^+ state in ^{52,54,56}Ti and development of shell closures at $N = 32, 34$». Phys. Rev. C **71**, 041 302 (2005). DOI: 10.1103/PhysRevC.71.041302

[EBB+02] J. Enders, A. Bauer, D. Bazin, A. Bonaccorso, B. A. Brown, T. Glasmacher, P. G. Hansen, V. Maddalena, K. L. Miller, A. Navin, B. M. Sherrill, and J. A. Tostevin: «Single-neutron knockout from ^{34,35}Si and ^{37}S». Phys. Rev. C **65**, 034 318 (2002). DOI: 10.1103/PhysRevC.65.034318

[EBB+03] J. Enders, T. Baumann, B. A. Brown, N. H. Frank, P. G. Hansen, P. R. Heckman, B. M. Sherrill, A. Stolz, M. Thoennessen, J. A. Tostevin, E. J. Tryggestad, S. Typel, and M. S. Wallace: «Spectroscopic factors measured in inclusive proton-knockout reactions on ^{8}B and ^{9}C at intermediate energies». Phys. Rev. C **67**, 064 301 (2003). DOI: 10.1103/PhysRevC.67.064301

[ENS07] «ENSDF Database» (2007). URL `http://www.nndc.bnl.gov/ensdf/`

[ETB+96] J. Eberth, H. G. Thomas, P. von Brentano, R. M. Lieder, H. M. Jäger, H. Kämmerling, M. Berst, D. Gutknecht, and R. Henck: «Encapsulated Ge detectors: development and first tests». Nucl. Instr. Meth. A **369**, 135–140 (1996). DOI: 10.1016/0168-9002(95)00794-6

[Far07] E. Farnea: (2007). URL `http://agata.pd.infn.it/`

[FZJ+04] B. Fornal, S. Zhu, R. V. Janssens, M. Honma, R. Broda, P. F. Mantica, B. A. Brown, M. P. Carpenter, P. J. Daly, S. J. Freeman, Z. W. Grabowski, N. J. Hammond, F. G. Kondev, W. Królas, T. Lauritsen, S. N. Liddick, C. J. Lister, E. F. Moore, T. Otsuka, T. Pawłat, D. Seweryniak, B. E. Tomlin, and J. Wrzesiński: «Development of shell closures at $N = 32, 34$. II. Lowest yrast excitations in even-even Ti isotopes from deep-inelastic heavy-ion collisions». Phys. Rev. C **70**, 064 304 (2004). DOI: 10.1103/PhysRevC.70.064304

[GA] J.-l. Gailly and M. Adler: «`zlib` (de)compression library». URL `http://www.zlib.org/`

[GAB+92] H. Geissel, P. Armbruster, K. H. Behr, A. Brünle, K. Burkard, M. Chen, H. Folger, B. Franczak, H. Keller, O. Klepper, B. Langenbeck, F. Nickel, E. Pfeng, M. Pfützner, E. Roeckl, K. Rykaczewski, I. Schall, D. Schardt, C. Scheidenberger, K.-H. Schmidt, A. Schröter, T. Schwab, K. Sümmerer, M. Weber, G. Münzenberg, T. Brohm, H.-G. Clerc, M. Fauerbach, J.-J.

Gaimard, A. Grewe, E. Hanelt, B. Knödler, M. Steiner, B. Voss, J. Weckenmann, C. Ziegler, A. Magel, H. Wollnik, J. P. Dufour, Y. Fujita, D. J. Vieira, and B. Sherrill: «The GSI projectile fragment separator (FRS): a versatile magnetic system for relativistic heavy ions». Nucl. Instr. Meth. B **70**, 286–297 (1992). DOI: 10.1016/0168-583X(92)95944-M

[Gad07] A. Gade: priv. comm. (2007)

[GAN07] GANIL website (2007). URL `http://www.ganil.fr/user/areas/index.html`

[GBB+04a] A. Gade, D. Bazin, B. A. Brown, C. M. Campbell, J. A. Church, D. C. Dinca, J. Enders, T. Glasmacher, P. G. Hansen, Z. Hu, K. W. Kemper, W. F. Mueller, H. Olliver, B. C. Perry, L. A. Riley, B. T. Roeder, B. M. Sherrill, J. R. Terry, J. A. Tostevin, and K. L. Yurkewicz: «One-neutron knockout reactions on proton-rich nuclei with N = 16». Phys. Rev. C **69**, 034 311 (2004). DOI: 10.1103/PhysRevC.69.034311

[GBB+04b] A. Gade, D. Bazin, B. A. Brown, C. M. Campbell, J. A. Church, D. C. Dinca, J. Enders, T. Glasmacher, P. G. Hansen, Z. Hu, K. W. Kemper, W. F. Mueller, H. Olliver, B. C. Perry, L. A. Riley, B. T. Roeder, B. M. Sherrill, J. R. Terry, J. A. Tostevin, and K. L. Yurkewicz: «Reduced Occupancy of the Deeply Bound $0d_{5/2}$ Neutron State in ^{32}Ar». Phys. Rev. Lett. **93**, 042 501 (2004). DOI: 10.1103/PhysRevLett.93.042501

[GBB+05] A. Gade, D. Bazin, C. A. Bertulani, B. A. Brown, C. M. Campbell, J. A. Church, D. C. Dinca, J. Enders, T. Glasmacher, P. G. Hansen, Z. Hu, K. W. Kemper, W. F. Mueller, H. Olliver, B. C. Perry, L. A. Riley, B. T. Roeder, B. M. Sherrill, J. R. Terry, J. A. Tostevin, and K. L. Yurkewicz: «Knockout from ^{46}Ar:$\ell = 3$ neutron removal and deviations from eikonal theory». Phys. Rev. C **71**, 051 301 (2005). DOI: 10.1103/PhysRevC.71.051301

[GH78] A. S. Goldhaber and H. H. Heckmann: «High energy interactions of nuclei». Ann. Rev. Nucl. Part. Sci. **28**, 161–205 (1978). DOI: 10.1146/annurev.ns.28.120178.001113

[GJB+06] A. Gade, R. Janssens, D. Bazin, B. Brown, C. Campbell, M. Carpenter, J. Cook, A. Deacon, D.-C. Dinca, S. Freeman, T. Glasmacher, M. Horoi, B. Kay, P. Mantica, W. F. Mueller, J. Terry, J. Tostevin, and S. Zhu: «One-neutron knockout in the vicinity of the $N = 32$ sub-shell closure: ^{9}Be(^{57}Cr,^{56}Cr+γ)X». Phys. Rev. C **74**, 047 302 (2006). DOI: 10.1103/PhysRevC.74.047302. arXiv: nucl-ex/0608053

[GKB+00] V. Guimarães, J. J. Kolata, D. Bazin, B. Blank, B. A. Brown, T. Glasmacher, P. G. Hansen, R. W. Ibbotson, D. Karnes, V. Maddalena, A. Navin,

B. Pritychenko, B. M. Sherrill, D. P. Balamuth, and J. E. Bush: «Spectroscopy of ^{13,14}B via the one-neutron knockout reaction». Phys. Rev. C **61**, 064 609 (2000). DOI: 10.1103/PhysRevC.61.064609

[Gla98] T. Glasmacher: «Coulomb exciation at intermediate energies». Ann. Rev. Nucl. Part. Sci. **48**, 1–31 (1998). DOI: 10.1146/annurev.nucl.48.1.1

[Gla01] T. Glasmacher: «Intermediate-energy Coulomb exciation». Nucl. Phys. A **693**, 90–104 (2001). DOI: 10.1016/S0375-9474(01)01147-2

[Goe49] M. Goeppert-Mayer: «On Closed Shells in Nuclei. II». Phys. Rev. **75**, 1969–1970 (1949). DOI: 10.1103/PhysRev.75.1969

[Gol74] A. Goldhaber: «Statistical Models of Fragmentation Processes». Phys. Lett. B **53B**, 306–308 (1974). DOI: 10.1016/0370-2693(74)90388-8

[Gra04] H. Grawe: «Shell Model from a Practitioner's Point of View». Lecture Notes in Physics **651**, 33–75 (2004). ISSN 1616-6361. DOI: 10.1007/b98790

[Gra07] M. Grasso: priv. comm. (2007)

[GS91] J.-J. Gaimard and K.-H. Schmidt: «A reexamination of the abrasion- ablation model for the description of the nuclear fragmentation reaction». Nucl. Phys. A **531**, 709–745 (1991). DOI: 10.1016/0375-9474(91)90748-U

[HBE96] K. Hencken, G. Bertsch, and H. Esbensen: «Breakup reactions of the halo nuclei ^{11}Be and ^{8}B». Phys. Rev. C **54**, 3043–3050 (1996). DOI: 10.1103/PhysRevC.54.3043

[HBJ+07] A. M. Hurst, P. A. Butler, D. G. Jenkins, P. Delahaye, F. Wenander, F. Ames, C. J. Barton, T. Behrens, A. Bürger, J. Cederkäll, E. Clément, T. Czosnyka, T. Davinson, G. de Angelis, J. Eberth, A. Ekström, S. Franchoo, G. Georgiev, A. Görgen, R.-D. Herzberg, M. Huyse, O. Ivanov, J. Iwanicki, G. D. Jones, P. Kent, U. Köster, T. Kröll, R. Krücken, A. C. Larsen, M. Nespolo, M. Pantea, E. S. Paul, M. Petri, H. Scheit, T. Sieber, S. Siem, J. F. Smith, A. Steer, I. Stefanescu, N. U. H. Syed, J. van de Walle, P. van Duppen, R. Wadsworth, N. Warr, D. Weisshaar, and M. Zielińska: «Measurement of the Sign of the Spectroscopic Quadrupole Moment for the 2_1^+ State in ^{70}Se: No Evidence for Oblate Shape». Phys. Rev. Lett. **98**, 072 501 (2007). DOI: 10.1103/PhysRevLett.98.072501

[Hey94] K. L. G. Heyde: *The Nuclear Shell Model* (Springer, Berlin, Heidelberg, 1994), 2nd corrected and enlarged edn.

[HGK+92] R. Holzmann, K. Grimm, R. Kulessa, E. Wajda, H. Xie, and M. Zinser: «Measurement of the Photon Background Produced by Atomic Processes in Relativistic Heavy-Ion Bombardments». GSI Annual Report page 48 (1992). (LAND collaboration)

[HJ62] T. Hamada and I. D. Johnston: «A potential model representation of two-nucleon data below 315 MeV». Nucl. Phys. **34**, 382–403 (1962). DOI: 10.1016/0029-5582(62)90228-6

[HJKO95] M. Hjorth-Jensen, T. T. S. Kuo, and E. Osnes: «Realistic Effective Interactions for Nuclear Systems». Phys. Rep. **261**, 125–270 (1995). DOI: 10.1016/0370-1573(95)00012-6

[HJS49] O. Haxel, J. H. Jensen, and H. E. Suess: «On the "Magic Numbers" in Nuclear Structure». Phys. Rev. **75**, 1766–1766 (1949). DOI: 10.1103/PhysRev.75.1766.2

[HKK+85] A. Huck, G. Klotz, A. Knipper, C. Miehé, C. Richard-Serre, G. Walter, A. Poves, H. L. Ravn, and G. Marguier: «Beta decay of the new isotopes ^{52}K, ^{52}Ca, and ^{52}Sc; a test of the shell model far from stability». Phys. Rev. C **31**, 2226–2237 (1985). DOI: 10.1103/PhysRevC.31.2226

[HOBM02] M. Honma, T. Otsuka, B. A. Brown, and T. Mizusaki: «Effective interaction for pf-shell nuclei». Phys. Rev. C **65**, 061 301 (2002). DOI: 10.1103/PhysRevC.65.061301

[HOBM04] M. Honma, T. Otsuka, B. A. Brown, and T. Mizusaki: «New effective interaction for pf-shell nuclei and its implications for the stability of the $N = Z = 28$ closed core». Phys. Rev. C **69**, 034 335 (2004). DOI: 10.1103/PhysRevC.69.034335

[HT03] P. G. Hansen and J. A. Tostevin: «Direct Reactions with Exotic Nuclei». Ann. Rev. Nucl. Part. Sci. **53**, 219–261 (2003). DOI: 10.1146/annurev.nucl.53.041002.110406

[IGM+97] N. Iwasa, H. Geissel, G. Münzenberg, C. Scheidenberger, T. Schwab, and H. Wollnik: «MOCADI, a universal Monte Carlo code for the transport of heavy ions through matter within ion-optical systems». Nucl. Instr. Meth. B **126**, 284–289 (1997). DOI: 10.1016/S0168-583X(97)01097-5

[JFM+02] R. V. F. Janssens, B. Fornal, P. F. Mantica, B. A. Brown, R. Broda, P. Bhattacharyya, M. P. Carpenter, M. Cinausero, P. J. Daly, A. D. Davies, T. Glasmacher, Z. W. Grabowski, D. E. Groh, M. Honma, F. G. Kondev, W. Królas, T. Lauritsen, S. N. Liddick, S. Lunardi, N. Marginean, T. Mizusaki, D. J. Morrissey, A. C. Morton, W. F. Mueller, T. Otsuka, T. Pawlat, D. Seweryniak, H. Schatz, A. Stolz, S. L. Tabor, C. A. Ur, G. Viesti, I. Wiedenhöver, and J. Wrzesiński: «Structure of ^{52,54}Ti and shell closures in neutron-rich nuclei above ^{48}Ca». Phys. Lett. B **546**, 55–62 (2002). DOI: 10.1016/S0370-2693(02)02682-5

[KB68] T. T. S. Kuo and G. E. Brown: «Reaction matrix elements for the $0f - 1p$ shell nuclei». Nucl. Phys. A **114**, 241–279 (1968). DOI: 10.1016/0375-9474(68)90353-9

[KGM+02] S. Kanno, T. Gomi, T. Motobayashi, K. Yoneda, N. Aoi, Y. Ando, H. Baba, K. Demichi, Z. Fülöp, U. Futakami, H. Hasegawa, Y. Higurashi, K. Ieki, N. Imai, N. Iwasa, H. Iwasaki, T. Kubo, S. Kubono, M. Kunibu, Y. Matsuyama, S. Michimasa, T. Minemura, H. Murakami, T. Nakamura, A. Saito, H. Sakurai, M. Serata, S. Shimoura, T. Sugimoto, E. Takeshita, S. Takeuchi, K. Ue, K. Yamada, Y. Yanagisawa, A. Yoshida, and M. Ishihara: «Coulomb Excitation of ^{24}Si». RIKEN Acc. Progr. Rep. **2001**, 70 (2002)

[Kha07] E. Khan: priv. comm. (2007)

[KL03] W. Korten and S. Lunardi: «Achievements with the EUROBALL spectrometer» (2003). URL `http://www-dapnia.cea.fr/Sphn/Deformes/EB/eb-report-final.pdf`

[KLS69] S. Kahana, H. C. Lee, and C. K. Scott: «Effect of Woods-Saxon Wave Functions on the Calculation of $A = 18, 206, 210$ Spectra with a Realistic Interaction». Phys. Rev. **180**, 956–966 (1969). DOI: 10.1103/PhysRev.180.956

[KM59] H. W. Koch and J. W. Motz: «Bremsstrahlung Cross-Section Formulas and Related Data». Rev. Mod. Phys. **31**, 920–956 (1959). DOI: 10.1103/RevModPhys.31.920

[Kuo67] T. T. S. Kuo: «State dependence of shell-model reaction matrix elements». Nucl. Phys. A **103**, 71–96 (1967). DOI: 10.1016/0375-9474(67)90790-7

[Lee90] I.-Y. Lee: «The GAMMASPHERE». Nucl. Phys. A **520**, c641–c655 (1990). DOI: 10.1016/0375-9474(90)91181-P

[Lee03] I.-Y. Lee: «GRETA - Gamma Ray Energy Tracking Array». In P. Fallon and R. Clark (Eds.), *Frontiers of Nuclear Structure*, vol. 656 of *American Institute of Physics Conference Series*, pages 343–348 (2003). DOI: 10.1063/1.1556663

[Leo94] W. R. Leo: *Techniques for Nuclear and Particle Physics Experiments* (Springer, Berlin/New York, 1994), 2nd edn.

[Lib01] J. Libin: «Construction of two multichannel drift chambers for the focal plane of SPEG». Nouvelles du GANIL **67** (2001)

[LMG+05] R. Lozeva, S. Mandal, J. Gerl, M. Gorska, J. Grebosz, I. Kojouharov, J. Adamczewski, A. Banu, F. Becker, T. Beck, P. Bednarczyk, A. Blazhev, P. Doornenbal, H. Geissel, M. Hellstroem, M. Kavatsyuk, O. Kavatsyuk, N. Kurz, M. Mutterer, S. Muralithar, G. Muenzenberg, W. Prokopowicz, N. Saito, T. Saitoh, H. Schaffner, K. Suemmerer, H. Weick, M. Winkler, C. Wheldon, and H.-J. Wollersheim: «Calorimeter Telescope for Identification of Relativistic Heavy Ion Reaction Channels». Acta Phys. Pol. B **36**, 1245–1248 (2005)

[LP95] K. Lau and J. Pyrlik: «Opimization of centroid-finding algorithms for cathode strip chambers». Nucl. Instr. Meth. A **366**, 298–309 (1995). DOI: doi:10.1016/0168-9002(95)00604-4

[MBB+05] F. Maréchal, D. L. Balabanski, D. Borremans, J.-M. Daugas, F. D. Santos, P. Dessagne, G. Georgiev, J. Giovinazzo, S. Grévy, P. Himpe, C. Jollet, I. Matea, G. Neyens, F. Perrot, E. Poirier, O. Roig, M. Stanoiu, C. Stodel, J.-C. Thomas, K. Turzó, D. Yordanov, E. Caurier, F. Nowacki, and A. Poves: «β decay of ^{31}Mg: Extending the "island of inversion"». Phys. Rev. C **72**, 044 314 (2005). DOI: 10.1103/PhysRevC.72.044314

[MLG+06] N. Mărginean, S. M. Lenzi, A. Gadea, E. Farnea, S. J. Freeman, D. R. Napoli, D. Bazzacco, S. Beghini, B. R. Behera, P. G. Bizzeti, A. Bizzeti-Sona, D. Bucurescu, R. Chapman, L. Corradi, A. N. Deacon, G. de Angelis, F. D. Vedova, E. Fioretto, M. Ionescu-Bujor, A. Iordachescu, T. Kröll, A. Latina, X. Liang, S. Lunardi, G. Montagnoli, R. Mărginean, M. Nespolo, G. Pollarolo, C. Rusu, F. Scarlassara, J. F. Smith, K. Spohr, A. M. Stefanini, S. Szilner, M. Trotta, C. A. Ur, B. J. Varley, and W. Zhimin: «Shape transitions far from stability: The nucleus ^{58}Cr». Phys. Lett. B **633**, 696–700 (2006). DOI: 10.1016/j.physletb.2005.12.047

[MRRS88] G. Musiol, J. Ranft, R. Reif, and D. Seeliger: *Kern- und Elementarteilchenphysik* (VEB Deutscher Verlag der Wissenschaften, Berlin, 1988)

[N+] J. Nyberg *et al.*: AGATA web site (Uppsala University). URL `http://www.agata.org/`

[NAA+00] A. Navin, D. W. Anthony, T. Aumann, T. Baumann, D. Bazin, Y. Blumenfeld, B. A. Brown, T. Glasmacher, P. G. Hansen, R. W. Ibbotson, P. A. Lofy, V. Maddalena, K. Miller, T. Nakamura, B. V. Pritychenko, B. M. Sherrill, E. Spears, M. Steiner, J. A. Tostevin, J. Yurkon, and A. Wagner: «Direct Evidence for the Breakdown of the $N = 8$ Shell Closure in ^{12}Be». Phys. Rev. Lett. **85**, 266–269 (2000). DOI: 10.1103/PhysRevLett.85.266

[Neu01] A. Neußer: *Ein Experiment zur Konversionselektronen-γ-Koinzidenzspektroskopie im ^{136}Nd am EUROBALL*. Diplomarbeit, Universität Bonn, Bonn (2001)

[OFU+01] T. Otsuka, R. Fujimoto, Y. Utsuno, B. A. Brown, M. Honma, and T. Mizusaki: «Magic Numbers in Exotic Nuclei and Spin-Isospin Properties of the NN Interaction». Phys. Rev. Lett. **87**, 082 502 (2001). DOI: 10.1103/PhysRevLett.87.082502

[OMA+99] S. Ottini-Hustache, C. Mazur, F. Auger, A. Musumarra, N. Alamanos, B. Cahan, A. Gillibert, A. Lagoyannis, O. Maillard, E. Pollacco, J. L. Sida, and M. Riallot: «CATS, a low pressure multiwire proportionnal chamber

for secondary beam tracking at GANIL». Nucl. Instr. Meth. A **431**, 476–484 (1999)

[OMLS+96] O. H. Odland, W. Mittig, A. Lépine-Szily, G. Fremont, M. Chartier, M. MacCormick, and J. M. Casandjian: «A fast position sensitive microchannel plate detector for ray-tracing of charged particles». Nucl. Instr. Meth. A **378**, 149–154 (1996). DOI: 10.1016/0168-9002(96)00441-X

[OSF+05] T. Otsuka, T. Suzuki, R. Fujimoto, D. Abe, H. Grawe, and Y. Akaishi: «Evolution of Shell and Collective Structures in Exotic Nuclei». Acta Phys. Pol. B **36**, 1213–1220 (2005)

[OUF+02] T. Otsuka, Y. Utsuno, R. Fujimoto, B. A. Brown, M. Honma, and T. Mizusaki: «Frontiers and challenges of the nuclear shell model». Eur. Phys. J. A **13**, 69–74 (2002)

[PMB+01] J. I. Prisciandaro, P. F. Mantica, B. A. Brown, D. W. Anthony, M. W. Cooper, A. Garcia, D. E. Groh, A. Komives, W. Kumarasiri, P. A. Lofy, A. M. Oros-Peusquens, S. L. Tabor, and M. Wiedeking: «New evidence for a subshell gap at $N = 32$». Phys. Lett. B **510**, 17–23 (2001). DOI: 10.1016/S0370-2693(01)00565-2

[PNC05] A. Poves, F. Nowacki, and E. Caurier: «Isovector effective charge and the staggering of $2^+ \to 0^+$ transition probabilities in the titanium isotopes». Phys. Rev. C **72**, 047 302 (2005). DOI: 10.1103/PhysRevC.72.047302

[PSCN01] A. Poves, J. Sánchez-Solano, E. Caurier, and F. Nowacki: «Shell model study of the isobaric chains $A = 50$, $A = 51$ and $A = 52$». Nucl. Phys. A **694**, 157–198 (2001). DOI: 10.1016/S0375-9474(01)00967-8. arXiv: nucl-th/0012077

[PZ81] A. Poves and A. Zuker: «Theoretical spectroscopy and the fp shell». Phys. Rep. **70**, 235–314 (1981). DOI: 10.1016/0370-1573(81)90153-8

[RCNP97] J. Retamosa, E. Caurier, F. Nowacki, and A. Poves: «Shell model study of the neutron-rich nuclei around $N = 28$». Phys. Rev. C **55**, 1266–1274 (1997). DOI: 10.1103/PhysRevC.55.1266

[RE07] T. Rodriguez and J. Egido: «New beyond-mean-field theories: Examination of the potential shell closures at $N = 32$ or 34». Phys. Rev. Lett. **99**, 062 501 (2007). DOI: 10.1103/PhysRevLett.99.062501

[RIS] «RISING homepage». URL `http://www-linux.gsi.de/~wolle/EB_at_GSI/PHOTOS/array-last3.jpg`

[RN67] R. R. Roy and B. P. Nigam: *Nuclear Physics* (Wiley & Sons, New York, 1967)

[RNT01] S. Raman, C. W. Nestor Jr., and P. Tikkanen: «Transition Probability From The Ground To The First Excited 2^+ State Of Even-Even Nuclei». Atomic Data and Nuclear Data Tables **78**, 1–128 (2001). DOI: 10.1006/adnd.2001.0858

[SB02] K. Sümmerer and B. Blank: «EPAX Version 2: A modified empirical parametrization of fragmentation cross sections». Nucl. Phys. A **701**, 161c (2002). DOI: 10.1016/S0375-9474(01)01566-4

[SCO+00] E. Sauvan, F. Carstoiu, N. A. Orr, J. C. Angélique, W. N. Catford, N. M. Clarke, M. M. Cormick, N. Curtis, M. Freer, S. Grévy, C. L. Brun, M. Lewitowicz, E. Liégarda, F. M. Marquésa, P. Roussel-Chomaz, M. G. S. Laurent, M. Shawcross, and J. S. Winfield: «One-neutron removal reactions on neutron-rich *psd*-shell nuclei». Phys. Lett. B **491**, 1–7 (2000). DOI: 10.1016/S0370-2693(00)01003-0

[SRD+06] M. Seidlitz, P. Reiter, A. Dewald, O. Möller, P. von Brentano, B. Bruyneel, S. Christen, F. Finke, C. Fransen, M. Gorska, A. Holler, G. Ilie, P. Knoch, P. Kudejova, S. Mandal, B. Melon, D. Mücher, J.-M. Regis, B. Saha, T. Steinhardt, T. Striepling, A. Wiens, T. Willers, and K. O. Zell: «Lebensdauermessungen in den neutronenreichen Kernen ^{56}Cr, ^{52}Ti» (2006). DPG Meeting

[SS00] R. Schneider and A. Stolz: «Ionisation Chamber MUSIC80» (2000). URL `http://www-w2k.gsi.de/bacquias/music80_manual.pdf`

[Sta03] M. Stanoiu: *Spectroscopie γ en ligne de noyaux légers riches en neutrons produits par fragmentation de faisceau radioactif et Mesures de temps de vie des niveaux excités dans des noyaux proches de ^{68}Ni.* Ph.D. thesis, Université de Caen (2003)

[Ste91] H. Stelzer: «Multiwire chambers with a two-stage gas amplification». Nucl. Instr. Meth. A **310**, 103–106 (1991). DOI: 10.1016/0168-9002(91)91006-H

[Str97] B. Stroustrup: *The C++ Programming Language* (Addison-Wesley, Reading, Massachusetts, 1997), 3rd edition edn.

[SW92] G. Schatz and A. Weidinger: *Nukleare Festkörperphysik* (Teubner, Stuttgart, 1992)

[Tar04] O. Tarasov: «Analysis of momentum distributions of projectile fragmentation products». Nucl. Phys. A **734**, 536–540 (2004). DOI: 10.1016/j.nuclphysa.2004.01.099

[TB03] O. Tarasov and D. Bazin: «Development of the program `LISE`: application to fusion-evaporation». Nucl. Instr. Meth. B **204**, 174–178 (2003). DOI: 10.1016/S0168-583X(02)01917-1

[TBB+02] J. Tostevin, D. Bazin, B. Brown, T. Glasmacher, P. G. Hansen, V. Maddalena, A. Navin, and B. Sherrill: «Single-neutron removal reactions from ^{15}C and ^{11}Be: Deviations from the eikonal approximation». Phys. Rev. C **66**, 024 607 (2002). DOI: 10.1103/PhysRevC.66.024607

[TBB+04] J. R. Terry, D. Bazin, B. A. Brown, J. Enders, T. Glasmacher, P. G. Hansen, B. M. Sherrill, and J. A. Tostevin: «Absolute spectroscopic factors from neutron knockout on the halo nucleus ^{1}5C». Phys. Rev. C **69**, 054 306 (2004). DOI: 10.1103/PhysRevC.69.054306

[Tos01] J. A. Tostevin: «Single-nucleon knockout reactions at fragmentation beam energies». Nucl. Phys. A **682**, 320c–331c (2001). DOI: 10.1016/S0375-9474(00)00656-4

[WA79] A. Winther and K. Alder: «Relativistic coulomb excitation». Nucl. Phys. A **319**, 518 (1979). DOI: 10.1016/0375-9474(79)90528-1

[WAB+05] H. J. Wollersheim, D. E. Appelbe, A. Banu, R. Bassini, T. Beck, F. Becker, P. Bednarczyk, K.-H. Behr, M. A. Bentley, G. Benzoni, C. Boiano, U. Bonnes, A. Bracco, S. Brambilla, A. Brunle, A. Burger, K. Burkard, P. A. Butler, F. Camera, D. Curien, J. Devin, P. Doornenbal, C. Fahlander, K. Fayz, H. Geissel, J. Gerl, M. Gorska, H. Grawe, J. Grebosz, R. Griffiths, G. Hammond, M. Hellstrom, J. Hoffmann, H. Hubel, J. Jolie, J. V. Kalben, M. Kmiecik, I. Kojouharov, R. Kulessa, N. Kurz, I. Lazarus, J. Li, J. Leske, R. Lozeva, A. Maj, S. Mandal, W. Meczynski, B. Million, G. Munzenberg, S. Muralithar, M. Mutterer, P. J. Nolan, G. Neyens, J. Nyberg, W. Prokopowicz, V. F. E. Pucknell, P. Reiter, D. Rudolph, N. Saito, T. R. Saito, D. Seddon, H. Schaffner, J. Simpson, K.-H. Speidel, J. Styczen, K. Summerer, N. Warr, H. Weick, C. Wheldon, O. Wieland, M. Winkler, and M. Zieblinski: «Rare ISotopes INvestigation at GSI (RISING) using gamma-ray spectroscopy at relativistic energies». Nucl. Instr. Meth. A **537**, 637–657 (2005). DOI: 10.1016/j.nima.2004.08.072

[Wei07] H. Weick: «ATomic Interaction with MAtter» (2007). URL `http://www-linux.gsi.de/~weick/atima/`

[Wil84] B. Wildenthal: «Empirical Strengths of Spin Operators in Nuclei». Progr. Nucl. Part. Phys. **11**, 5 (1984). DOI: 10.1016/0146-6410(84)90011-5

[YOG+06] K. Yoneda, A. Obertelli, A. Gade, D. Bazin, B. A. Brown, C. M. Campbell, J. M. Cook, P. D. Cottle, A. D. Davies, D.-C. Dinca, T. Glasmacher, P. G. Hansen, T. Hoagland, K. W. Kemper, J.-L. Lecouey, W. F. Mueller, R. R. Reynolds, B. T. Roeder, J. R. Terry, J. A. Tostevin, and H. Zwahlen: «Two-neutron knockout from neutron-deficient ^{34}Ar, ^{30}S, and ^{26}Si». Phys. Rev. C **74**, 021 303 (2006). DOI: 10.1103/PhysRevC.74.021303. arXiv: nucl-ex/0607017

[ZDF+06] S. Zhu, A. N. Deacon, S. J. Freeman, R. V. F. Janssens, B. Fornal, M. Honma, F. R. Xu, R. Broda, I. R. Calderin, M. P. Carpenter, P. Chowdhury, F. G. Kondev, W. Królas, T. Lauritsen, S. N. Liddick, C. J. Lister, P. F. Mantica, T. Pawłat, D. Seweryniak, J. F. Smith, S. L. Tabor, B. E. Tomlin, B. J. Varley, and J. Wrzesiński: «Level structure of the neutron-rich ^{56,58,60}Cr isotopes: Single-particle and collective aspects». Phys. Rev. C **74**, 064 315 (2006). DOI: 10.1103/PhysRevC.74.064315